2016

Reduction Of Mutual Coupling In Antenna Technology Using Elliptically Shaped Metasurfaces

Gabriel Moreno
University of Mississippi

REDUCTION OF MUTUAL COUPLING IN ANTENNA TECHNOLOGY USING

ELLIPTICALLY SHAPED METASURFACES

A Thesis
presented in partial fulfillment of requirements
for the degree of Masters in Engineering
in the Department of Electrical Engineering
The University of Mississippi

by

Gabriel Moreno

August 2016

ABSTRACT

This thesis is devoted to the use of metasurfaces for the goals of the reduction of mutual coupling between closely spaced antennas and the increase of antenna bandwidth. This is done first using a graphene monolayer as a cloak to decrease mutual coupling and restore radiation patterns for closely spaced antennas at THz frequencies. The introduction of the graphene monolayer was also extensively studied in regards to the effect on the radiation properties of the antennas.

The use of metasurfaces also has other applications, in particular with the bandwidth of antennas, where an anisotropic metasurface can be used to drastically increase the bandwidth of wire monopole antennas over a ground plane. This was then moved to an elliptical structure, using a strip monopole antenna. The last structure explored was for a microstrip antenna, where the strip monopole antenna is now placed above a ground plane on a substrate.

DEDICATION

I would like to dedicate this work to my family, especially my parents and my sister Catherine. Their support made sure this work made it to completion with their understanding and support.

ACKNOWLEDGEMENTS

I would like to thank my advisor Professor Alexander B. Yakovlev for his help and advice during this work and my other research at the University of Mississippi. Without his time, suggestions, and support, this work would not have been possible. I would also like to thank the other committee members, Professor Richard Gordon and Professor Elliot Hutchcraft for their help with this work. Hossein Bernety was also very helpful for his discussion during the work done on this thesis. Lastly I would like to thank my family for their help during this time. Their encouragement was invaluable during my research and writing.

Gabriel Moreno

TABLE OF CONTENTS

x

CHAPTER 1

INTRODUCTION

There has been significant work done on the theory and applications of metasurfaces. One particular area of interest is the use of metasurfaces combined with existing antenna structures. The field of metamaterials and more specifically metasurfaces has been of great interest in the past decade as these materials and surfaces can provide very interesting behaviors that cannot be found in normal materials [1]. This thesis will focus on the use of metasurfaces to improve the performance of antennas both to the mutual coupling between antennas placed close together, and with regards to the bandwidth of these antennas.

1.1 Graphene Characterization

One such metamaterial is graphene, it is a 2D material, as in the ideal case it is a one atom thick layer. Graphene was first discovered in by Novoselov et. al. in [2]. To this end, graphene has been studied extensively due to its interesting electrical and mechanical properties [3–8]. The manufacturing of graphene has also been a significant area of interest towards using graphene for more applications, as it is a complicated process with difficulties in producing high quality graphene [9, 10]. There are many opportunities to find uses for graphene [11–15], and the exploration of graphene's usefulness is continuing to this day. One such exciting opportunity is using graphene with antennas. Graphene has recently been used to make antennas in the THz frequency range, one of which is a cylindrical waveguide which behaves like a dipole antenna [12]. Another potential use of graphene is a planar dipole antenna made of graphene patches on a substrate [11]. The resonance frequency of these antennas can be tuned through biasing of the chemical potential of graphene μ_c.

Graphene has been of particular interest for its use as a metasurface at Terahertz (THz) frequencies. Graphene can be modeled as a two-sided surface characterized by its surface conductivity $\sigma(\omega, \mu_c, \Gamma, T)$, where ω is the radian frequency, μ_c is the chemical potential, Γ is the phenomenological scattering rate, $-e$ is the charge of an electron, $\hbar$ is the reduced Planck constant, and T is temperature [3],

$$\sigma(\omega, \mu_c, \Gamma, T) = \frac{je^2(\omega - j2\Gamma)}{\pi\hbar^2}[\frac{1}{(w - j2\Gamma)^2} \int_0^\infty \varepsilon\left(\frac{\partial f_d(\varepsilon)}{\partial \varepsilon} - \frac{\partial f_d(-\varepsilon)}{\partial \varepsilon}\right)d\varepsilon -$$

$$\int_0^\infty \frac{f_d(-\varepsilon) - f_d(\varepsilon)}{(\omega - j2\Gamma)^2 - 4(\varepsilon/\hbar)^2}d\varepsilon]. \tag{1.1}$$

The Fermi-Dirac distribution, $f_d(\varepsilon)$, is shown in (1.2),

$$f_d(\varepsilon) = (e^{(\varepsilon - \mu_c)/k_B T} + 1)^{-1}. \tag{1.2}$$

The surface conductivity is tunable via different parameters of the graphene, in particular the μ_c and Γ. The phenomenological scattering rate Γ can also be represented in terms of τ, which is the momentum relaxation time.

The surface conductivity of graphene (1.1) can be broken up into multiple terms in the THz frequency range, the intraband and interband conductivity. In the low THz range, the intraband contribution dominates the contribution from the interband. However, any calculations done with graphene were done using both the interband and intraband contributions to the surface conductivity. A closed form expression for the intraband contribution to the complex surface conductivity of graphene has been derived from the Kubo formula [3]:

$$\sigma_{intra} = j\frac{e^2 k_B T}{\pi\hbar^2(\omega + j\tau^{-1})}\left[\frac{\mu_c}{k_B T} + 2ln(e^{\frac{\mu_c}{k_B T}} + 1)\right]. \tag{1.3}$$

The second equation, for the interband surface conductivity (1.4), can be appproximated in

the case of $k_B T \ll |\mu_c|$,

$$\sigma_{inter} \cong \frac{je^2}{4\pi\hbar} ln\left(\frac{2|\mu_c| - \omega\hbar}{2|\mu_c| + \omega\hbar}\right), \qquad (1.4)$$

where k_B is the Boltzmann constant. For most of the calculations and simulations that follow, it should be noted that the temperature $T = 300$ K and the momentum relaxation time $\tau = 1.5$ ps. This value of τ corresponds to a high quality graphene, with low losses. The use of lower quality graphene will be addressed in terms of antenna efficiency and the input impedance of the cloaked antennas discussed in more detail in Chapter 2.

1.2 Cloaking at GHz and THz Frequencies

Cloaking has many potential potential applications in the world of electrical engineering. The path to cloaking objects started with the work of several groups, using a variety of methods [16–27]. The performance of these cloaks has also been explored with the goal of characterizing it in terms of performance versus bandwidth [28], or increasing the performance in [29]. One of the early important methods involved using transformation optics, which takes advantage of the form invariant properties of Maxwell's equations when taking a coordinate transformation [17]. The idea of plasmonic cloaking has also been explored extensively [30], to the point of experimental verification as in [31, 32]. Another method of interest is called scattering cancellation, which focuses on using thin mantle cloaks to provide the cloaking behavior. This method was introduced and further explored through several papers [33–35]. At GHz frequencies, the mantle cloak can be realized by using different patterns of metal on top of a dielectric substrate as in [36].

For this paper, the transverse magnetic (TM) polarized plane wave was chosen to impinge on the objects. This polarization represents the primary contribution to the overall scattering of an infinitely long dielectric cylinder. The specific choice of metasurface allows for some tuning in the mantle cloak. Vertical strips provide an inductive surface impedance, while horizontal rings provide a capacitive surface impedance. These different surfaces are

used for the cloaking of different types of objects, with the vertical strips used for the cloaking of dielectric cylinders, while the horizontal rings are used for the cloaking of PEC cylinders. The structure of these metasurfaces can be seen in Figs. 1.1 and 1.2.
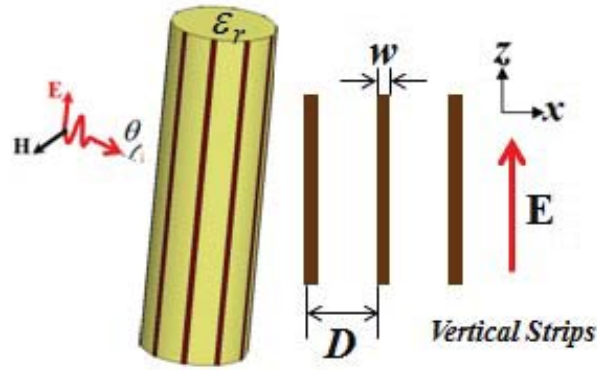
Figure 1.1. Vertical strips used as a metasurface to cloak a dielectric cylinder at GHz frequencies.
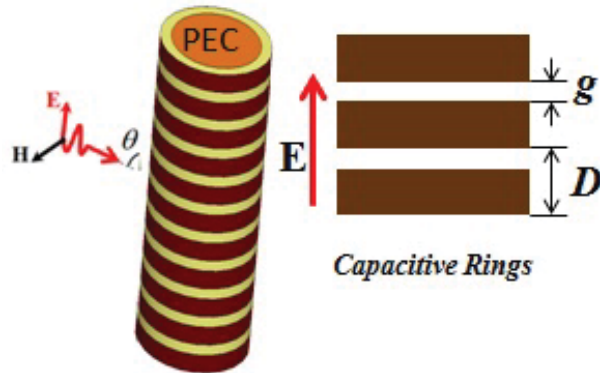
Figure 1.2. Horizontal rings used as a metasurface to cloak a PEC cylinder with a dielectric cylinder spacer at GHz frequencies.

There are also other surfaces available for cloaking, such as patches, Jerusalem crosses, and cross dipoles. All these surfaces have different geometrical parameters which can be changed to adjust the surface impedance of the entire structure. The concept of adjusting the parameters of the surface to change its properties will be important going forward, as this is a key component for the cloaking of antennas.

Graphene has been used previously to explore the possibility of cloaking objects at

THz frequencies, which started with work done by Chen and Alu in [18] and [19]. In [18], the authors explored the use of graphene to cloak planar and cylindrical objects. Graphene is a perfect candidate material for this type of cloaking in the low THz range, as it is a tunable material, and by the nature of the material, ideal Graphene is one atom thick. The goal of the mantle cloak is to provide "anti-phase" currents on the surface of the cloak, which drastically reduce the scattered fields from the object to be cloaked. When using graphene, it is important to consider the manufacturing process, which usually requires the graphene be grown on a substrate or directly on a metal [9]. Some additional work has been done on the transferring of graphene from said substrates to other materials [10].

Some additional studies were done into the effect of changing both the chemical potential μ_c and the momentum relaxation time, τ. Graphene's tunable nature is very useful in this regard, as by adjusting the chemical potential, the frequency at which an object is cloaked can be changed within a range of frequencies. τ is the momentum relaxation time, which is included in the intraband contribution to the surface conductivity, which is most frequently referred to with respect to the losses of graphene. A higher value of τ represents a higher quality graphene, with lower losses. A typical value for τ in this paper is $\tau =1.5$ ps.

For this cloaking structure, there is a range for μ_c where the object will be cloaked. This range of μ_c changes with frequency, as increasingly high μ_c are needed to cloak objects at higher frequencies in the low-THz. It is also important to note that not only can the frequency of the cloak be adjusted, but at a specific frequency, the scattering of the object can be carefully tuned. Since this tunability has nothing to do with the geometrical properties of the graphene monolayer cloak, this is a significant benefit over the earlier mentioned mantle cloaks at GHz frequencies.

In [19], the previous work on tunable graphene cloaking was expanded to the use of graphene nanopatches. In [37], it was established that graphene nanopatches have both an inductive and capacitive surface impedance in the low-THz, depending on the frequency. In general, the patches provide a capacitive surface impedance, as shown in [36] at GHz

frequency. However, the kinetic inductance of the graphene increases with frequency, which eventually overcomes the capacitance provided by the patches. The geometry of the patches can be adjusted to provide more or less capacitance. Additionally, the μ_c of the graphene can also be changed to alter the surface impedance of the patches.

Thanks to the increased tunability as a result of using graphene nanopatches, [19] provides several examples of cloaking using graphene monolayers and nanopatches. One of the more important facts is that the patches behave similarly to the graphene monolayer, only requiring adjustment of the μ_c to change the frequency at which the cloak operates. Multiple designs are detailed in the paper, and even with different μ_c, by changing the size of the patches, two different cloaks can operate at the same frequency.

1.3   Graphene Elliptical Cloaking

It is important to note that the previous work discussed was all done in a cylindrical coordinate system. The use of the cylindrical coordinate system is very useful for scattering cancellation, as the symmetry of it allows for an easier time when formulating the problem. However, there are some downsides, such as the need to use a wire dipole if you want to move into the cloaking of antennas. This desire to move away from wire dipoles led to work done by Bernety and Yakovlev to move into other coordinate systems, in this case, the elliptical coordinate system [38].

In their paper, Bernety and Yakovlev explore the cloaking of infinitely long elliptical cylinders at low-THz frequencies. The change in coordinate system leads to a complete reformulation of the scattering problem. The formulation is done with Mathieu functions of the angular and radial variety. In the elliptical coordinate system (u, v, z), the major and minor axes of the ellipse are represented by $u = tanh^{-1}(\frac{b}{a})$, where b is the minor axis and a is the major axis. Another important parameter for the use of the elliptical cloaking system is the focal point of the ellipse, which will be referred to as F. The first elliptical

cylinder is made of dielectric material, which in order to cloak requires a graphene monolayer. The second elliptical cylinder of interest is a perfect electric conducting cylinder, with an additional spacer, which is a larger dielectric cylinder placed around the PEC cylinder. The most interesting case for future purposes is the case of a strip embedded inside a dielectric elliptical cylinder. A strip in the elliptical coordinate system can be treated as a special case of an ellipse, where the minor axis of the ellipse is zero. The geometry of the strip and the graphene nanopatch cloak can be seen in Fig. 1.3.
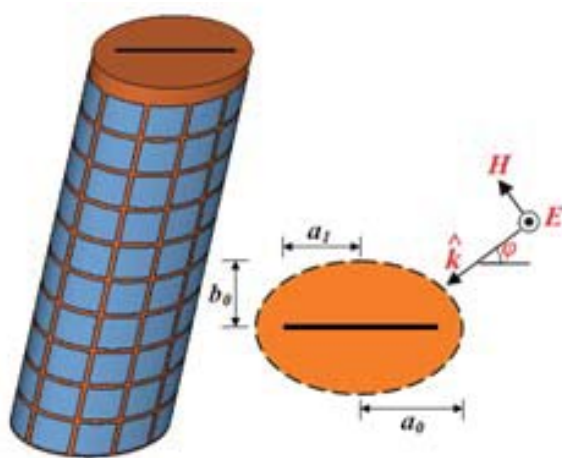
Figure 1.3. Graphene nanopatches used as a metasurface to cloak a metallic strip surrounded dielectric cylinder at THz frequencies.

For the three cases mentioned in [38], a cloak is created and the total scattering width is calculated and simulated. There is good agreement between the simulation and analytical solutions in these infinitely long structures. As mentioned before, graphene nanopatches can be used for the cloaking of dielectric of PEC elliptical cylinders. The graphene monolayers can only be used for elliptical dielectric cylinders due to its inductive surface impedance.

The third case is of the most interest for moving onto the cloaking of antennas, a strip placed inside a dielectric cylinder. In the infinite structure, the graphene nanopatches are used as the cloak. For all these cases, multiple angles of incidence are chosen, and it should be noted that the strip case is particularly sensitive to the angle of incidence, with the cloak being most effective for the case of 0 degrees, when the incident fields are directed

along the thinnest part of the ellipse.

It is important to note that all of these objects have been small compared to the size of the wavelength at the frequency the objects are being cloaked. This is a requirement of the scattering cancellation method, as there is a maximum sized object that can be cloaked. This maximum size was tested by using increasingly large configurations of objects to cloak. There are several configurations explored in [38], and many of these are interesting cases in their own right, but only two of these will be mentioned here. First, the change from one ellipse to two merged ellipses, each with their own cloak. The total length of these two ellipses is $L = \lambda/2.083$, which is a significant increase in the size of the object. The other key configuration is two separate strips covered with dielectric, placed very closely. This configuration is very similar to the future goal of the cloaking of antennas.

1.4 Reduction of Mutual Coupling between Strip Dipole Antennas in GHz

The cloaking mentioned in the previous sections has all focused on the theoretical case of cloaking infinitely large objects. This has some obvious benefits for the formulation of the problem, as analytical solutions can be calculated, and then verified through simulation. When the time comes for the transition to finite structures, there are some changes in the structure that cannot be accounted for in the analytical solutions. The idea of cloaking for antennas has always been a goal of the field, as in [39], where metasurfaces were used with the goal of reducing the mutual blockage between wire dipole antennas. The reduction of mutual coupling between antennas is something that has been explored extensively with multiple types of structures [40–51]. The paper by Bernety and Yakovlev [52] took the next step in cloaking in the GHz frequency range. The goal of this cloaking was to reduce the mutual coupling between two closely spaced antennas, and to restore the original radiation patterns. The cloaking structure follows from the previous section, using the elliptical coordinate system. The cloaks used in [52] are conformal and confocal. This means the cloaks are

wrapped around the dielectric elliptical cylinder, and the ellipse made by the cloak shares the same focal points as the dielectric. These focal points also coincide with the edge of the strip dipole antenna inside the dielectric. This is an important requirement for the elliptical cloaking structure. Two sets of antennas are cloaked in this paper, using two different metasurfaces.

The first metasurface used in this paper was metallic rings. These rings provide a capacitive surface impedance. The strip dipole antenna provides a similar case to the infinite strip surrounded by an elliptically shaped dielectric spacer mentioned in the previous section. When the rings are wrapped around the antenna resonating at $f_1 = 1$ GHz, cloaked the antenna at $f_2 = 5$ GHz. This cloaking behavior can be observed by studying the RCS of the isolated Antenna I. The addition of the rings causes a minimum in the RCS of Antenna I. As with previous cases, the RCS is studied as the result of a TM polarized plane wave. Antenna II in this case did not require a cloak due to the small size of the antenna in relation to the wavelength at the frequency f_1.

The second metasurface used in the paper was vertical strips, which provide an inductive surface impedance. The inductive surface impedance causes the cloaking effect to occur at a frequency much closer to the resonance frequency of the antenna. For this second case, the two antennas resonated at $f_1 = 3.02$ GHz, and $f_2 = 3.33$ GHz. These frequencies are much closer than the previous case, and as a result the radiation patterns of the uncloaked antennas are significantly perturbed. The cloaking provided by the vertical strips restores the radiation patterns of Antenna I and Antenna II at their resonance frequencies. Another important thing to note is that the mutual coupling between these antennas is also significantly reduced at the resonance frequencies.

1.5   Wideband Monopole Antenna

The bandwidth of antennas has always been a point of interest in the design of antennas. For this purpose, many different designs have been proposed to increase the bandwidth

of existing antenna designs [53–56]. In [57], a design for a wideband monopole antenna was introduced. This antenna used an anisotropic metasurface to drastically increase the impedance bandwidth of a quarter wavelength monopole over a ground plane using an SMA port. This antenna was simulated and then the antenna was created to experimentally verify the increased bandwidth. The metasurface used to create this broadband monopoly antenna is somewhat similar to the metasurfaces used in [36], it is a metallic dogbone pattern. This metasurface is very similar to the Jerusalem cross, but with only the vertical component. The increased bandwidth provided by this metasurface stems from a second resonance produced at a higher frequency. The monopole has a 2:1 VSWR bandwidth of 2.15-4.6 GHz, which is a significant increase over the same monopole without the metasurface. The structure of this metasurface is different from previous metasurfaces that have been discussed in that while it is in the cylindrical coordinate system, there is a significant air gap between both the antenna and the first layer, and the first layer with the second layer.

The original monopole antenna resonates at 2.5 GHz. The bandwidth of this original monopole is only 0.4 GHz. The introduction of the metasurface causes the original resonance of the antenna to shift down to 2.35 GHz, and a second resonance is produced at 3.85 GHz. The radiation properties of the antenna are not interfered with by the metasurface, as the radiation patterns are consistent throughout the frequency range. This will be expanded on in 3.

The antenna was created by manufacturing two planar metasurface sheets for the two layers. The layers were then curled to become the required circular inner and outer layers. The antenna was then tested, and found to agree very well with the simulated antenna. The radiation patterns of the simulated vs measured antennas were also in good agreement.

CHAPTER 2

CLOAKING OF ANTENNAS WITH A GRAPHENE MONOLAYER

2.1   Introduction

The cloaking of antennas is a significant area of interest in GHz and THz frequencies. Some initial work has been done, but there are still significant opportunities for continued research, for example, with respect to the cloaking of antennas. This chapter will focus specifically on the cloaking of strip dipole antennas in the low THz frequencies to reduce the mutual coupling between two closely spaced antennas. This work has many potential future applications for use with antennas in THz frequencies. This work is a continuation of work done by Bernety and Yakovlev in [52] which was done at GHz, and it is an expansion of [58] with a deeper study into the use of these antennas at different spacings, and with a further exploration into the varying of different parameters of the graphene. There are two important qualifications for our cloaked antennas that must be clarified before proceeding. When these two antennas are placed close together, the antennas should have reduced mutual coupling, and the patterns of the cloaked antennas should be restored as if the antenna was isolated. There are some key differences between the cloaking of antennas done at the GHz frequencies and this research, most of which spawn from using a graphene monolayer as the mantle cloak for the antennas. One of the key benefits of using the graphene monolayer is that it is a tunable material, thanks to the chemical potential μ_c. This allows the antennas to be changed without changing the geometrical properties of the antenna, so not only are the antennas cloaked, they can be reconfigured to resonate at different frequencies. This also

allows the antenna to be cloaked at different frequencies. The specifics of this tunability will be explained in the design process of how these cloaked strip dipole antennas are created.

2.2   Design Process for Cloaked Antennas

To accomplish the cloaking of two strip dipole antennas, a design process was conceived to create the antennas. A brief overview of this procedure will be given here. First, the cloaked Antenna I is created. This antenna is then simulated to obtain the S-parameters and the scattering behavior of the isolated Antenna I. With this information, we can obtain the frequency above the resonance frequency of the antenna at which the RCS and ACS are minimum, the frequency where the ACS and RCS are at a minimum is the frequency where the antenna is cloaked. This is done using a TM polarized plane wave, which constitutes the dominant scattering mode of the antenna. This frequency where the ACS and RCS are at a minimum is the desired resonance frequency of Antenna II. The resonance frequency and the frequency at which the antenna is cloaked can be shifted through the adjustment of the material properties of the graphene monolayer, in particular the chemical potential μ_c, or through changing the geometrical properties of the antenna, such as the length of the antenna or the size of the elliptical dielectric cylinder. For our purposes, the chemical potential μ_c will be kept in the range μ_c= 0.75 eV - 1.5 eV. By shifting the frequency at which the antenna is cloaked through changing the μ_c, a range of frequencies is obtained where Antenna II can operate and be cloaked by the initial design for Antenna I. It is important to verify that this minimum in the RCS and ACS that we used for Antenna I can also be obtained for Antenna II below it's resonance frequency. This will result in some adjustment in the μ_c to accommodate this goal. Once these two Antennas have the required RCS and ACS behavior, the antennas are placed together at a very close distance d $=\lambda/10.92$ where λ is the wavelength at the resonance frequency of the lower frequency antenna. Additional work has been done to further explore the behavior of these antennas at other distances,

such as $d = \lambda/32.8$, $d = \lambda/2$, $d = \lambda$.

The geometry of the cloaked and uncloaked antennas can be seen in Fig. 2.1. The uncloaked antenna in this case is a strip dipole antenna with an elliptically shaped dielectric surrounding this strip. The size of the dielectric has several impacts on the design of the cloaked antenna which will be explored in the following sections. As mentioned earlier, the size of the dielectric is chosen such that the focal points of the ellipse are at the edges of the strip inside the dielectric. As a result of this requirement, the dielectric becomes significantly thinner whenever the major axis length is smaller. This can be seen more clearly in Fig. 2.2, where Antenna I has dimensions $a = 1.75$ μm, and $b = 0.90$ μm, and Antenna II has dimensions $a = 2.0$ μm, and $b = 1.32$ μm.
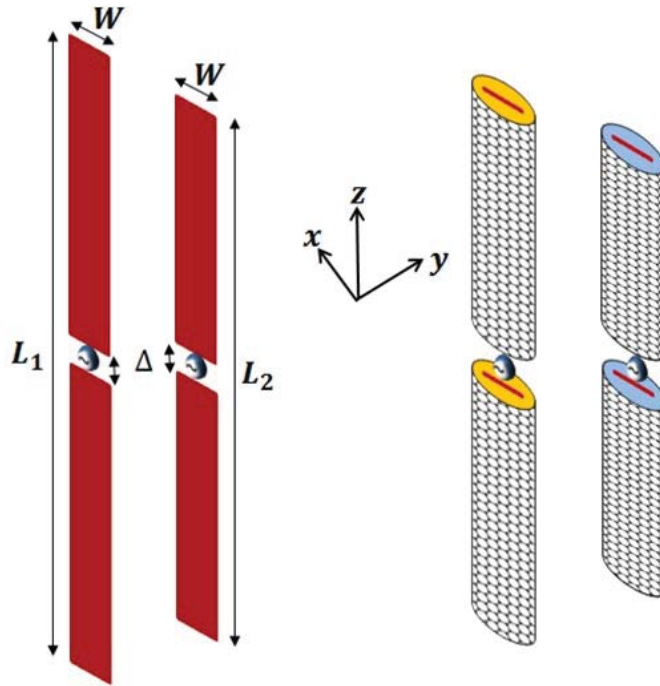
Figure 2.1. Geometry of the uncloaked and cloaked strip dipole antennas.

To start the design process, the effect that the graphene has on the strip dipole antenna in the low-THz frequency range must be noted. In Fig. 2.3, the S_{11} for the strip dipole antenna with the dielectric elliptical cylinder is shown in gray. The same antenna is now covered with an elliptically shaped graphene monolayer, and the change in the S_{11}

13

Figure 2.2. Cross section of the elliptical dielectric cylinders used for the cloaked antennas. The two elliptical cylinders shown here are representative of the final designs, where Antenna I has a smaller ellipse and Antenna II has the larger ellipse.

is shown in black. The first thing that is important to note that the introduction of the graphene monolayer causes a frequency shift in the resonance frequency of the antenna. This is due to the effect of the graphene monolayer in the input impedance of the antenna. The introduction of the graphene monolayer also creates a frequency at which the antenna becomes a very poor radiator, which is of interest for when the antennas are brought together. Not only should the antenna have a low RCS and ACS at the frequency which the other antenna resonates, the antenna should not radiate well at that frequency.
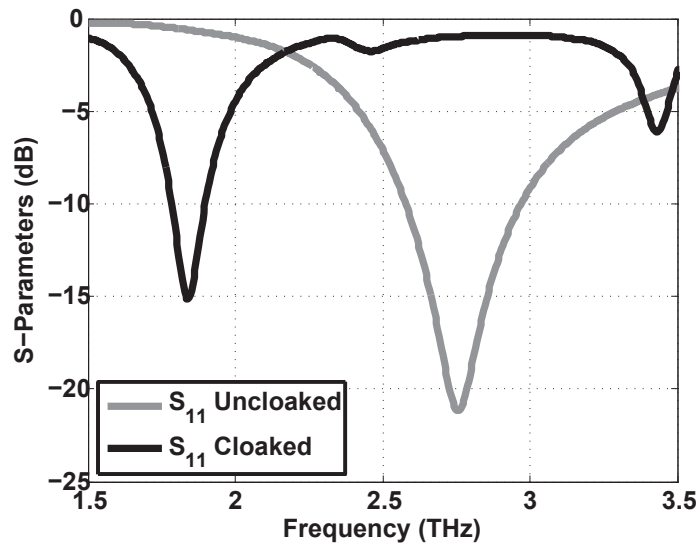
Figure 2.3. S_{11} for the isolated Antenna I, cloaked and uncloaked with $L_1 = 44$ μm.

14

2.2.1 Graphene Monolayer's Effect on Antenna Input Impedance

The graphene monolayer used in the cloaking of these antennas was introduced earlier in chapter 1. Some of the properties of the graphene monolayer are important to keep in mind when considering the impact of the graphene monolayer on the input impedance of the strip dipole antennas being used. In the low THz, the surface conductivity of a graphene monolayer can be calculated using the Kubo formula as shown from the combination of the intraband contribution (1.3) and the interband contribution (1.4). Using these two contributions to the surface conductivity, the surface impedance can be found by taking the inverse of the total surface conductivity,

$$Z_s = \frac{1}{\sigma_{intra} + \sigma_{inter}}. \tag{2.1}$$

A plot of Z_s vs. frequency can be seen in Fig. 2.4 for a graphene monolayer with $\mu_c = 1.5$ eV and $\tau = 1.5$ ps. This plot represents the surface impedance of the graphene monolayer for the maximum values of μ_c and τ that can and will be used for the cloaking of antennas. It is important to note the effect that the μ_c and τ have on this plot of the surface
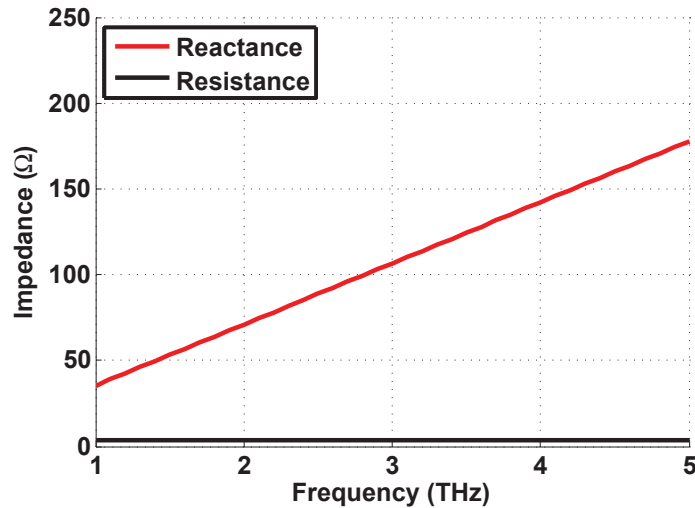
Figure 2.4. Surface resistance and reactance of a graphene monolayer with $\mu_c = 1.5$ eV and $\tau = 1.5$ ps.

impedance. A reduction in the μ_c of the graphene monolayer represents an increase of the imaginary surface reactance, which can be seen in Fig. 2.5. A reduction in τ represents an increase in the losses in the graphene, which results in an increase in the real part of the surface impedance over the entire frequency range. For example, in the low-THz frequency range, a graphene monolayer with $\mu_c = 1.5$ eV and $\tau = 1.5$ ps has a resistance of $\text{Real}(Z_s)$ = 3.77 Ω. A decrease in τ to 1.0 ps results in increase of the resistance to $\text{Real}(Z_s) = 5.66$ Ω. The same decrease in τ has no effect on the imaginary part of the surface impedance.
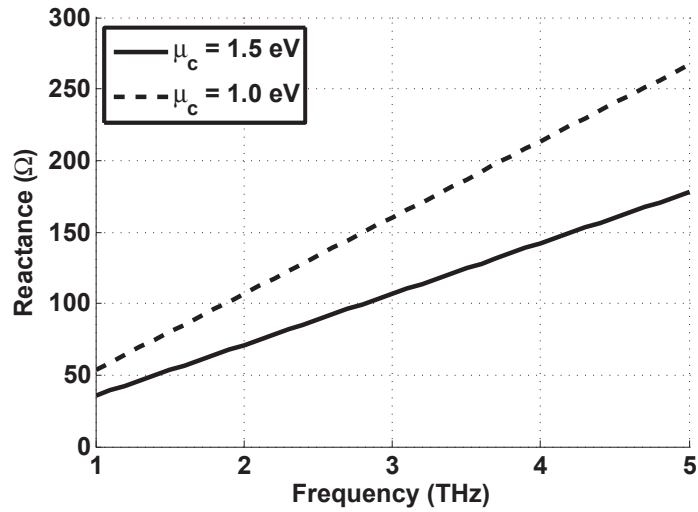
Figure 2.5. Surface reactance of a graphene monolayer with $\mu_c = 1.0$ eV and 1.5 eV.

Now that we have established the effect of the μ_c and τ on the graphene monolayer, the impact of introducing the graphene monolayer wrapped around the elliptical dielectric cylinder can be explored. As shown in Fig. 2.3, the introduction of the graphene monolayer causes a frequency shift in the resonance frequency of the strip dipole antenna. This frequency shift can be attributed to the imaginary part of the input impedance, which can be seen in Fig. 2.6. Below the resonance frequency of the uncloaked antenna, the imaginary part of the input impedance is capacitive. The graphene monolayer provides an inductive surface reactance at these frequencies. The combination of the capacitive reactance of the uncloaked antenna with the inductive graphene monolayer causes the 0 Ω reactance at a new

16

frequency. The uncloaked strip dipole antenna resonates at f_B, while the antenna cloaked
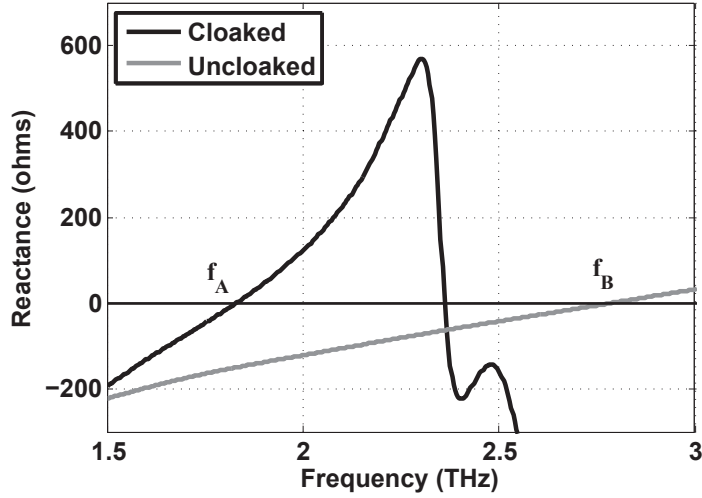
Figure 2.6. Input reactance of the strip dipole antenna with and without a graphene mono-layer with $\mu_c = 1.4$ eV and $\tau = 1.5$ ps.

with a graphene monolayer with $\mu_c = 1.4$ eV and $\tau = 1.5$ ps resonates at f_A. The cloaked antenna's resonance frequency can be changed simply by changing the μ_c of the graphene monolayer. This is a significant advantage in using these cloaked antennas, as they are com-
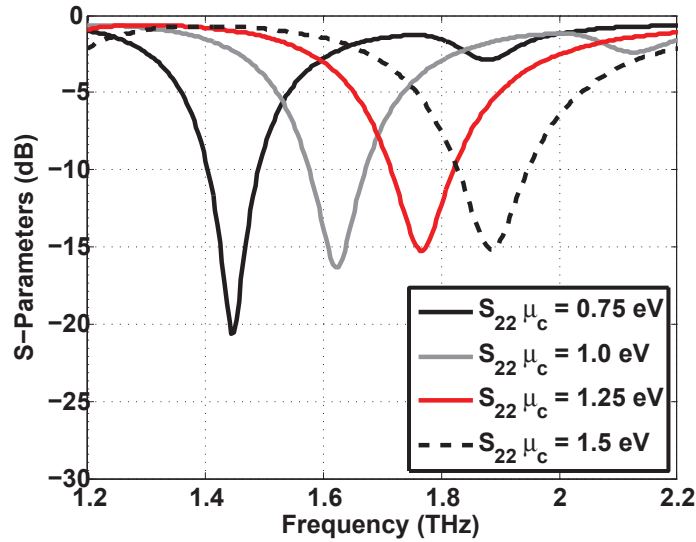
Figure 2.7. S_{11} for Antenna I with varying chemical potential $\mu_c = 0.75$ eV - 1.5 eV.

pletely tunable within a frequency range that can be seen in Fig 2.8, where the resonance

17

frequency of the antenna is between 1.83 THz to 2.32 THz for Antenna II. A similar range can be found for Antenna I, from 1.55 THz to 2.0 THz. It is important to note that while this adjustment is mainly revealed through the change in the resonance frequency of the antenna, there are other consequences to the changing of μ_c. This can be seen in Figs. 2.7 and 2.8, where the matching of the antenna is different for each μ_c. A lower μ_c represents
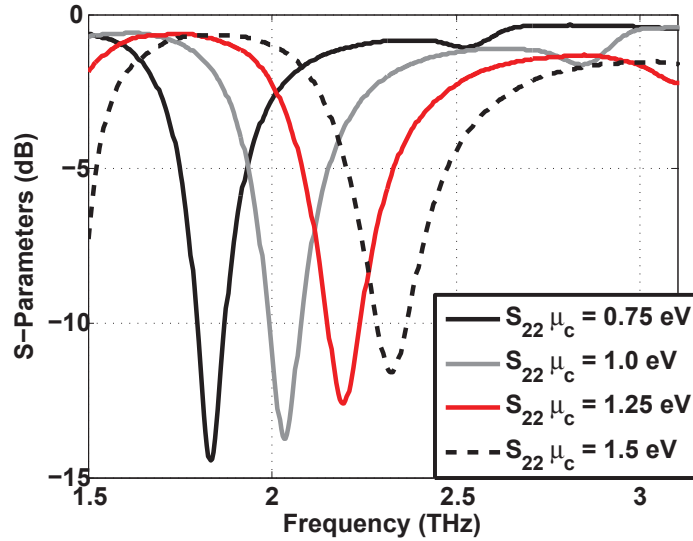
Figure 2.8. S_{22} for Antenna II with varying chemical potential $\mu_c = 0.75$ eV - 1.5 eV.

a change in the surface impedance of the antenna, where a higher μ_c represents a smaller inductance. Thus, the change in frequency when comparing the original uncloaked antenna to the cloaked antenna is smaller, which is desirable as this change has a direct impact on the efficiency of the antenna. A higher μ_c results in a higher efficiency, but we are limited to the range mentioned earlier, $\mu_c= 0.75$ eV - 1.5 eV. At significantly lower μ_c, the efficiency of the antennas is so reduced that the cloaking effect becomes irrelevant as the antenna is no longer a good radiator.

It has been established that there is a frequency range in which Antenna I and Antenna II where the antennas are good radiators. These frequency ranges can be adjusted by changing the length or other geometrical parameters of the antennas. These frequency ranges can also be observed through the real and imaginary parts of the input impedance.
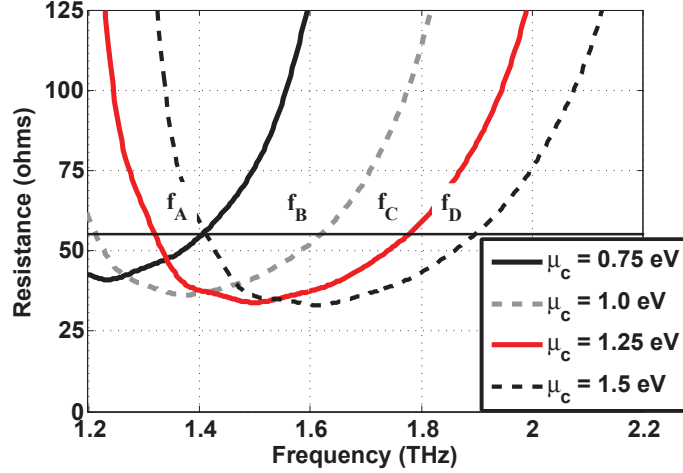
Figure 2.9. The input resistance for the cloaked Antenna I with varying chemical potential $\mu_c = 0.75$ eV - 1.5 eV. The line at 55 Ω represents the desired condition for the matching of the cloaked antenna.

In Figs. 2.9 - 2.12, the real and imaginary parts of the input impedances can be seen for Antenna I and II with varying μ_c. For the real part of the input impedance, there are two different resistances at which Antenna I and II are well matched.
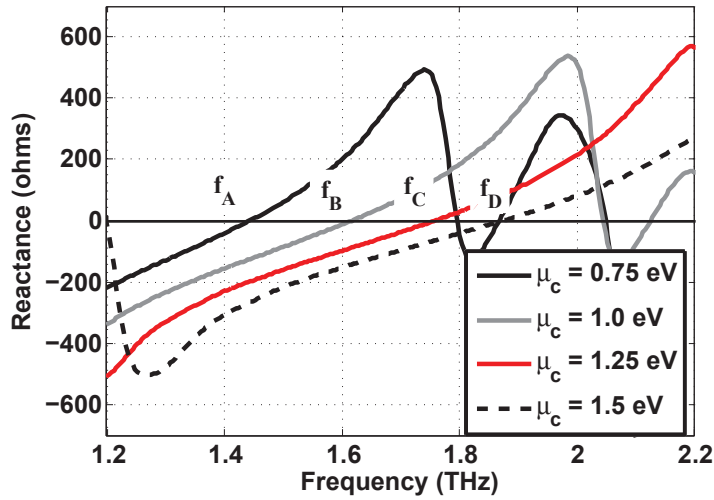
Figure 2.10. The input reactance for the cloaked Antenna I with varying chemical potential $\mu_c = 0.75$ eV - 1.5 eV. The line at 0 Ω represents the desired condition for the matching of the cloaked antenna.

It is important to note that the dimensions of the Antennas are the final dimensions
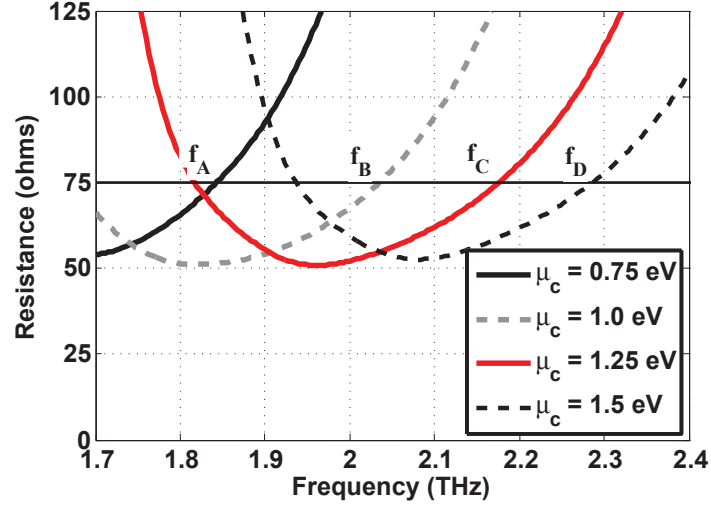
Figure 2.11. The input resistance for the cloaked Antenna II with varying chemical potential $\mu_c = 0.75$ eV - 1.5 eV. The line at 75 Ω represents the desired condition for the matching of the cloaked antenna.

chosen for the two Antennas, and as a result of some of the requirements of cloaking both antennas, some of the parameters in regards to the geometrical size of the antenna have been altered to provide the most significant cloaking effect.
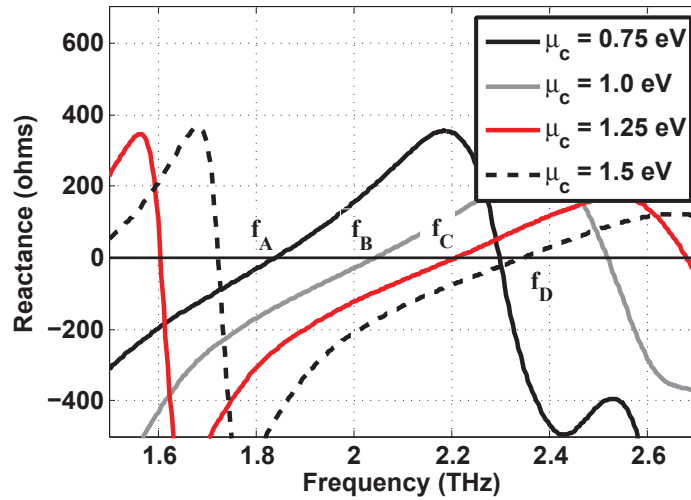
Figure 2.12. The input reactance for the cloaked Antenna II with varying chemical potential $\mu_c = 0.75$ eV - 1.5 eV. The line at 0 Ω represents the desired condition for the matching of the cloaked antenna.

This is most important to note for Antenna I, as the size of the ellipse is different

from Antenna II, which was chosen to provide the $R_{input} = 75$ Ω and $X_{input} = 0$ Ω. Antenna I has an input resistance of $R_{input} = 55$ Ω, which is represented by the horizontal line in Fig. 2.9. This happens as a direct result of changing the size of the dielectric elliptical cylinder, which has a size $a_1 = 1.75$ μm and $b_1 = 0.90$ μm, while the second antenna has an elliptical dielectric cylinder has size $a_2 = 2$ μm and $b_2 = 1.32$ μm. The reason for the smaller size of the ellipse for Antenna I will be discussed in the next section. Following from Antenna I, the resonance frequencies of Antenna II can be shown for different μ_c in Figs. 2.11 and 2.12, where f_A through f_D are the resonance frequencies for varying $\mu_c = 0.75$ eV to 1.5 eV.

2.2.2 Graphene Monolayer's Effect on ACS and RCS

The elliptically shaped graphene monolayer allows us to cloak the antennas at some frequency other than the radiating frequency. This can be seen by studying the ACS and RCS of the cloaked antenna. In the previous cloaking work, the focus was on the transverse magnetic (TM) polarization, so the plane wave will be created with the same goal, with the electric field vector directed along the antenna, with the propagation direction towards the widest side of the antenna. A TE polarized plane wave could be used to study the ACS and RCS if there is any interest in placing two antennas perpendicular to each other, which could be explored in future work. Additionally, it has been shown that the TM polarization is the dominant scattering mode, so by focusing on reducing the scattering from this polarization, a significant overall scatting reduction will occur. As before with the input impedance, the maxima and the minima in the RCS and ACS shift in frequency with the change in μ_c, increasing in frequency as the μ_c increases. For the cloaking of the first antenna, we are first interested in the resonance frequency, where the antenna is well matched as mentioned in the previous section. The graphene monolayer produces a second frequency where the ACS and RCS are at a minimum above that resonance frequency of the antenna. This reduction in scattering is the desired goal of the cloaked antenna, as this cloaked antenna will not disturb

Figure 2.13. RCS of Antenna I cloaked with graphene biased with varying chemical potential $\mu_c = 0.75$ eV - 1.5 eV.

the radiation patterns of the second antenna.

In Fig. 2.13, we can see the RCS of our cloaked Antenna I vs. μ_c. From this plot, a series of frequencies can be obtained, where for each curve, the RCS is at a minimum at a frequency higher than the resonance frequency. A set of 4 frequencies is obtained, $f_1 = 1.86$ THz, $f_2 = 2.11$ THz, $f_3 = 2.33$ THz, and $f_4 = 2.52$ THz. These four frequencies provide a range, from 1.86-2.52 THz, where our Antenna II can operate and have an omnidirectional radiation pattern. This range of frequencies also stems from the earlier limit on the μ_c of the Antenna, from $\mu_c = 0.75$ - 1.5 eV. The specific frequency can be selected solely by adjusting the μ_c of Antenna I. It is important to note that the changing of μ_c also changes the resonance frequency of the antenna. The difference in frequency between the resonance frequency and the cloaking frequency varies slightly depending on the μ_c, where a higher μ_c results in a larger difference in these two frequencies. In addition, due to the minimum $\mu_c = 0.75$ eV in an effort to keep the efficiency at a reasonable value, there is a minimum difference in the resonance frequencies of Antenna I and Antenna II, of about 0.3 THz. This difference in frequencies is also affected by the size of the ellipse used for the dielectric cylinder, where a balance must be chosen between the efficiency of the antenna and the difference in the

Figure 2.14. ACS of Antenna I cloaked with graphene biased with varying chemical potential $\mu_c = 0.75$ eV - 1.5 eV.

resonance and cloaking frequencies. By choosing the length and other geometrical parameters of Antenna II correctly, the antenna will resonate in this frequency band, while also having low RCS and ACS in the band of frequencies that Antenna I operates in.

Now in Fig. 2.14, the ACS of the Antenna I can be seen vs. μ_c with $L_1 = 44$ μm. There is always a maximum in the RCS and ACS of the antenna at its resonance frequency, as this indicates that the antenna is a good radiator. The overall efficiency is affected by the material properties of the graphene monolayer, which will be discussed in further detail later. At this frequency, the antenna is well matched as mentioned in the previous section. The first minimum in the ACS above the resonance frequency corresponds to the frequency where the mutual coupling will be at its minimum, as the power coupled to the antenna is directly related to how much the antenna absorbs from this plane wave excitation. This minimum at the ACS does not always occur at the same frequency as the minimum in the RCS. By adjusting the size of the ellipse, these minimum in the ACS and RCS can be brought closer together. This difference can be seen in Figs. 2.15 and 2.16. These two antennas have different lengths, 44 and 49.2 μm, to create the two antennas with the the same resonance frequency. Even with the same resonance frequency, by changing the size of the dielectric

23

Figure 2.15. ACS and RCS of an Antenna with L = 44 μm, a = 1.75 μm, and b = 0.90 μm cloaked with a graphene monolayer biased with μ_c = 1.5 eV.

elliptical cylinder, the frequency at which the antenna is cloaked changes. The minimum for the first dielectric elliptical cylinder can be seen by the vertical line at 2.47 THz and for the second dielectric elliptical cylinder at 2.62 THz. This difference in the frequency at which the antenna will be cloaked will have an important impact on creating the final Antenna I and II to be used, as there are several things which must be balanced to provide the antenna with good matching and the required behavior in the RCS and ACS.

Now that we have the procedure for making one antenna, the second antenna can be created through . It is important to note that previously, we were interested in the RCS and ACS at some frequency above the resonance frequency. For Antenna II, the higher frequency antenna, we are interested in the RCS and ACS being a minimum at a frequency below the resonance frequency. The frequency that this occurs at can again be adjusted by the μ_c of the graphene monolayer, but overall, the RCS is much lower below the resonance frequency of the antenna, due to the smaller size of the antenna in relation to the wavelength at these lower frequencies. This can be seen in Figures 2.17 and 2.18, the RCS and ACS of Antenna II vs. μ_c with L_2 = 40.8 μm. While the RCS and ACS of Antenna I indicate a specific frequency where Antenna II must operate to benefit from the cloak, only the ACS

24

Figure 2.16. ACS and RCS of an Antenna with L $= 49.2$ μm, $a = 2.0$ μm, and $b = 1.32$ μm cloaked with a graphene monolayer biased with $\mu_c = 1.5$ eV.
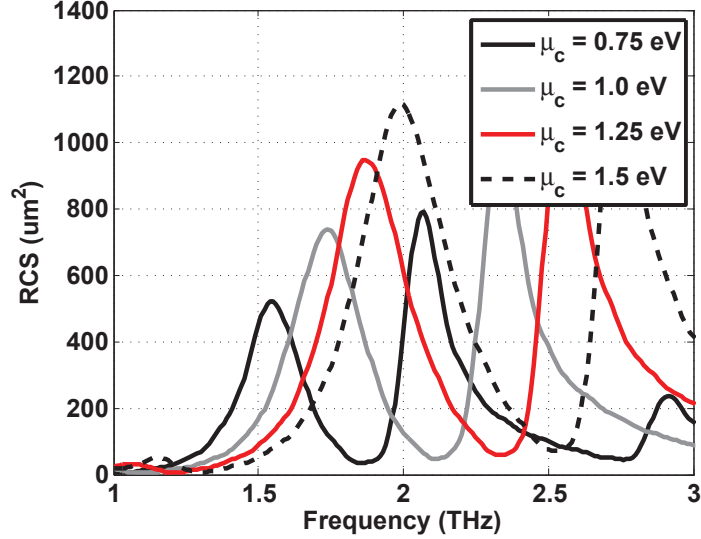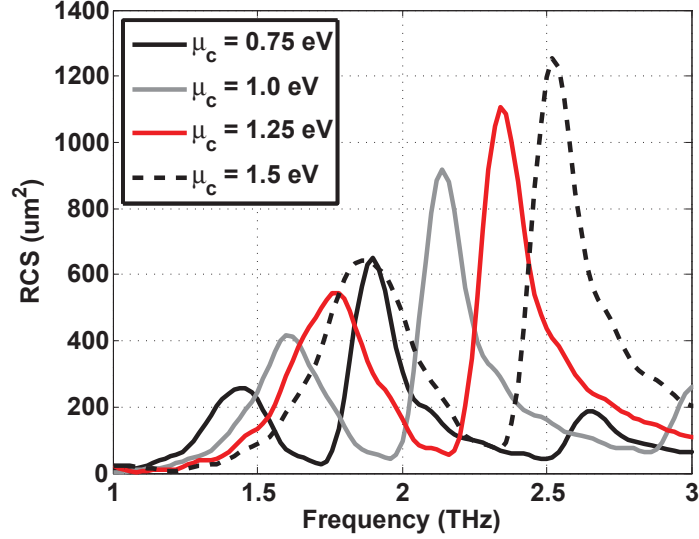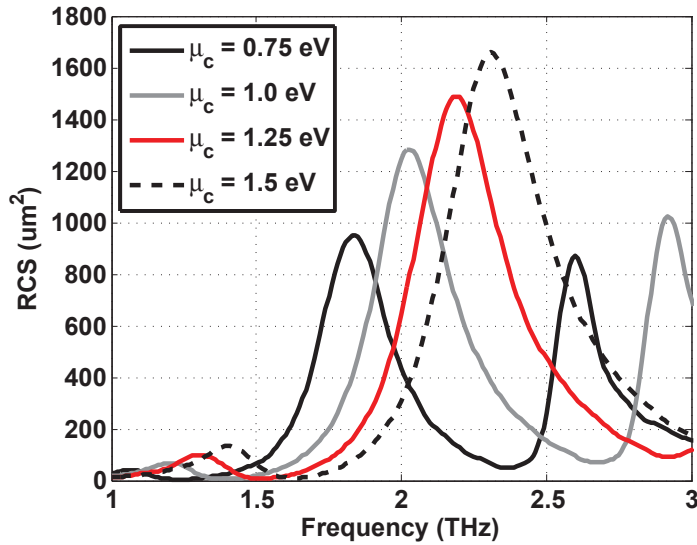

Figure 2.17. RCS of Antenna II cloaked with graphene biased with varying chemical potential $\mu_c = 0.75$ eV - 1.5 eV.

of Antenna II gives an indication of the optimal frequency for Antenna I. If the resonance frequencies of the two antennas are too close, then the radiation patterns of Antenna I will still be perturbed. Using Fig. 2.18, the frequency range of Antenna I can be seen when the ACS of Antenna II is at a minimum. The length of Antenna II should be adjusted to ensure that the minimum in the ACS below the resonance frequency of Antenna II is in the range

of frequencies that were established when the length of Antenna I was picked.
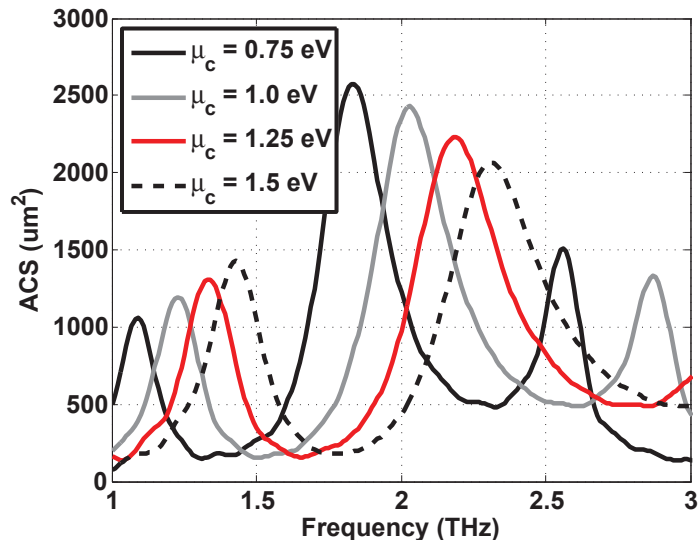
Figure 2.18. ACS of Antenna II cloaked with graphene biased with varying chemical potential $\mu_c = 0.75$ eV - 1.5 eV.

2.2.3 Final Design for Antenna I and Antenna II

There are several points of interest when creating the final designs for Antenna I and II. In the earlier stages of the design process, there was only one size for the elliptical dielectric cylinder, with $a = 2.0$ μm and $b = 1.32$ μm. This size of the elliptical cylinder was chosen for the usefulness of the matching provided by this sized elliptical cylinder with the graphene monolayer. As it was shown in Figs. 2.12 and 2.11, when this size is chosen for the elliptical cylinder, the input impedance of the antenna was almost exactly $R_{input} = 75$ Ω and $X_{input} = 0$ Ω. This was desirable for the port made in CST as this input impedance is a common goal for the matching of antennas. By changing the size of the ellipse to $a = 1.75$ μm and $b = 0.90$ μm, the antenna became cloaked more effectively at a specific frequency. This was a problem with previous designs where the frequency at which the RCS and ACS were at a minimum were not quite the same.

In the same way, in Fig. 2.15, there is a vertical line at 2.47 THz indicating the
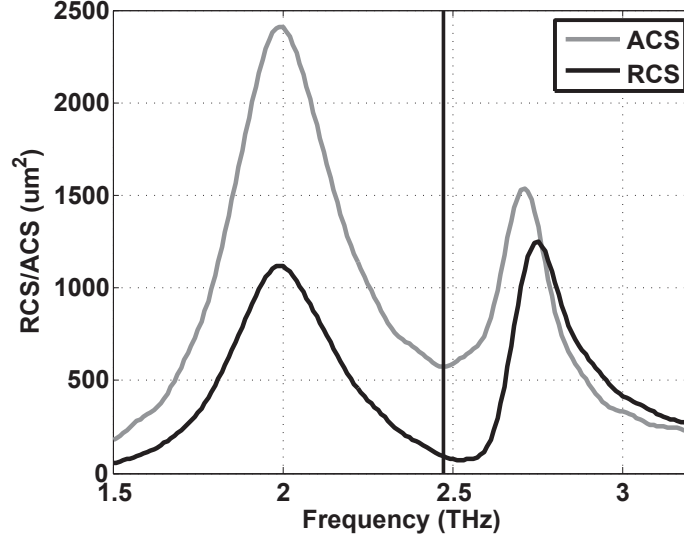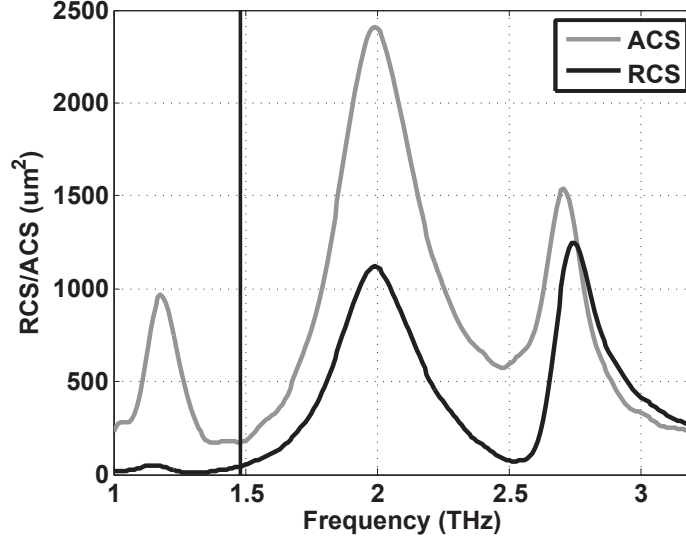
Figure 2.19. ACS and RCS of an Antenna with L = 44 μm, a = 1.75 μm, and b = 0.90 μm cloaked with a graphene monolayer biased with μ_c = 1.5 eV.

minimum in the ACS for this antenna with a smaller elliptical dielectric cylinder, and the minimum in the RCS occurs at 2.52 THz. This represents a small improvement in the difference between these two frequencies, which will further be improved upon in the final design. This is also a concern for Antenna II, as the changing of the size of the elliptical dielectric cylinder also affects the frequency at which the ACS and RCS are a minimum below the resonance frequency. In Figs. 2.19 and 2.20, the RCS and ACS of the same antenna is shown as in Figs. 2.15 and 2.16. Now the point of interest is below the resonance frequency of the antenna. The same two dimensions for the size of the elliptical dielectric cylinder have an impact on where the minimum in the ACS and RCS is at a minimum. The frequency where the ACS is at a minimum is shown in Figs. 2.19 and 2.20 by the vertical lines. In Fig. 2.19, this line is at 1.48 THz, while in Fig. 2.20, the line is at 1.54 THz. The difference between the resonance frequency and these minimums in the ACS below the resonance frequency are important to keep in mind, as this indicates how close in frequency the two antennas can operate. Previously, it was mentioned that with the dielectric elliptical cylinder having size a = 1.75 μm and b = 0.90 μm has an impact on the difference between the resonance frequency and the frequency where the antenna is cloaked, where the minimum

27

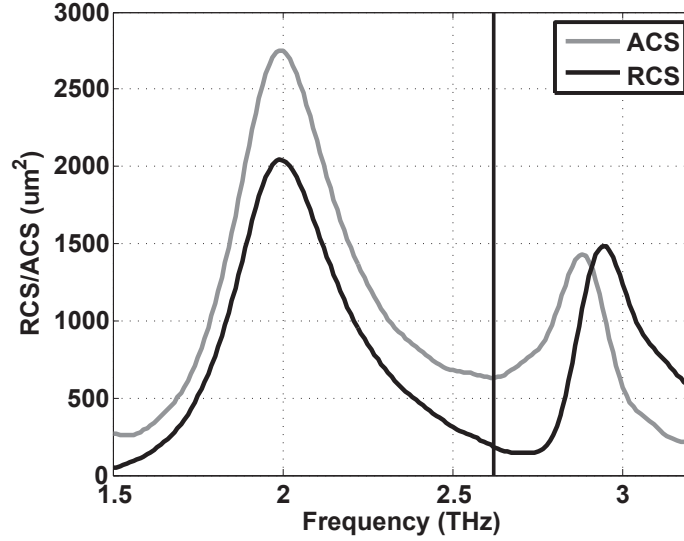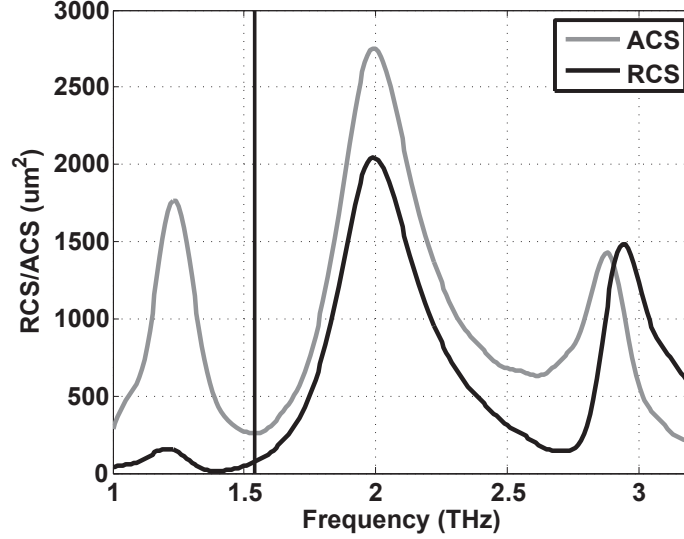Figure 2.20. ACS and RCS of an Antenna with L = 49.2 μm, a = 2.0 μm, and b = 1.32 μm cloaked with a graphene monolayer biased with μ_c = 1.5 eV.

difference is about 0.3 THz. In the same way, the geometrical parameters have an impact on the minimum difference between the resonance frequency and the frequency at which the Antenna II will be cloaked.

With this new information about the geometrical parameters of the antennas, we can now complete our process to create our Antenna I. For the final Antenna, the following
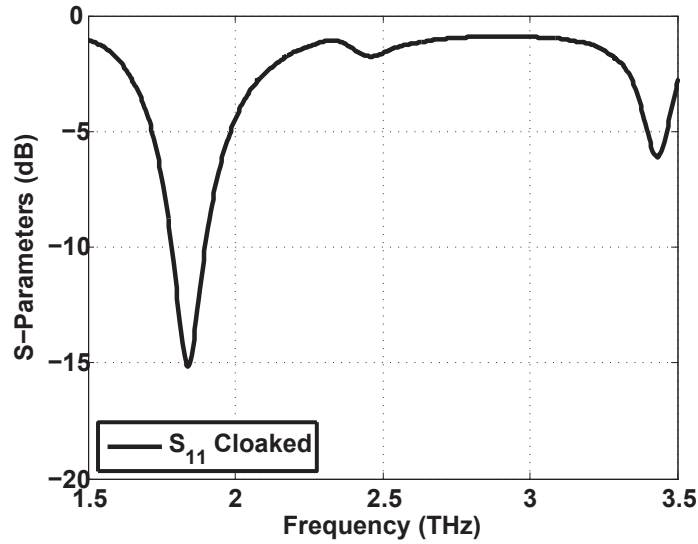
Figure 2.21. S_{11} for the cloaked Antenna I with L_1 = 44 μm.

28
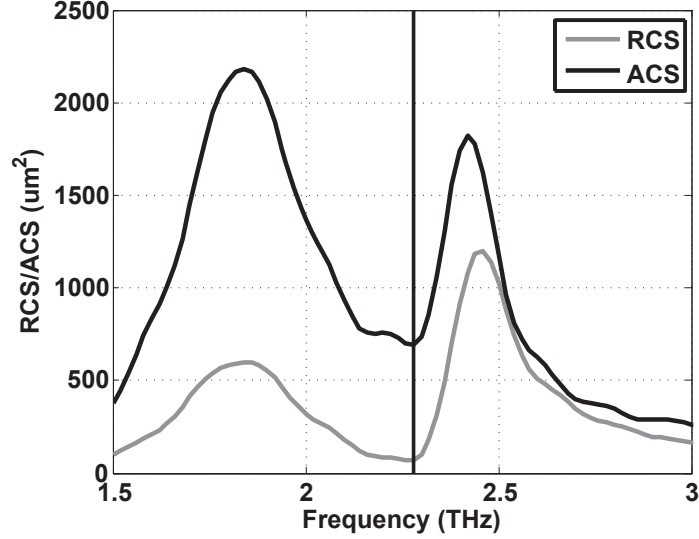
Figure 2.22. ACS and RCS of the final Antenna I with $L_1 = 44$ μm cloaked with graphene.

parameters were used: $\mu_c = 1.4$ eV, $\tau = 1.5$ ps, $L_1 = 44$ μm, $W = 3$ μm, $a = 1.75$ μm, $b = 0.901$ μm, and $\epsilon_r = 4$. The S_{11} of the final Antenna I can be seen in Fig. 2.21. The resonance frequency of antenna I is $f_1 = 1.83$ THz. The minimum in the RCS occurs at the vertical line in 2.22 at 2.26 THz and the minimum in the ACS occurs at 2.28 THz.

With the information provided by the final design for Antenna I, Antenna II can now also be constructed. The key piece of information to create Antenna II is the frequency at which the ACS and RCS are at a minimum. It is important to note that while these frequencies are important to deciding the resonance frequency of Antenna II, there is some adjustment due to the difference in the nature of the excitation. The RCS and ACS are calculated through the use of the previously mentioned TM polarized plane wave excitation, but in the case of cloaking the two antennas, the excitation from the strip dipole antenna is different from the plane wave due to the close spacing of the two antennas, and thus some adjustment in the creation of our Antenna II is needed.
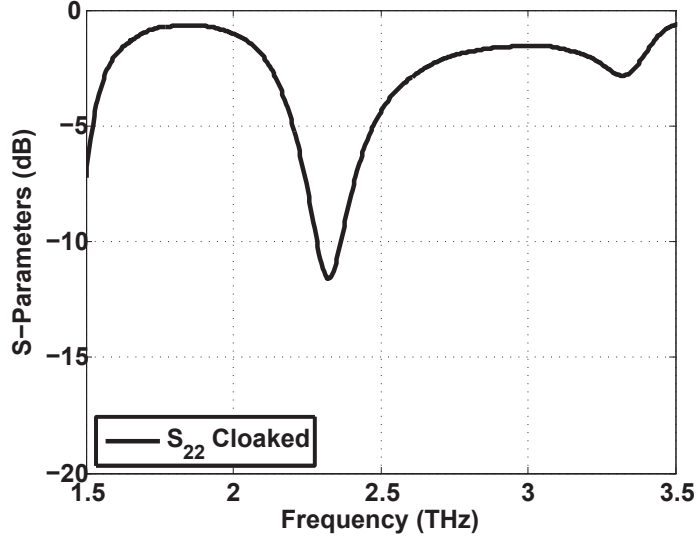
Figure 2.23. S_{22} for the cloaked Antenna II with $L_1 = 41.8$ μm.
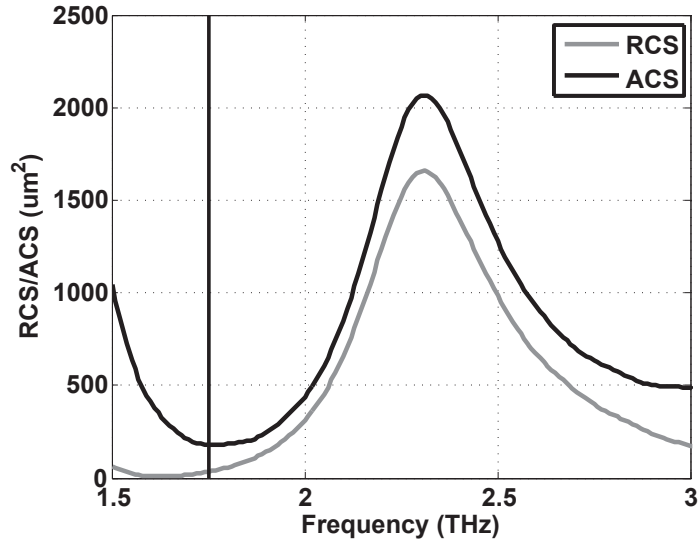
Figure 2.24. ACS and RCS of the final design Antenna II cloaked with graphene.

After this adjustment, a final design for Antenna II was reached: $\mu_c = 1.5$ eV, $\tau = 1.5$ ps, $L_1 = 40.8$ μm, $W = 3\mu$m $a = 2$ μm, $b = 1.322$ μm, and $\epsilon_r = 4$. Antenna II resonates at $f_2 = 2.31$ THz, which can be seen in Fig. 2.23, and has a minimum in the ACS at 1.76 THz which is shown by the line in Fig. 2.24. The 3D radiation patterns of the isolated Antenna I and II at their respective resonance frequencies are shown in Fig. 2.25. As mentioned before, there is some adjustment in the creation of both antennas which happens as a result of the

30

close proximity of the two antennas when placed together.
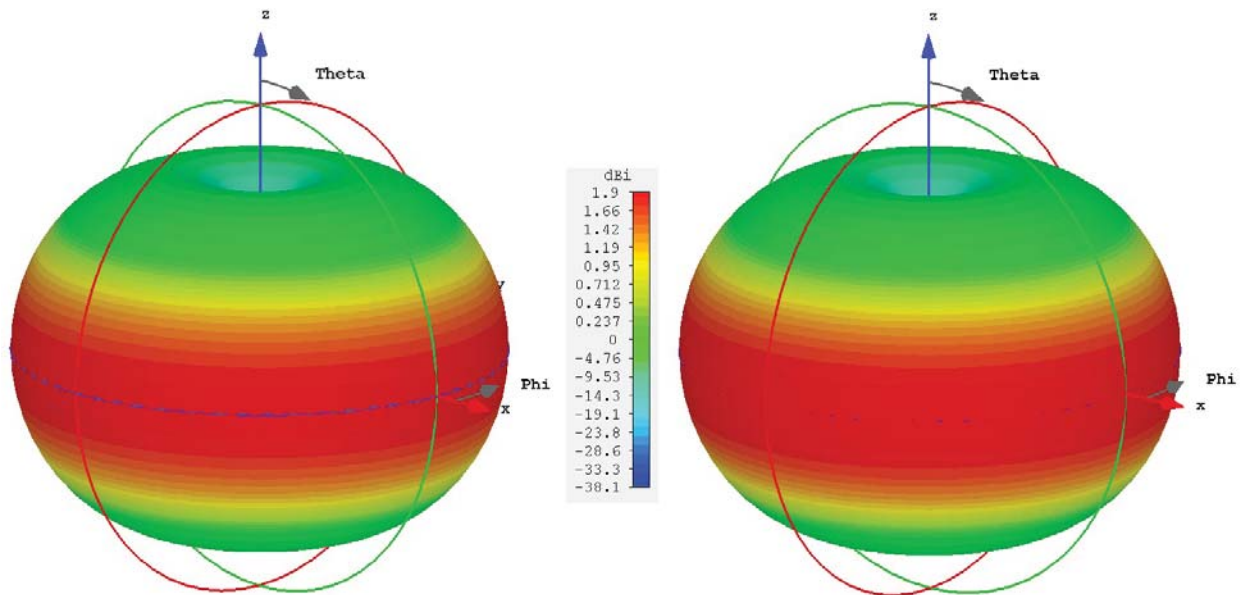
Figure 2.25. 3D radiation patterns of the Cloaked Antenna I and II when they are isolated, at frequencies $f_1 = 1.83$ and $f_2 = 2.31$ THz.

2.3 Cloaked Antenna Results

The final step is to put the two final antenna designs together and study the effect they have on each other. For the initial results, a distance of $d = \lambda/10.92$ was chosen, as this distance is electrically small. More results will follow exploring additional distances, $d = \lambda/32.8$, $d = \lambda/2$, and $d = \lambda$. At larger distances, the mutual coupling between the antennas is reduced, and some array factors are formed which cause differently shaped patterns in the uncloaked antennas. Previously, it was mentioned that the uncloaked antenna and the cloaked antenna resonate at different frequencies due to the addition of the graphene monolayer. To compare the uncloaked vs. the cloaked case, the final cloaked antennas are created first, and when their resonance frequencies f_1 and f_2 are known, equivalent uncloaked antennas are created which resonate at the same f_1 and f_2. These antennas will not be the same length due to the influence of the graphene monolayer. For this first case, the uncloaked

antennas have lengths $L_3 = 65.2$ μm, $L_4 = 51$ μm, and $W = 3$ μm, which resonate at $f_1 = 1.83$ THz and $f_2 = 2.31$ THz.

2.3.1 Closely Spaced Antennas (Case I)

First, the S-parameters of the two cloaked antennas are shown in Fig 2.26. Both Antenna I and II are well matched at their resonance frequencies, with Antenna I having $S_{11} = $ -13.9 dB and Antenna II having $S_{22} = $ -28.5 dB. The two antennas have significantly reduced mutual coupling throughout the frequency range of interest. In particular, there is a -16.5 dB reduction in the mutual coupling at the resonance frequency of Antenna I, f_1 = 1.83 THz and a 11.2 dB reduction at the resonance frequency of Antenna II, $f_2 = 2.31$ THz. The next major point of interest for these two antennas is the radiation patterns of the uncloaked case vs. the cloaked case.
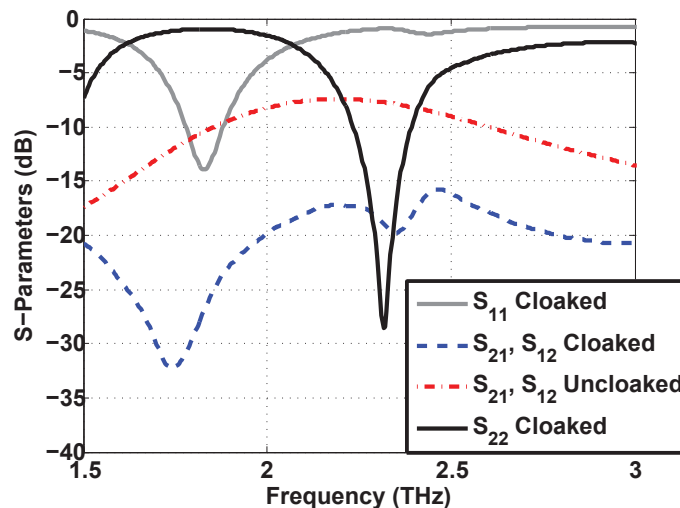
Figure 2.26. S-Parameters of the Cloaked Antenna I and II at a distance $d = \lambda/10.92$ ($d = 15$ μm).

The 3D radiation patterns of the uncloaked antennas can be seen in 2.27. As the antennas are placed very close together, the radiation patterns become highly disturbed. There is some interesting behavior that happens as a result of the placement of the antennas. The uncloaked Antenna I, which is longer, radiates in the direction of the shorter Antenna

II. This indicates that Antenna II is behaving as a director, similar to a Yagi-Uda antenna. In a similar way, Antenna II radiates away from the longer Antenna I, which means Antenna I is acting as a reflector.

Figure 2.27. 3D radiation patterns of the uncloaked Antenna I and II when placed at a distance $d = \lambda/10.92$ ($d = 15$ μm) at the resonance frequencies $f_1 = 1.83$ THz and $f_2 = 2.31$ THz.

Figure 2.28. 3D radiation patterns of the cloaked Antenna I and II when placed at a distance $d = \lambda/10.92$ ($d = 15$ μm) at the resonance frequencies $f_1 = 1.83$ THz and $f_2 = 2.31$ THz.

(a) E-Plane of Antenna I   (b) H-Plane of Antenna I

(c) E-Plane of Antenna II   (d) H-Plane of Antenna II

Figure 2.29. E and H-Plane radiation pattern for the isolated, uncloaked, and cloaked Antenna I and II in the presence of each other at $f_1 = 1.83$ THz (a,b) and for Antenna II at $f_2 = 2.31$ THz (c,d) at a distance $d = \lambda/10.92$ ($d = 15$ μm).

The 3D radiation patterns of the cloaked antennas can be seen in Fig. 2.28. These patterns represent a significant restoration of the patterns seen in the isolated case in Fig.

2.25. This restoration can also be seen more clearly by looking specifically at the E-plane and H-plane cuts of the radiation patterns. In Fig. 2.29, the isolated (gray), uncloaked (red), and cloaked (black) radiation patterns are shown for Antennas I and II at their resonance frequencies. It is interesting to note that the patterns of the cloaked antennas represent the same shape as the uncloaked patterns, but are significantly improved when compared with the uncloaked case. Now other antenna spacings can be looked at, the effect of the increased spacing between the antennas is most reflected in the radiation patterns of the uncloaked and cloaked antennas.

2.3.2 Half Wavelength Spaced Antennas (Case II)

The transition from the closely spaced antennas to the half lambda spacing emphasizes a few things of interest about the cloaked antennas. The two antennas designed in the previous section are again used here, but they are placed further away at a distance $d = \lambda/2$ ($d = 84$ μm). The S-parameters of the two antennas are shown in Fig. 2.30, where it
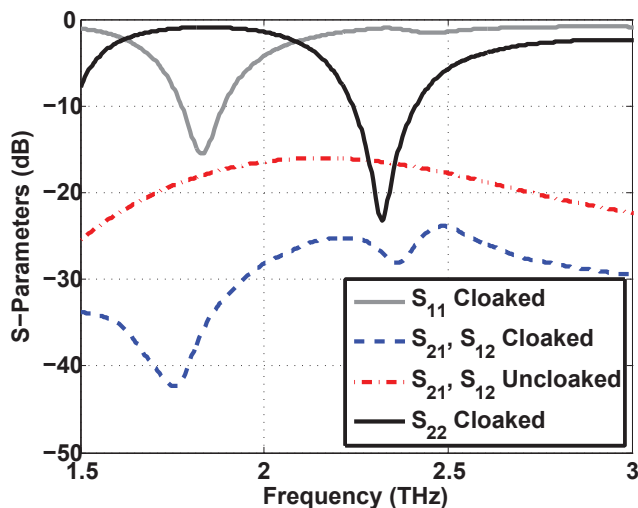
Figure 2.30. S-Parameters of the Cloaked Antenna I and II at a distance $d = \lambda/2$ ($d = 82$ μm).

is displayed that the matching of the antennas has not been affected by this increase in the distance betweeen the two antennas, with $S_{11} = $ -15.4 dB at $f_1 = 1.83$ THz, and $S_{22} = $ -23.19

dB at $f_2 = 2.31$ THz. As expected, the increase in distance between the antennas causes a decrease in the mutual coupling between the antennas.
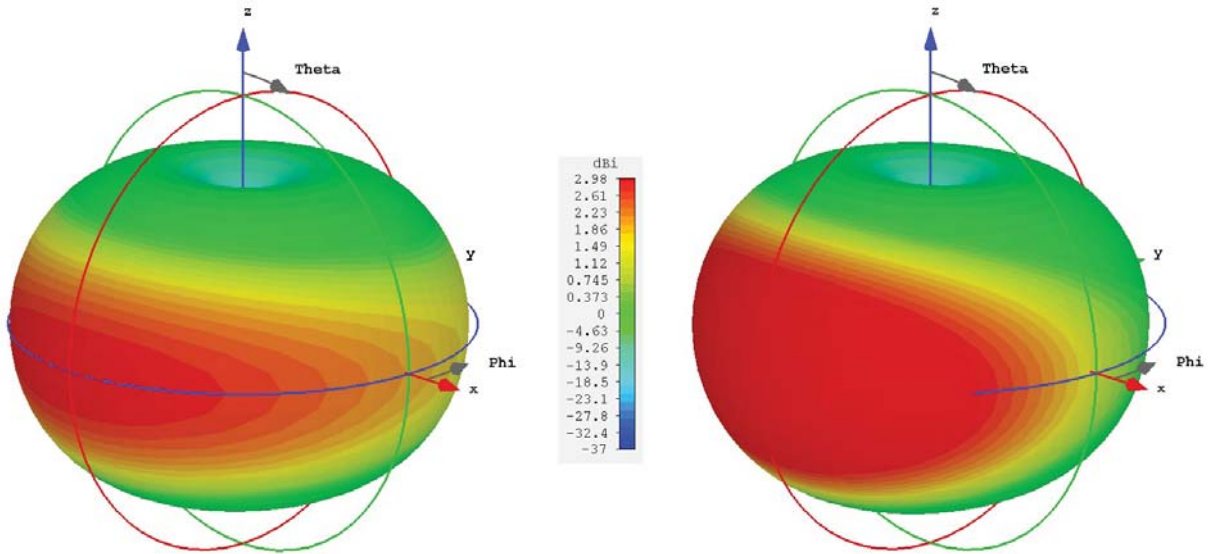

Figure 2.31. 3D radiation patterns of the uncloaked Antenna I and II when placed at a distance $d = \lambda/2$ ($d = 82$ μm) at the frequencies $f_1 = 1.83$ THz and $f_2 = 2.275$ THz.
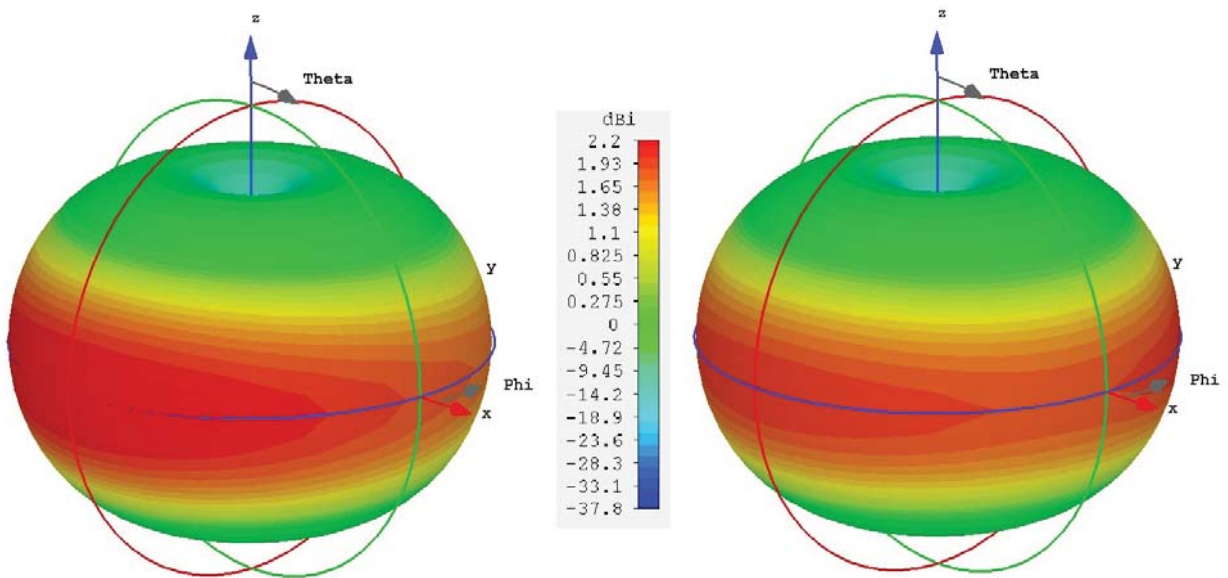

Figure 2.32. 3D radiation patterns of the cloaked Antenna I and II when placed at a distance $d = \lambda/2$ ($d = 82$ μm) at the frequencies $f_1 = 1.83$ THz and $f_2 = 2.275$ THz.

(a) E-Plane of Antenna I

(b) H-Plane of Antenna I
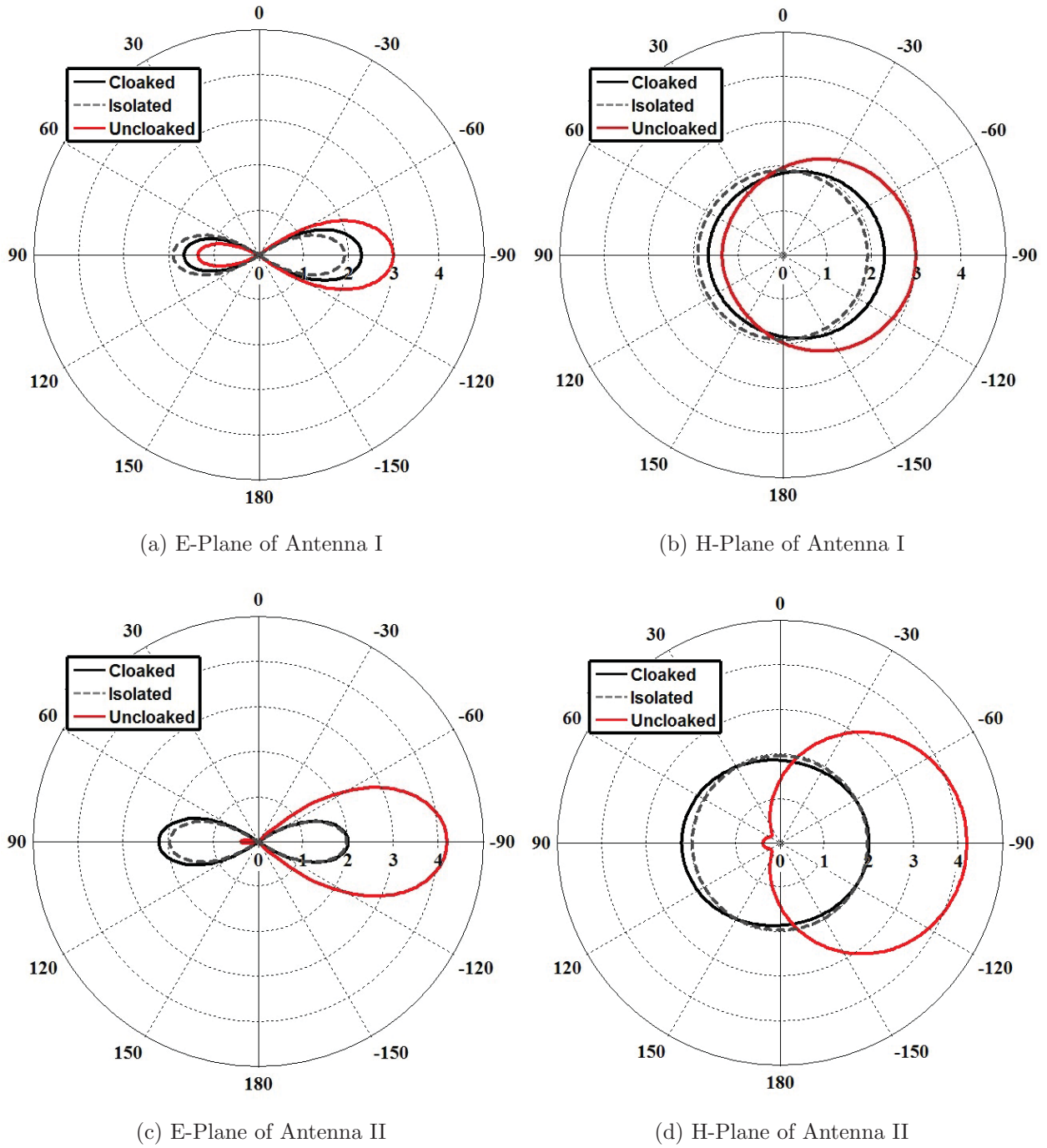
(c) E-Plane of Antenna II

(d) H-Plane of Antenna II

Figure 2.33. E and H-Plane radiation pattern for the isolated, uncloaked, and cloaked Antenna I and II in the presence of each other at $f_1 = 1.83$ THz (a,b) and for Antenna II at $f_2 = 2.31$ THz (c,d) at a distance $d = \lambda/2$ ($d = 82$ μm).

The reduction in the mutual coupling between has improved, from a -16.5 dB reduction for the closely spaced antennas in the previous section, to now a -18.2 dB reduction at

$f_1 = 1.83$ THz, and a -10.4 dB reduction at $f_2 = 2.31$ THz. The next point of interest for the cloaking of the antennas is the radiation patterns. The 3D radiation patterns for the uncloaked and cloaked antennas at a distance $d = \lambda/2$ are shown in Figs. 2.31 and 2.32.

The first thing to be noted is that the radiation patterns of the uncloaked antennas are a completely different shape when compared to the closely spaced antennas of the first case. An array factor is created due to the increased distance between the two antennas. The cloaked radiation patterns are similarly shaped to the uncloaked patterns with significantly less directivity, at $f_1 = 1.83$ THz, and at $f_2 = 2.275$ THz.

The frequency at which the radiation patterns were taken for Antenna II has changed for this spacing due to the fact that there was a frequency shift in the best frequency for the most omni-directional radiation pattern. This new frequency f_2 agrees much more with the original ACS and RCS, which had their respective minimums at 2.26 and 2.28 THz respectively. Antenna II is still very well matched at this frequency, so the performance of the antenna has not been affected by this change in frequency. This shift could stem from the increased distance between the antennas causing the radiation from the other antenna behaving more like a plane wave, which is how the ACS and RCS were calculated. The differences between the closely spaced antennas and the half lambda spaced antennas will continue in the next section, where the spacing increases to $d = \lambda$.

2.3.3 One Wavelength Spaced Antennas (Case III)

The distance between the two has now been increased to $d = \lambda$ ($d = 164$ μm), and the results follow in this section. First the S-parameters can be seen in Fig. 2.34 with S_{11} = -15.4 dB at $f_1 = 1.83$ THz, and $S_{22} = -22.9$ dB at $f_2 = 2.31$ THz. As in the half-lambda case, the further increased spacing has led to a continued decrease in the mutual coupling, with a -17.7 dB reduction at $f_1 = 1.83$ THz, and a -10.6 dB reduction at $f_2 = 2.31$ THz. This reduction in the mutual coupling is similar in magnitude to the half lambda case.
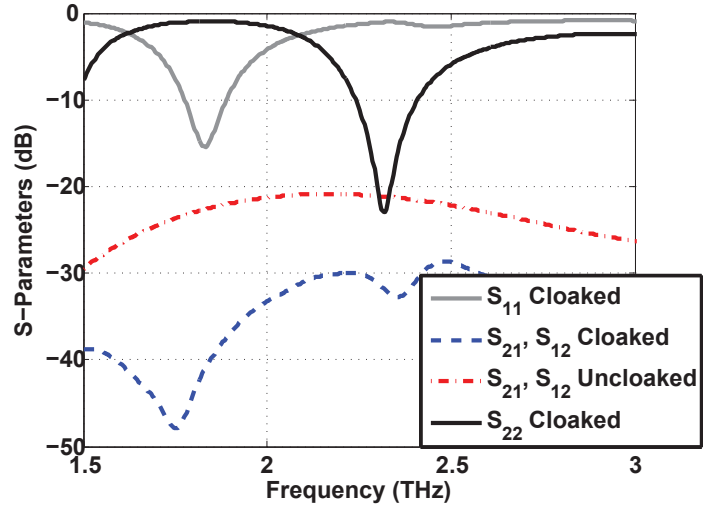
Figure 2.34. S-Parameters of the Cloaked Antenna I and II at a distance $d = \lambda$ ($d = 164$ μm).

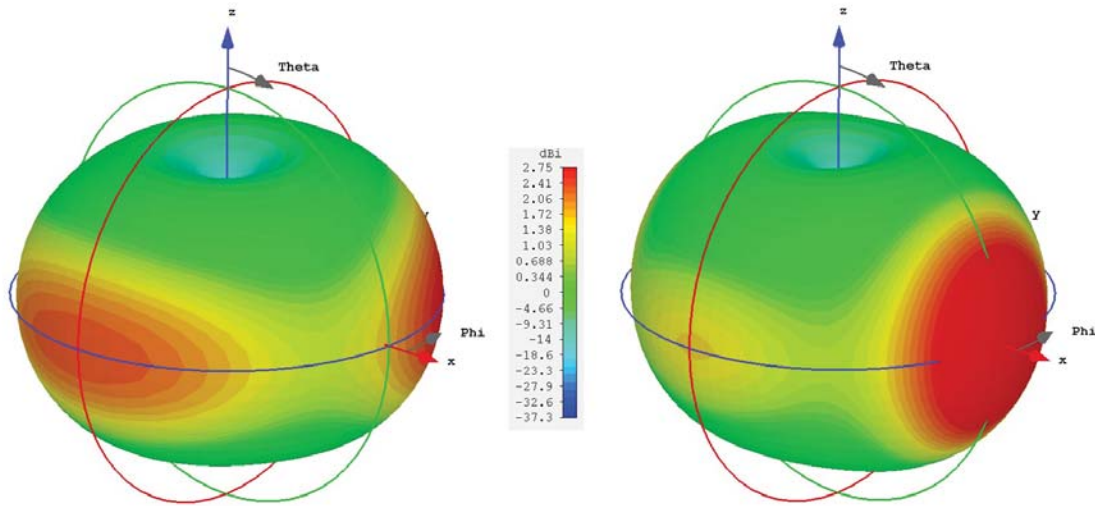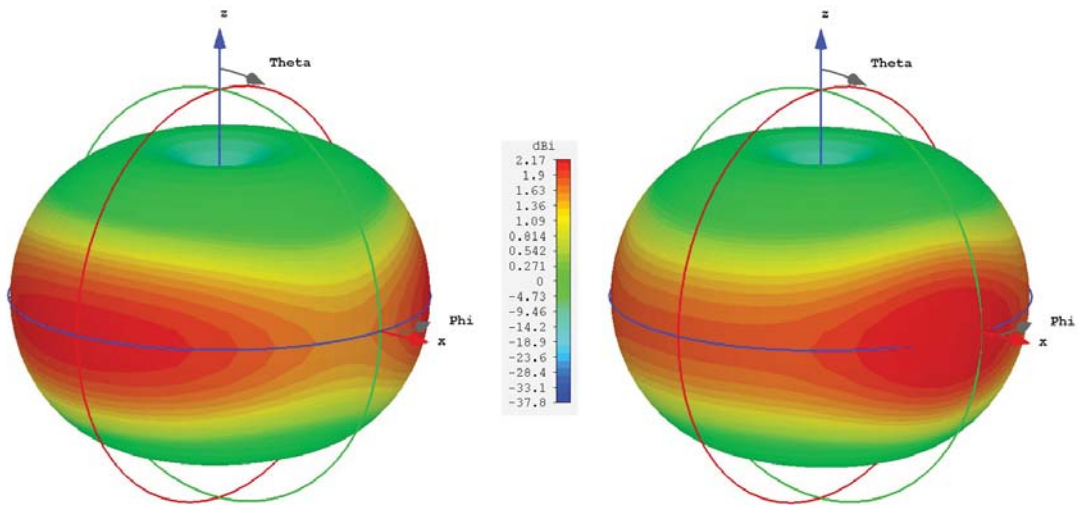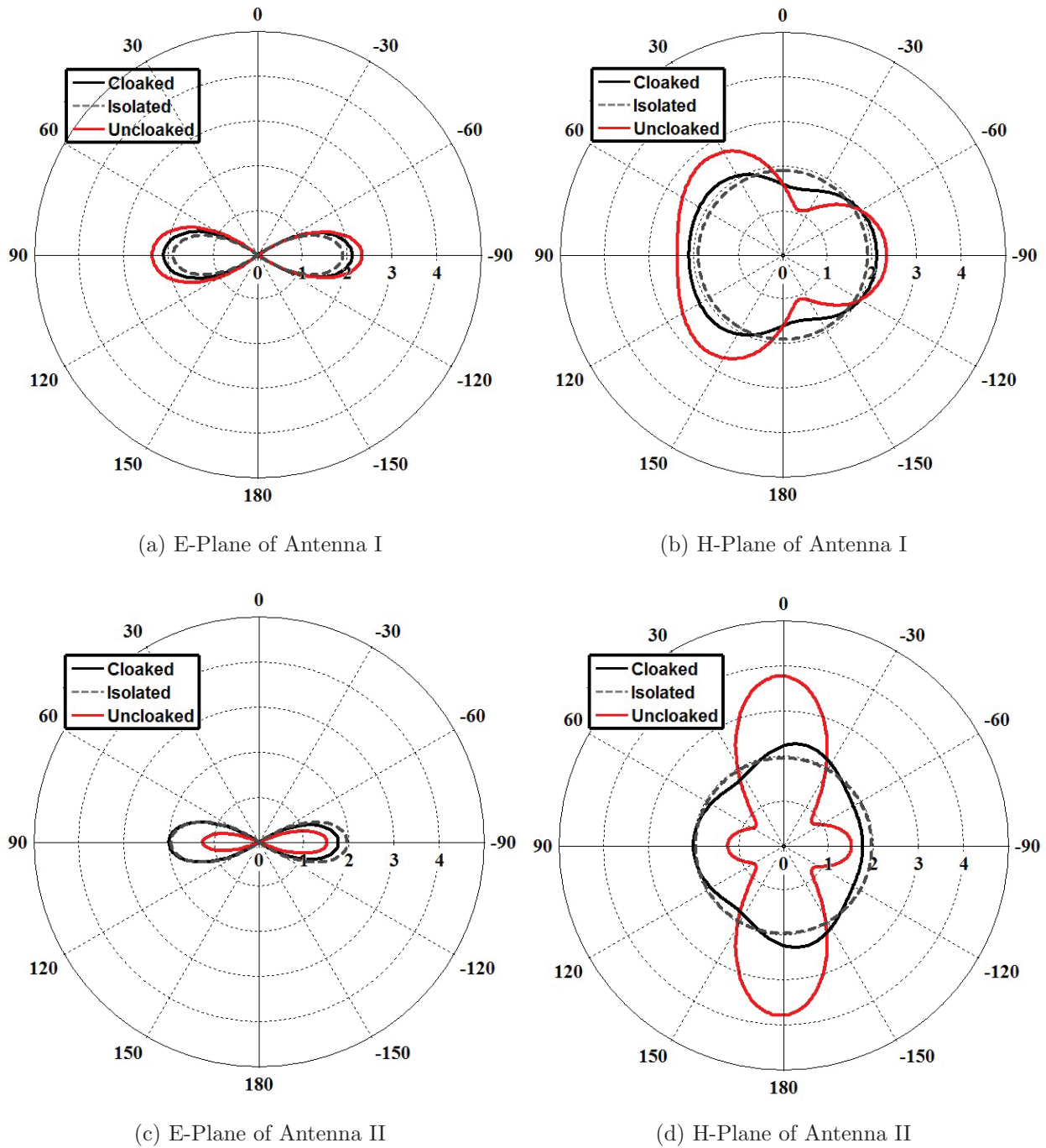Figure 2.35. 3D radiation patterns of the uncloaked Antenna I and II when placed at a distance $d = \lambda$ ($d = 164$ μm).

Figure 2.36. 3D radiation patterns of the cloaked Antenna I and II when placed at a distance $d = \lambda$ ($d = 164$ μm).

In the same way as the half-lambda case, the increase in the distance causes a differently shaped pattern due to the different antenna spacing, with up to 6 lobes in the uncloaked radiation pattern of Antenna II at 2.275 THz. The 3D radiation patterns for the two antennas can be seen in Figs. 2.35 and 2.36.

As in the half lambda case, the patterns are still significantly restored, but with the similar pattern to the uncloaked pattern. This can be seen most clearly in the H-Plane of Antenna II, which can be seen in part (d) of Fig. 2.37. In this figure, the radiation pattern of the cloaked Antenna II is very close to the original isolated radiation pattern, but there are some small lobes in the pattern that occur at the same places as the uncloaked case. In each case, the patterns of the cloaked antenna are always related to the patterns of the uncloaked antenna. This indicates that the cloaking effect is very robust in that any unusual radiation pattern can be restored to the original pattern thanks to the graphene monolayer cloak.

(a) E-Plane of Antenna I

(b) H-Plane of Antenna I

(c) E-Plane of Antenna II

(d) H-Plane of Antenna II

Figure 2.37. E and H-Plane radiation pattern for the isolated, uncloaked, and cloaked Antenna I and II in the presence of each other at $f_1 = 1.83$ THz (a,b) and for Antenna II at $f_2 = 2.31$ THz (c,d) at a distance $d = \lambda$ ($d = 164$ μm).

2.3.4 Extremely Close Spaced Antennas (Case IV)

The final case for a different spacing is detailed below, this is the case of two extremely close spaced antennas. The distance between the antennas is $d = \lambda/32.8$ ($d = 5$ μm). This distance represents the minimum distance required between the antennas, as any distance closer than this drastically increases the mutual coupling between the antennas to the point that the antennas no longer radiate well and a frequency shift also occurs. The cause for this minimum distance between the antennas is unknown so far, and further research would be needed to investigate this phenomenon. As mentioned before, the distance between the
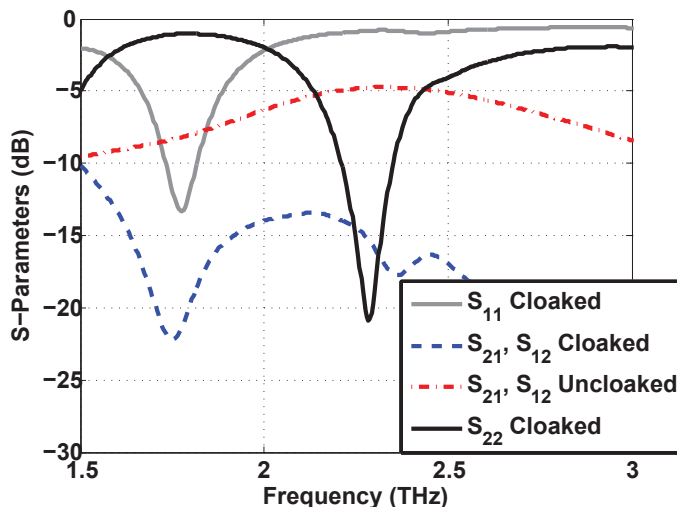
Figure 2.38. S-Parameters of the Cloaked Antenna I and II at a distance $d = \lambda/32.8$ ($d = 5$ μm).

two antennas is measured from the center of Antenna I to the center of Antenna II, so the distance from edge to edge of the antennas is much smaller, in this case it is $d_{edge} = 2.77$ μm.

The S-parameters of the two antennas are slightly affected by this extremely close spacing, and can be seen with 2.38 with $S_{11} = $ -13.2 dB at $f_1 = 1.83$ THz, and $S_{22} = $ -16.7 dB at $f_2 = 2.31$ THz. The radiation patterns are in Figs. 2.39 - 2.41. The closer spacing of the antennas has caused the radiation patterns of the uncloaked case to be less directive, with a maximum directivity of 2.41 dB at this closer spacing, compared to a maximum directivity

of 2.99 dB at the original spacing of $d = \lambda/10.92$. As a result the cloaked antenna patterns are very close to the isolated radiation patterns.
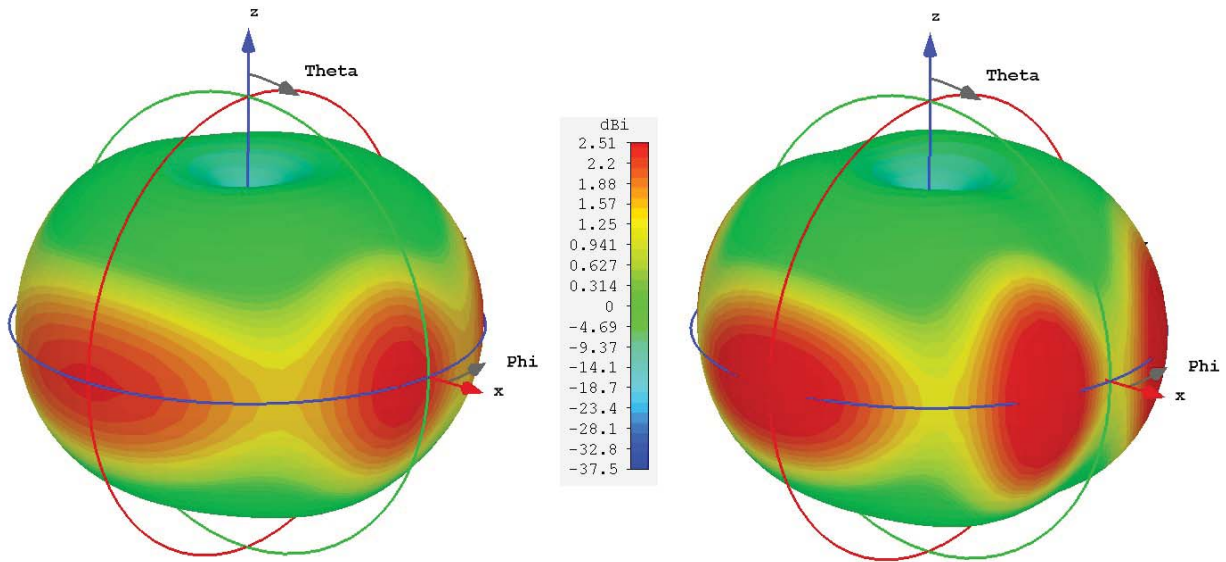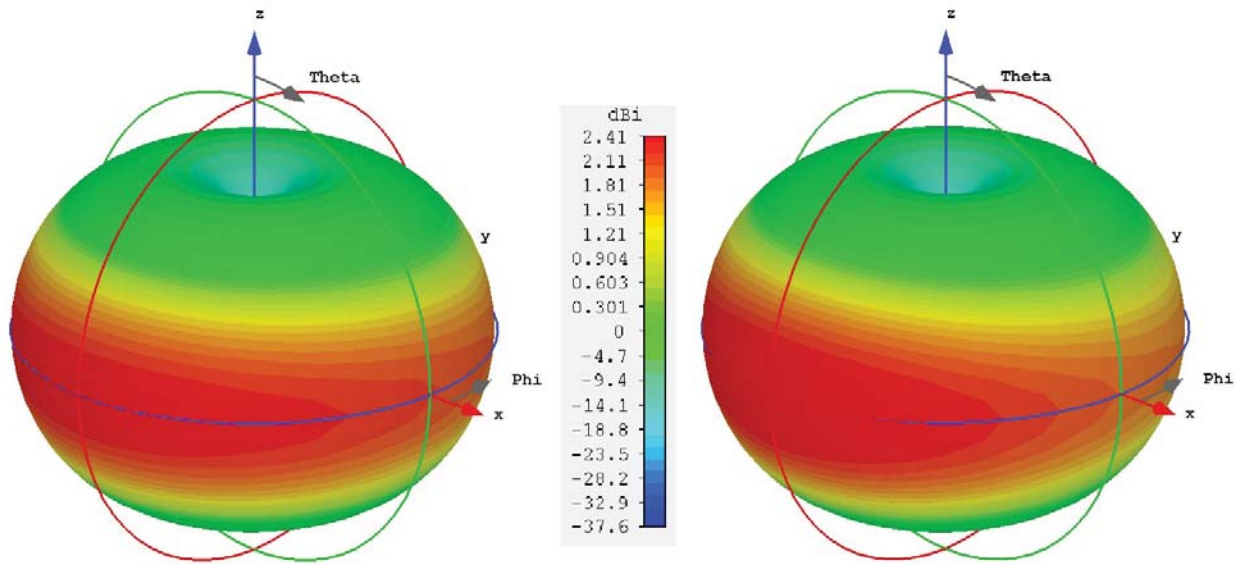

Figure 2.39. 3D radiation patterns of the uncloaked Antenna I and II when placed at a distance $d = \lambda/32.6$ ($d = 5$ μm).
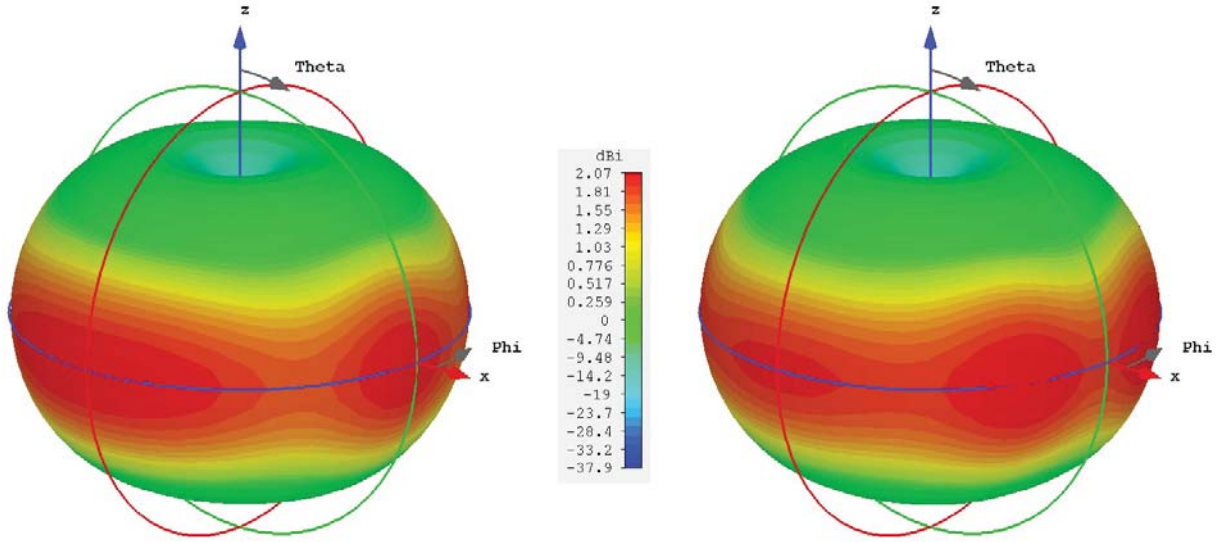

Figure 2.40. 3D radiation patterns of the cloaked Antenna I and II when placed at a distance $d = \lambda/32.6$ ($d = 5$ μm).
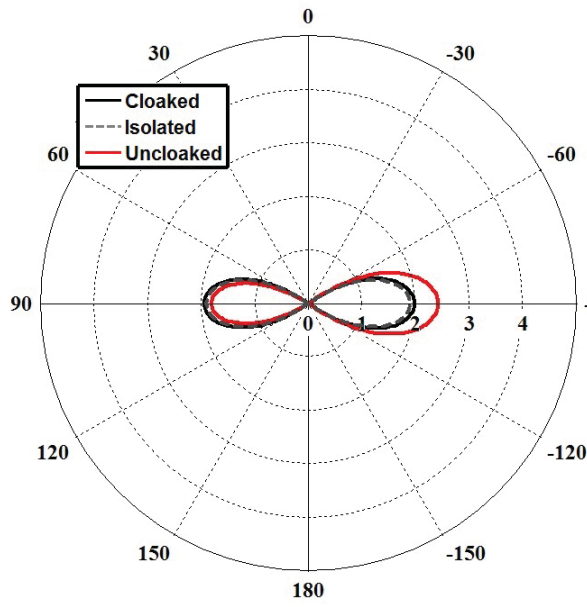
(a) E-Plane of Antenna I
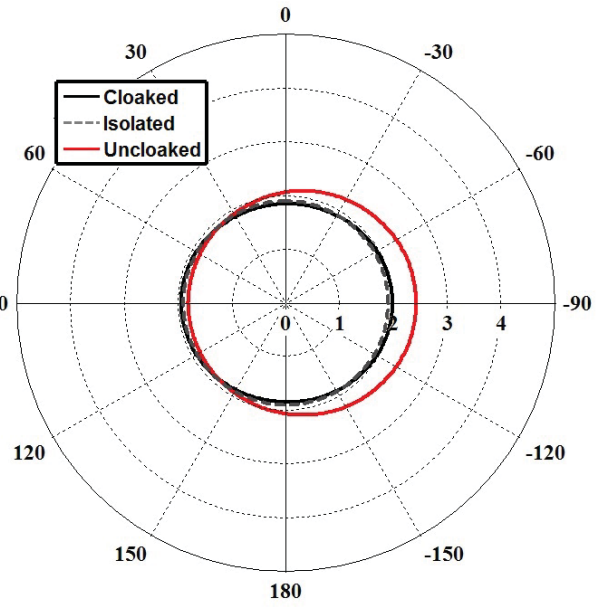
(b) H-Plane of Antenna I
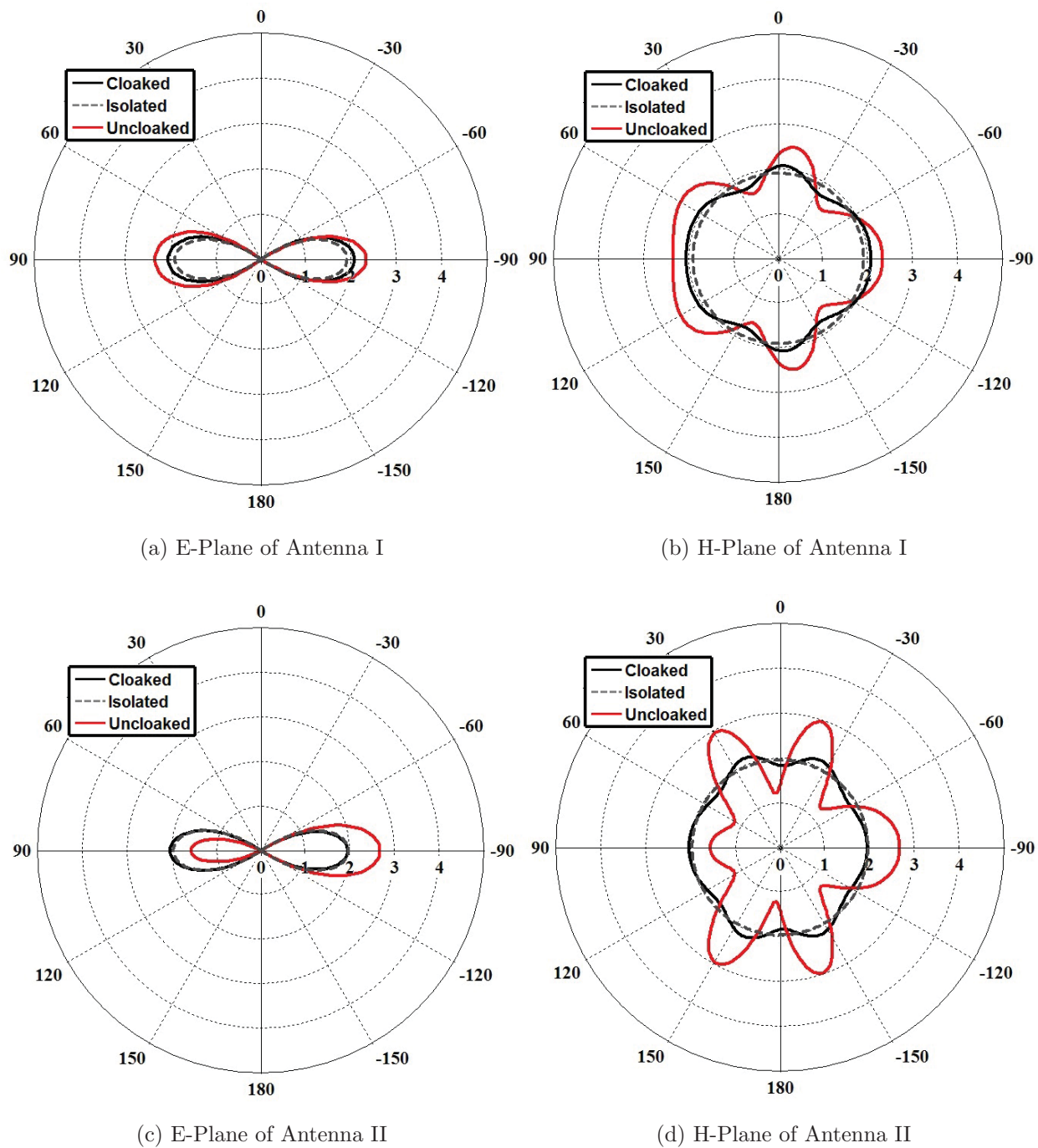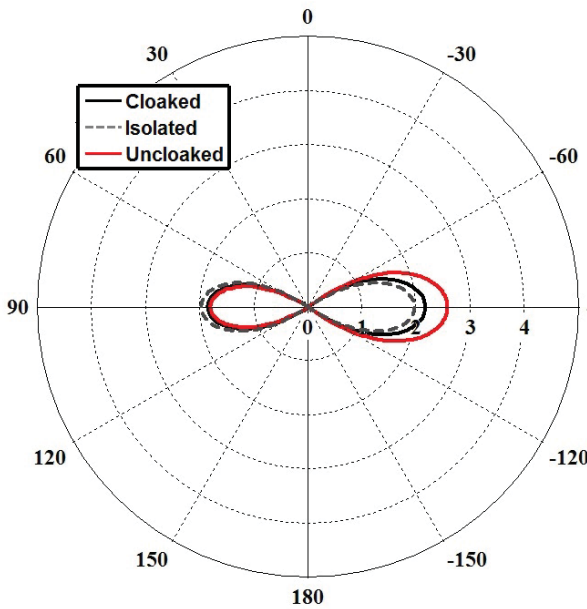
(c) E-Plane of Antenna II

(d) H-Plane of Antenna II

Figure 2.41. E and H-Plane radiation pattern for the isolated, uncloaked, and cloaked Antenna I and II in the presence of each other at $f_1 = 1.83$ THz (a,b) and for Antenna II at $f_2 = 2.31$ THz (c,d) at a distance $d/32.8 = \lambda$ ($d = 5$ μm).

2.4 Different Variables

One significant benefit of using the graphene monolayer as the cloak for the strip dipole antenna is the tunability of the graphene. This was explored mostly through the use of the chemical potential μ_c, where by changing μ_c, the antenna's resonance frequency can be changed without changing any of the geometrical properties of the antenna. To this end, it is the goal of this design process that the antennas should be able to be cloaked at any frequency within the frequency range defined by the changing of the μ_c. One such design is included in the following section, where by only changing μ_c, the resonance frequency of Antenna I and II are changed, and the antennas are still cloaked at the resonance frequency of the other antenna. It is also important to explore the importance of the losses of the graphene monolayer, represented through τ. In all the previous designs, $\tau = 1.5ps$, which is considered to be a very pristine graphene. In other research done on graphene, lower values for τ are used, so one such design using a lower τ is detailed below. In addition, the effect of τ on the antennas and the cloaking of the antennas is elaborated on.

2.4.1 Different μ_c

For this design, the μ_c of the graphene monolayer wrapped around Antenna I and II was changed to provide the cloaking effect at another set of frequencies. The geometrical properties of the antennas are unchanged for this design. This is an important benefit of using the graphene monolayer, as the only change in the antennas is the μ_c of Antenna I and II, where for Antenna I, $\mu_c = 1.0$ eV, and for Antenna II, $\mu_c = 1.0$ eV. This change in μ_c resulted in a new set of resonance frequencies, with $f_1 = 1.61$ THz, and $f_2 = 2.02$ THz.

The S-parameters of these two antennas can be seen in Fig. 2.34. The changing of μ_c has not had any significant impact on the matching characteristics of the antenna, with S_{11} = -15.1 dB at $f_1 = 1.61$ THz for Antenna I, and with $S_{11} = -29.6$ dB at $f_2 = 2.02$ THz for Antenna II. The reduction in the mutual coupling has also remained quite consistent, with
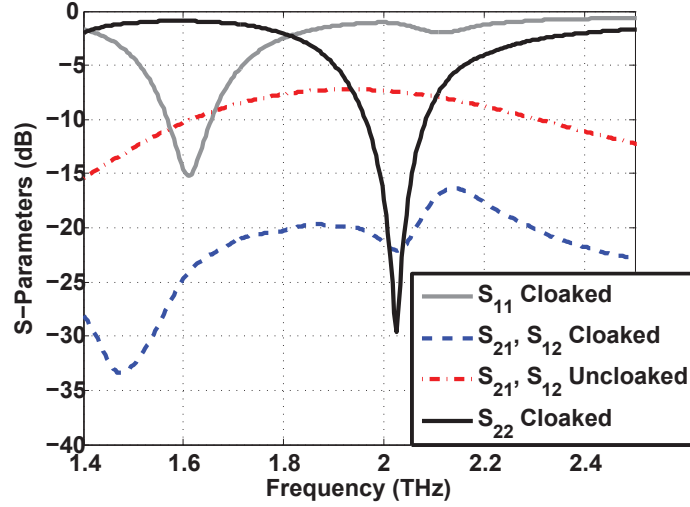
Figure 2.42. S-Parameters of the Cloaked Antenna I and II at a distance $d = \lambda/10.92$ ($d = 15~\mu$m).

the reduction being -14 dB at f_1, and a -14.6 dB reduction at f_2.
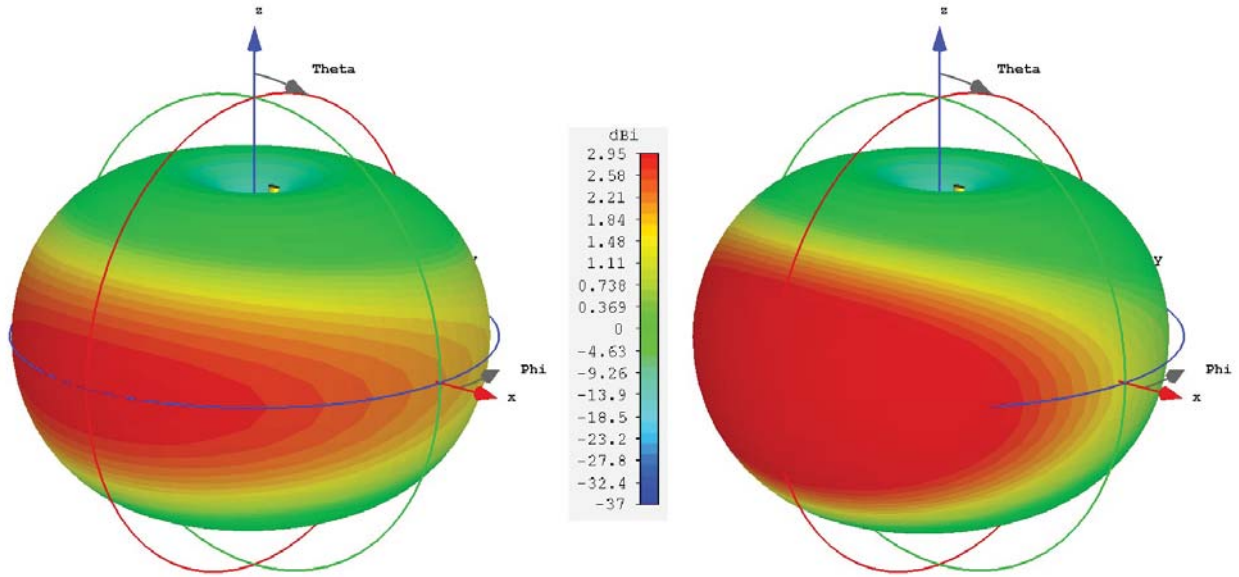
Figure 2.43. 3D radiation patterns of the uncloaked Antenna I and II when the chemical potential μ_c is changed for both antennas. $d = \lambda/10.92$ ($d = 15~\mu$m).
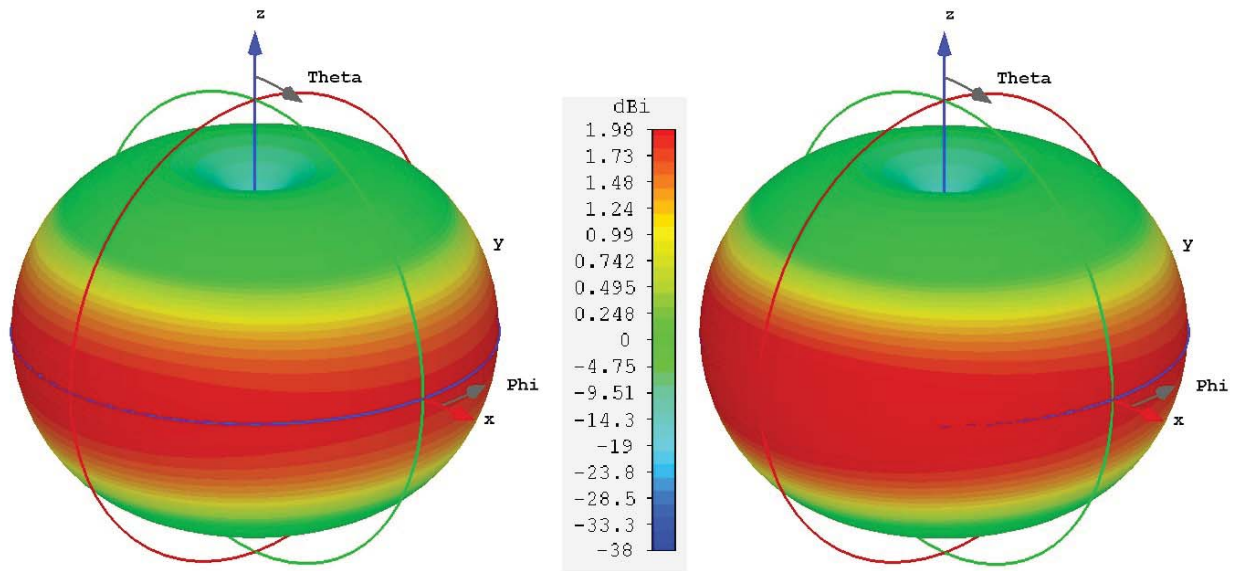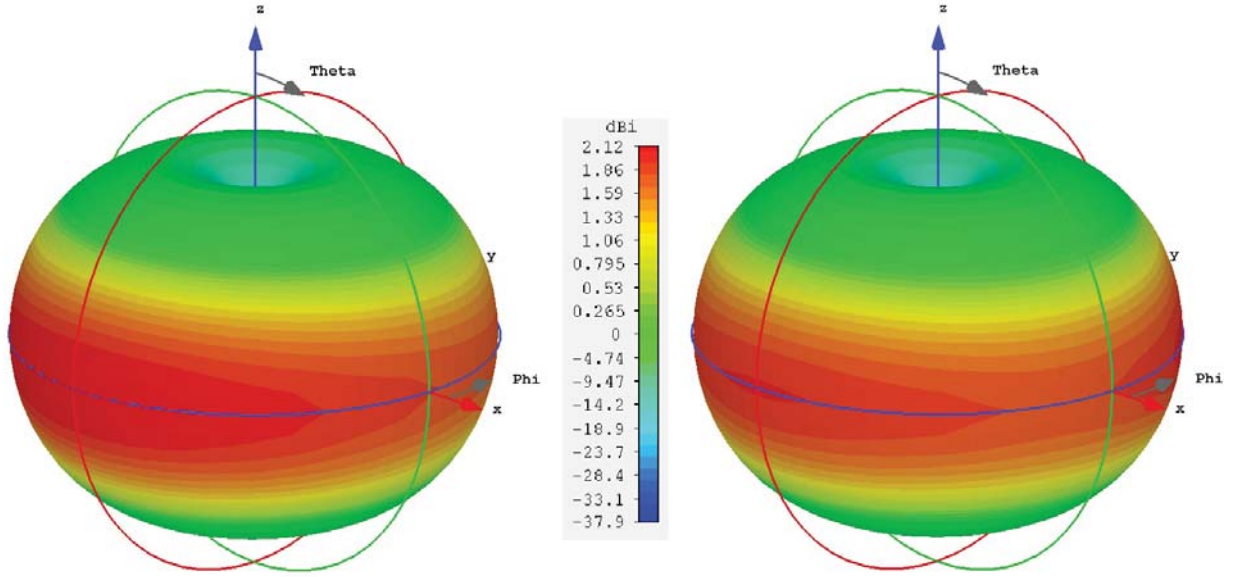
Figure 2.44. 3D radiation patterns of the cloaked Antenna I and II when placed at a distance $d = \lambda/10.92$ $(d = 15~\mu\text{m})$.
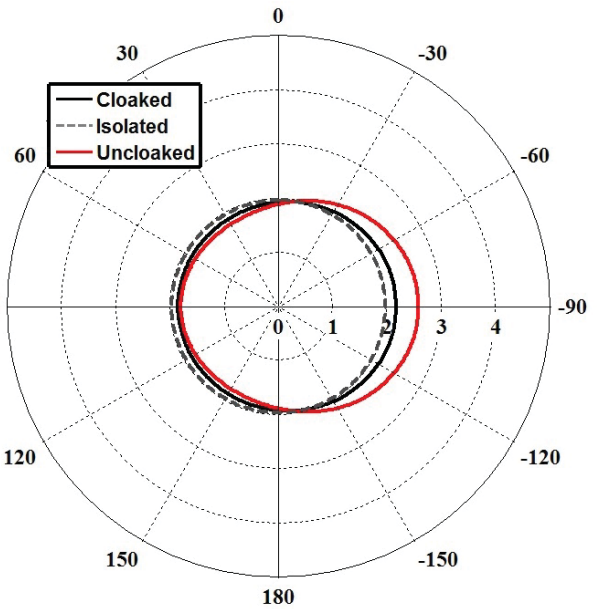
The radiation pattern of the uncloaked and antennas are shown in Figs. 2.43 and 2.44. It is interesting to note that the radiation patterns of Antenna I is very similar to the original case, regardless of the frequency shift from the change in μ_c. The E and H-plane radiation patterns are shown in Fig. 2.45, where the patterns are significantly restored as in the other cases.

It is important to note that this change in μ_c can be done for any μ_c between $\mu_c = 0.75 - 1.5$ eV. The design process could be repeated for any new resonance for Antenna I, and then based on the ACS and RCS of that Antenna I, the resonance frequency of Antenna II is chosen, and this frequency can be reached by solely changing the μ_c of Antenna II.
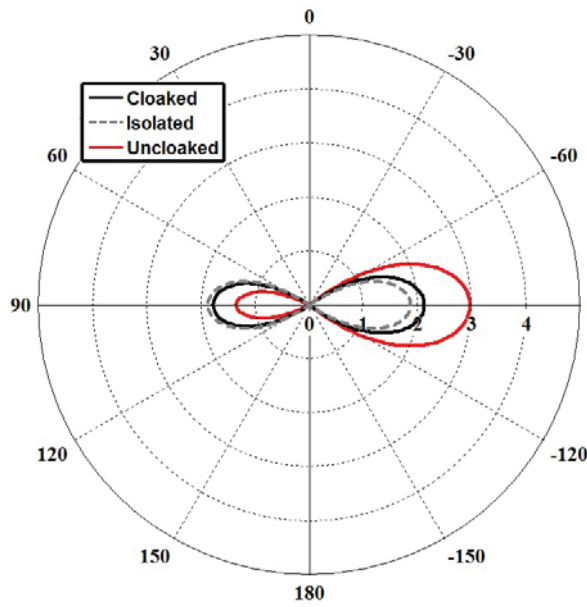
(a) E-Plane of Antenna I
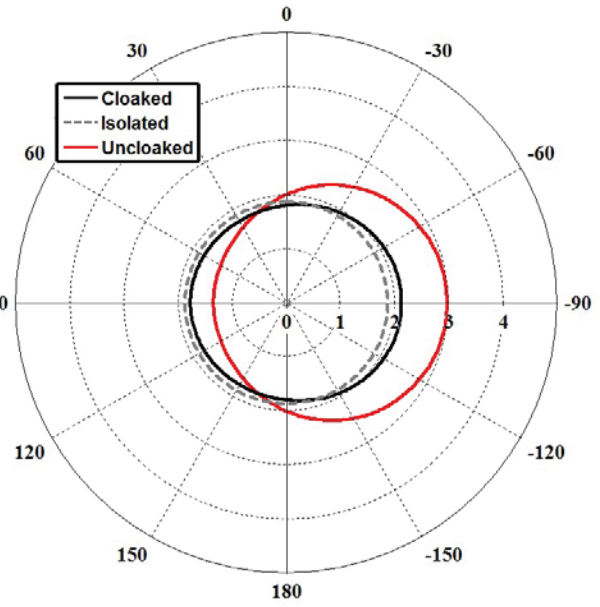
(b) H-Plane of Antenna I
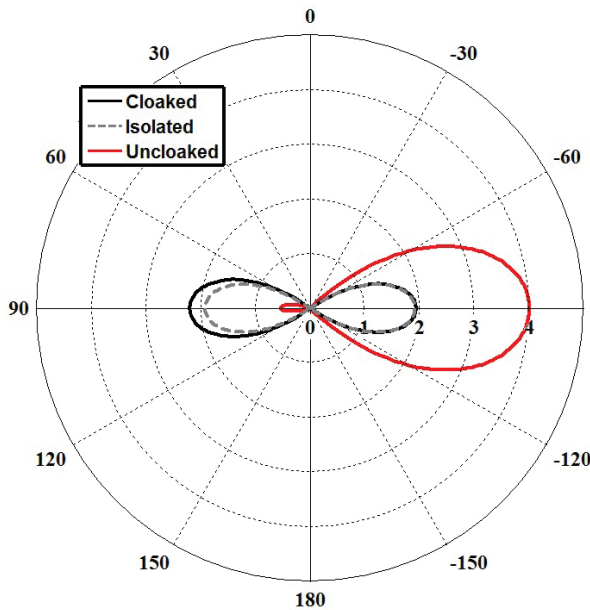
(c) E-Plane of Antenna II
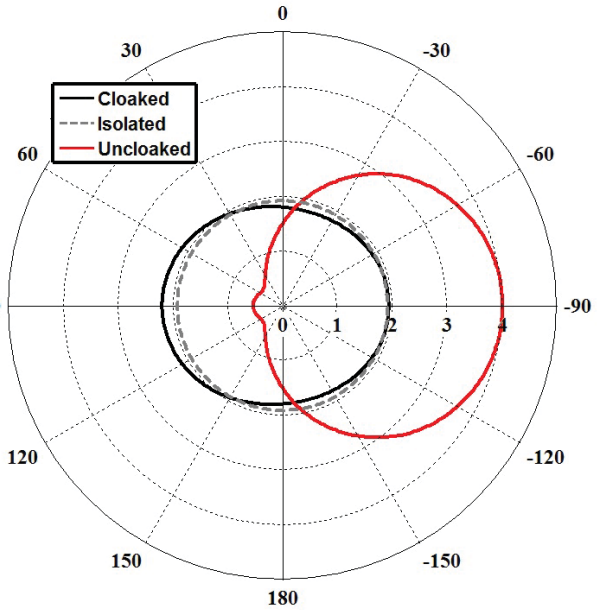
(d) H-Plane of Antenna II

Figure 2.45. E and H-Plane radiation pattern for the isolated, uncloaked, and cloaked Antenna I and II in the presence of each other at $f_1 = 1.61$ THz (a,b) and for Antenna II at $f_2 = 2.02$ THz (c,d) at a distance $d/10.92 = \lambda$ ($d = 15$ μm).

2.4.2 Momentum Relaxation Time, τ

The momentum relaxation time, τ, represents the losses in the graphene monolayer. This is reflected from the σ_{intra} contribution to the surface conductivity from Eq. (1.3). As mentioned earlier, any change in τ affects the resistance of the graphene monolayer, where a decrease in τ corresponds to a increase in the resistance. The μ_c also has an effect on the resistance, where a higher μ_c results in a lower resistance. The best case for our antennas is using a graphene monolayer with $\mu_c = 1.5$ eV and $\tau = 1.5$ ps, where an infinite graphene monolayer has a resistance of 3.77 Ω. When the resistance of the graphene monolayer is low, the combination with the strip dipole antenna causes the antenna to be well matched.

Figure 2.46. Total efficiency of Antenna I with varying momentum relaxation time $\mu_c = 0.75$ eV to 1.5 eV.

The total efficiency of an antenna is a combination of the radiation efficiency with the matching of the antenna. The efficiency of the antenna directly depends on the μ_c and τ of the graphene monolayer, which can be seen in Figs. 2.46 - 2.48. In Figs. 2.46 and 2.47, the total efficiency of Antenna I and II vs μ_c can be seen. The efficiency decreases as the μ_c decreases. It is important to note that these two antennas are the final designs from the earlier sections. As a result, Antenna I has a smaller elliptical dielectric cylinder, which affects the input resistance of the antenna, causing it to be smaller, and thus less well

49

matched. Antenna II has the best sized elliptical dielectric cylinder for the matching of the antenna, and thus has a slightly higher total efficiency. Next the efficiency of Antenna II is plotted vs. τ in Fig. 2.48. As τ decreases, the total efficiency of the antenna decreases. The minimum τ in the plot, $\tau = 0.75$ ps was chosen because the cloaking effect can still be shown when this increased τ is used.
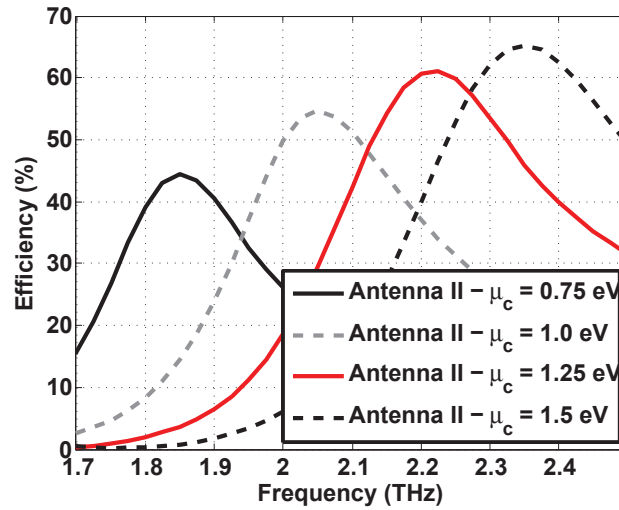
Figure 2.47. Total efficiency of Antenna II with varying momentum relaxation time $\mu_c =$ 0.75 eV to 1.5 eV.
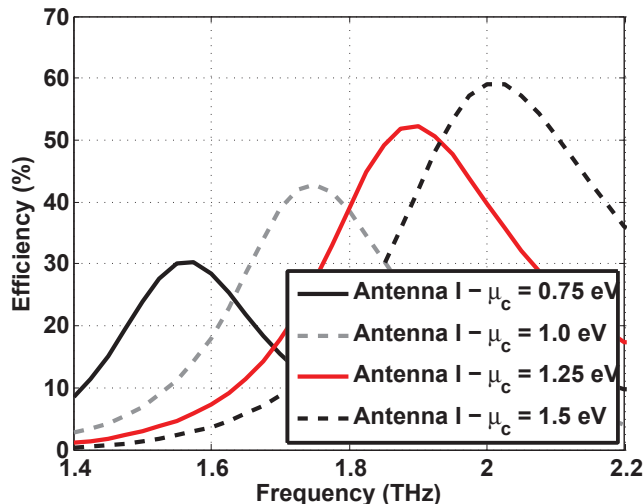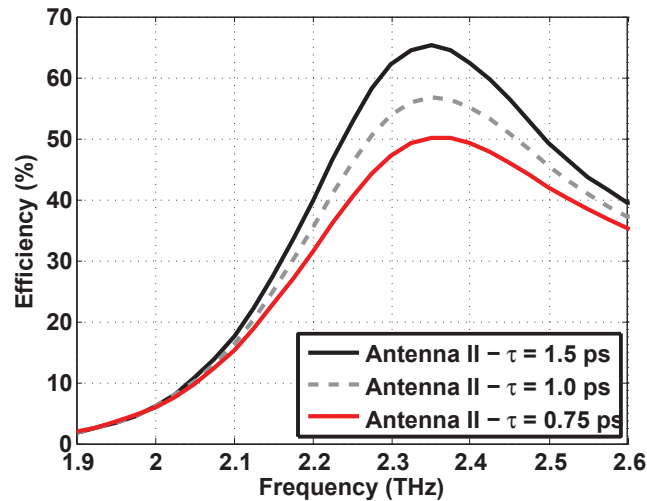

Figure 2.48. Total efficiency of Antenna II with varying momentum relaxation time $\tau. =$ 0.75 ps to 1.5 ps.

The S-parameters for this design with $\tau = 0.75$ ps are shown below in Fig. 2.49. Other than this change of τ, this design is identical to the final design discussed earlier. This is an important to show, as the sole change of the τ does not cause any frequency shift in the resonance frequency in the antennas. It is interesting to note that the increased resistance of the graphene monolayer has caused a significant improvement in the S_{11}, from $S_{11} = $ -13.9 dB when $\tau = 1.5$ ps, to $S_{11} = $ -39.7 dB when $\tau = 0.75$ ps. This is due to the fact that for Antenna I when $\tau = 1.5$ ps, the smaller size of the elliptical dielectric cylinder resulted in a lower than desired input resistance in Antenna I, with $R_{input} = 55$ Ω, instead of the desired $R_{input} = 75$ Ω. This desired resistance of 75 Ω was achieved in the final design for Antenna II due to a larger elliptical dielectric cylinder, and as a result, the increased resistance of the graphene monolayer caused an increase in the S_{22}, from $S_{22} = $ -28.5 dB when $\tau = 1.5$ ps, to $S_{22} = $ -16.8 dB when $\tau = 0.75$ ps.
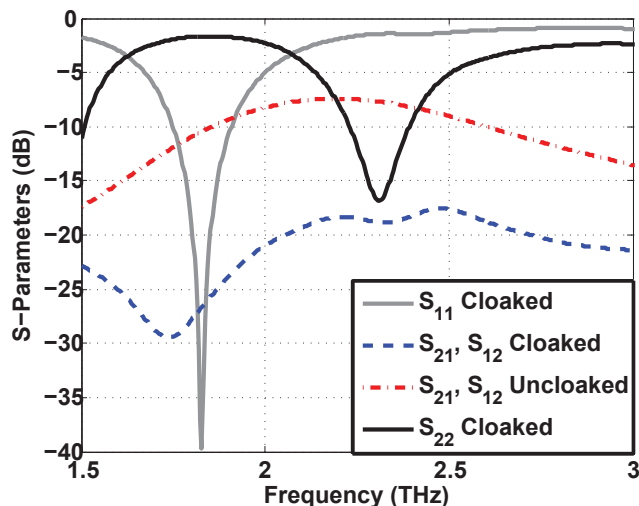
Figure 2.49. S-Parameters of the Cloaked Antenna I and II with $\tau = 0.75$ps at a distance $d = \lambda/10.92$ ($d = 15$ μm).

The radiation patterns for this lower τ case can be seen in Figs. 2.50 - 2.52. The patterns from the uncloaked Antenna I and II are the same as the closely spaced antennas from earlier, since the changing of τ has no effect on the uncloaked antennas. The radiation patterns of the cloaked antennas have not been very affected by the change in τ, as can be

51

seen in Fig. 2.51 and 2.52.
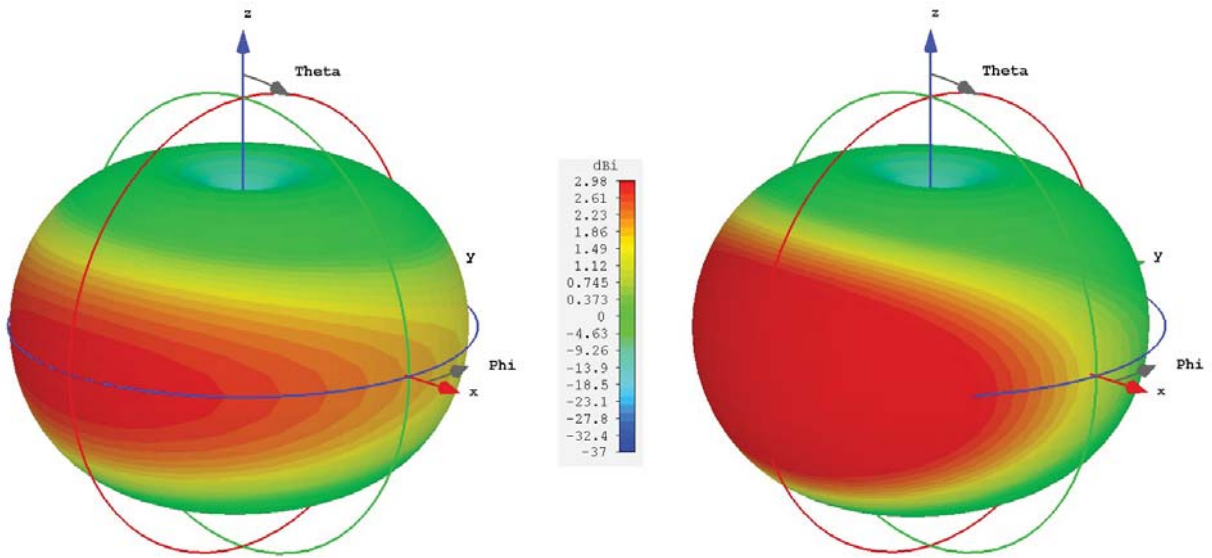
Figure 2.50. 3D radiation patterns of the uncloaked Antenna I and II when placed at a distance $d = \lambda/10.92$ ($d = 15$ μm).
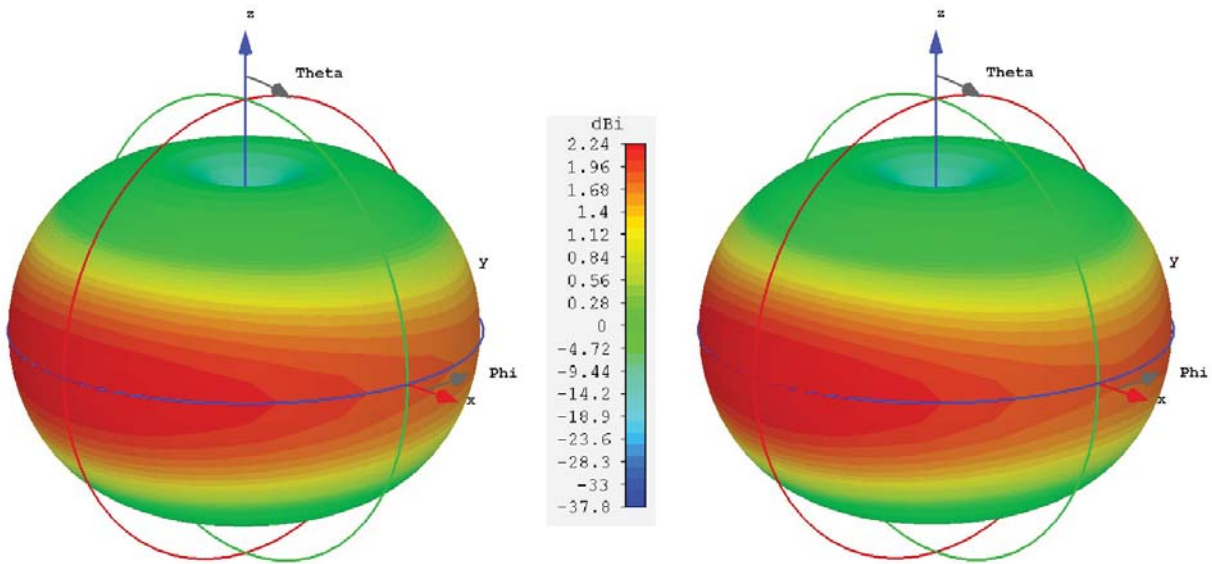
Figure 2.51. 3D radiation patterns of the cloaked Antenna I and II with $\tau = 0.75$ps when placed at a distance $d = \lambda/10.92$ ($d = 15$ μm).

(a) E-Plane of Antenna I

(b) H-Plane of Antenna I

(c) E-Plane of Antenna II

(d) H-Plane of Antenna II
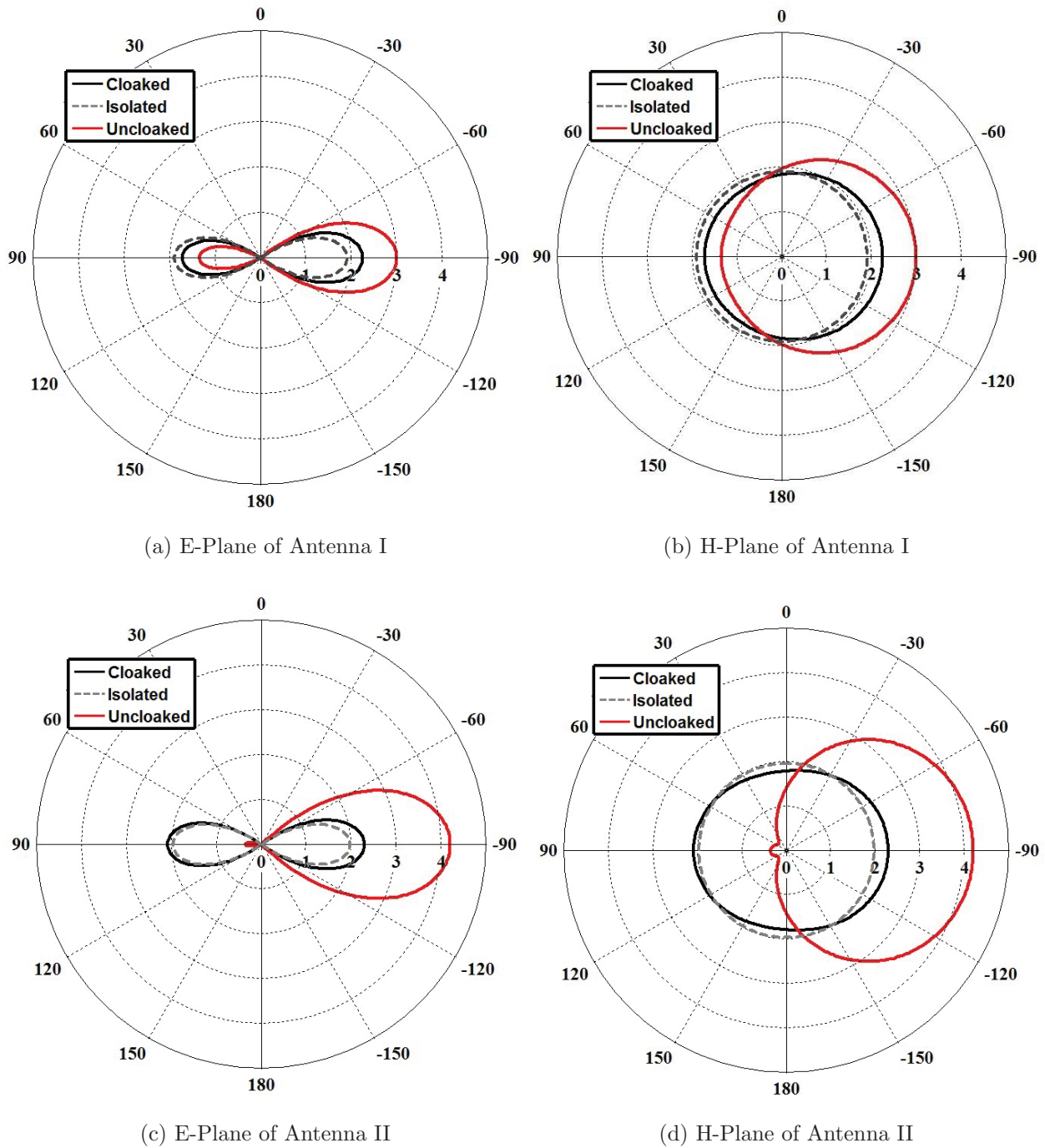
Figure 2.52. E and H-Plane Radiation Pattern for the Cloaked Antenna I in the presence of the Cloaked Antenna II with $\tau = 0.75$ps at $f_1 = 1.828$ THz (a,b) and for Antenna II at $f_2 = 2.275$ THz (c,d) at a distance $d = \lambda/10.92$ ($d = 15$ μm).

This behavior will continue as τ is decreased further, with the input resistance of the antennas increasing. However, below this example at $\tau = 0.75$ ps, the cloaking structure

breaks down. First, the reduction in the mutual coupling becomes less pronounced. In the previous designs, the mutual coupling has a dip at a frequency very close to the resonance frequencies of the antennas. It is also important to note that the efficiency of Antenna I at a lower τ becomes a significant concern, at $\tau = 0.5$ ps, Antenna I has a total efficiency of only 23%. This low efficiency was frequently a concern when designing these antennas, as the antennas without any graphene monolayer cloak are very efficient, usually up to 90%.

The cloaking structure can be viewed in a different way which can shed some light on the efficacy of the cloaking. In Fig. 2.53, the maximum directivity of the 3D radiation pattern is shown for multiple cases. The cases are for the isolated, uncloaked, and cloaked Antenna II for different τ, with $\tau = 0.25$, 0.5, 0.75, and 1.5 ps. This plot indicates how directive
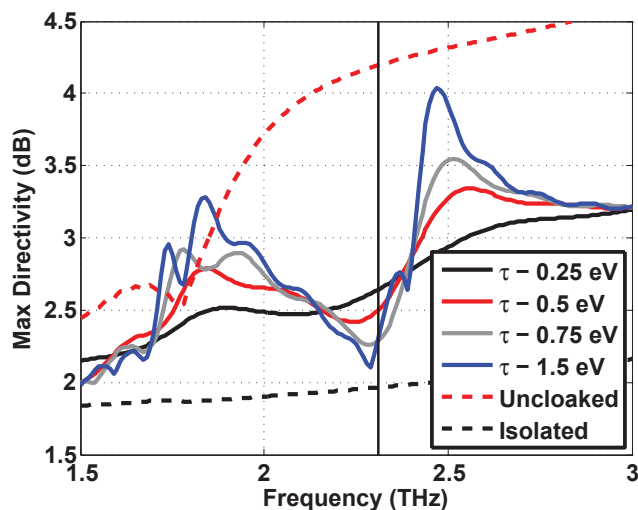
Figure 2.53. Maximum directivity for the isolated, uncloaked, and cloaked Antenna II for varying momentum relaxation time $\tau = 0.25$ - 1.5 ps.

Antenna II's radiation pattern is vs frequency. The frequency of interest is indicated by the vertical black line at $f_2 = 2.31$ THz. This is most clearly indicated by the difference between the isolated (black dashed line) and the uncloaked (red dash line). The cloaked radiation patterns are indicated by the solid lines, with descending τ. The antenna being cloaked is clearly indicated by the $\tau = 0.75$ and 1.5 ps curves. These curves indicate a clear reduction in the directivity of the radiation pattern at the frequency of interest. For lower τ, this reduction

becomes less significant, until at $\tau = 0.5$ ps, where there is significantly less reduction. It is important to note that these cloaked radiation patterns are still significantly less directive than the uncloaked case. To reinforce what this plot represents, the 3D radiation plots of 4 of the cases from 2.53 are shown in Fig. 2.54.

(a) Isolated Antenna II

(b) Cloaked Antenna II with $\tau = 1.5$ ps

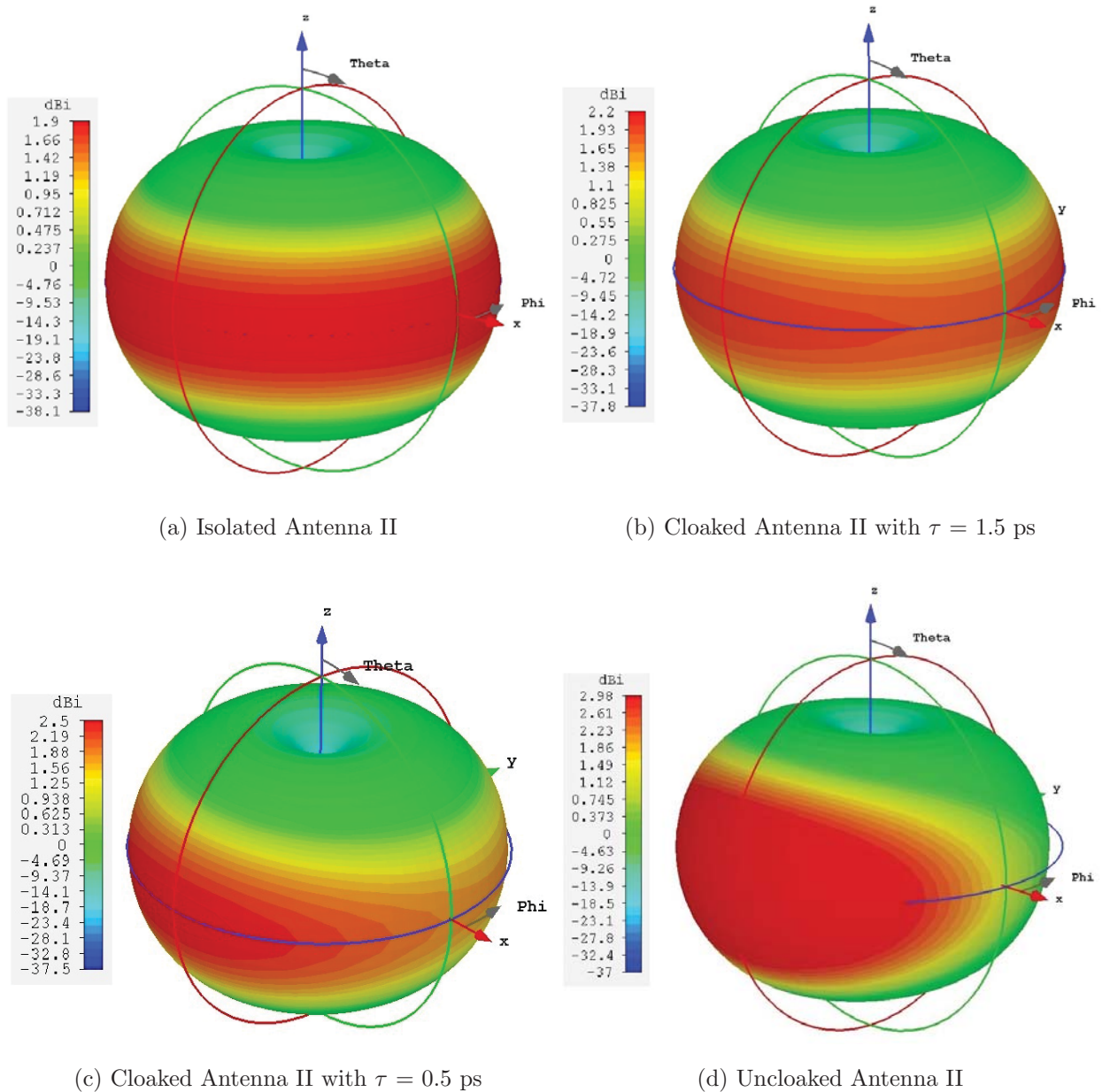(c) Cloaked Antenna II with $\tau = 0.5$ ps

(d) Uncloaked Antenna II

Figure 2.54. Maximum directivity for the isolated, uncloaked, and cloaked Antenna II for different τ ($\tau = 0.5$ and 1.5 ps).

2.5 Future Work

While the study done in this chapter was rather extensive, there are still numerous opportunities for further research which will be briefly outlined in this section. The use of the graphene monolayer for the cloak has a significant impact on the overall performance of the antenna. This is due to the surface impedance of the graphene monolayer wrapped around the elliptically shaped dielectric cylinder. The current work being done about the surface impedance of graphene has focused on the surface impedance of an infinitely sized graphene monolayer. As a result, further research must be done into how accurate this model is for less than infinitely large graphene sheets. Additionally, there are opportunities to improve the practicality of these structures by using more realistic feeding for the antennas at THz frequencies, where the graphene can still be used as a metasurface for cloaking. In regards to the use of cloaking for antennas, there are numerous opportunities for continued research, such as the use of cloaks for MIMO systems and phased arrays. For both of these applications, the important result that still remains to be seen is an antenna which resonates and is cloaked at the same frequency. This in particular is a long term goal that could open up many different opportunities.

2.6 Conclusion

Throughout this section, the use of a graphene monolayer was explored for the use of cloaking strip dipole antennas at THz frequencies. The cloaking effect has resulted in a significant reduction in the mutual coupling between closely spaced antennas and the restoration of radiation patterns. This is an interesting opportunity for taking advantage of the tunability of graphene, as due to its tunable nature as a metasurface, the resonance frequency of the cloaked antenna can be shifted through the chemical potential. This tunability also plays an important role in the cloaking of the antenna, as when the resonance

frequency of the antenna changes, so does the frequency at which the antenna is cloaked. There are further opportunities to continue the study of this type of cloaked antenna, in particular with regards to the input impedance of these antennas, as there is still much to be understood about how the graphene impacts the input impedance of the antenna.

CHAPTER 3

WIDEBAND MONOPOLE ANTENNAS

3.1 Cylindrical Wideband Antennas

The bandwidth of antennas has always been a significant area of interest throughout antenna design. In Chapter 1, a paper was mentioned by Jiang et. al. [57]. In this paper, a wideband monopole antenna was designed and fabricated in the low GHz frequency range. This antenna represents an interesting opportunity in antennas, as this antenna uses two metasurfaces made up of the same pattern to acheive this drastically improved bandwidth. In this chapter, the following will be discussed: a replication of the results from this paper, the transition from the cylindrical antenna structure to an elliptical one, and then the transition from the elliptical structure to a microstrip antenna.

3.1.1 Original Monopole Antenna

The antenna in [57] provided a significant increase in the bandwidth a wire monopole antenna. The concept of using a metasurface to improve some part of the performance is something very similar to the previous section about cloaking antennas. However, the structure of the antenna and metasurface was significantly different and should be explained further. The geometry of this antenna can be seen in 3.1.

The antenna is a simple copper wire monopole antenna set on top of a ground plane, fed by an SMA type port. The monopole has radius $r_{mono} = 0.5$ mm and length $L = 28.5$ mm. The metasurface is made up of two identical metasurfaces of different sizes, with radii

58
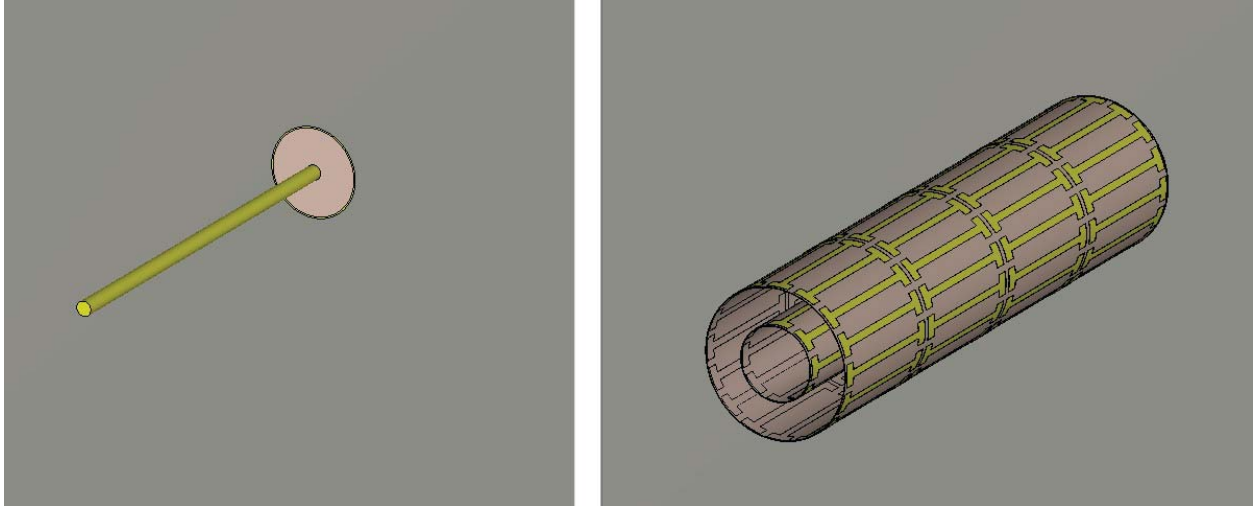
Figure 3.1. Geometry of the Cylindrical wideband antenna without and with the metasurface.

$r_{metasurface1} = 2.5$ mm and $r_{metasurface2} = 5$ mm and with length $H_l = 40$ mm. It is important to note that the metasurfaces are longer than the length of the antenna, which is consistent throughout all of the following designs. The metasurfaces themselves are comprised of unit cells of I-shaped metal patterns, which are printed on a thin dielectric cylinder. The dielectric is quite thin, with a thickness $t_{diel} = 0.051$ mm and with a dielectric constant $\epsilon_r = 2.9$. There is only air between the antenna and the metasurface layers. The geometry of the unit cell

Figure 3.2. Cross sectional view of the cylindrical wideband antenna and the metasurface unit cell.

and a cross section of the cylindrical wideband monopole antenna can be seen in Fig. 3.2. The unit cell has a width of $W = 2$ mm and a length of $B = 10$ mm. The I-shaped pattern has the following parameter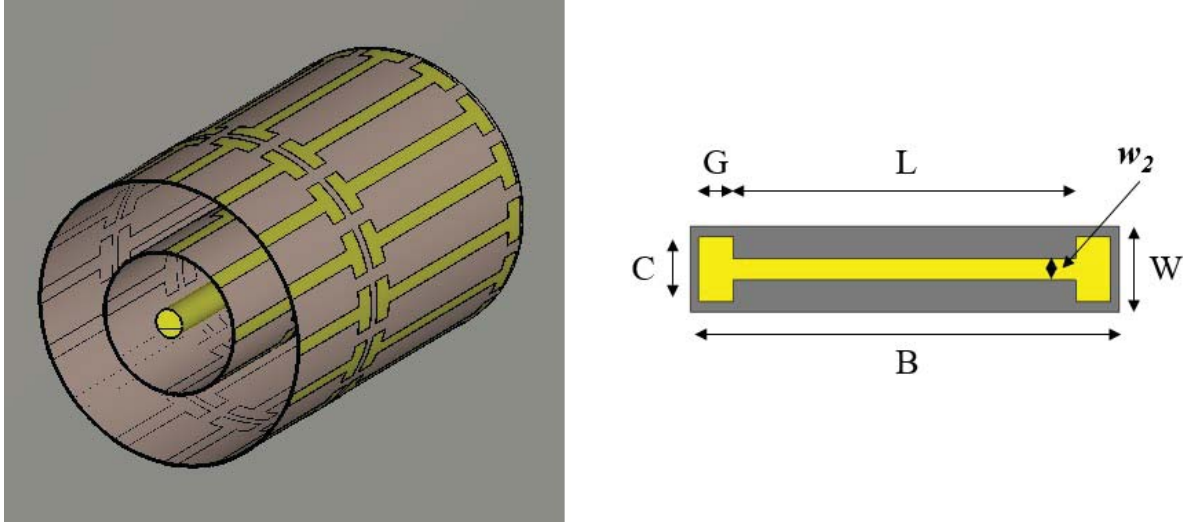s: $L = 8$ mm, $C = 1.5$ mm, $G = 0.8$ mm, $w_2 = 0.5$ mm, $t = 0.017$ mm, and with a $gap = 0.4$ mm between the I-shaped patterns. The inner layer is 8 unit cells wrapped around the dielectric, while the outer layer contains 16 unit cells.

With this knowledge, the structure was recreated in CST Microwave studio. It is important to note that the size of the port used in the paper was not explicit, so there is some small deviation between the paper results and the results that were recalculated. One such difference in the results is that the original dipole had a -10 dB bandwidth of 2.1 - 4.4 GHz, while the remade monopole antenna had a -10 dB bandwidth of 2.3 - 4.54 GHz. The S_{11} of this remade monopole antenna versus the original monopole without the metasurface can be seen in Fig. 3.3.
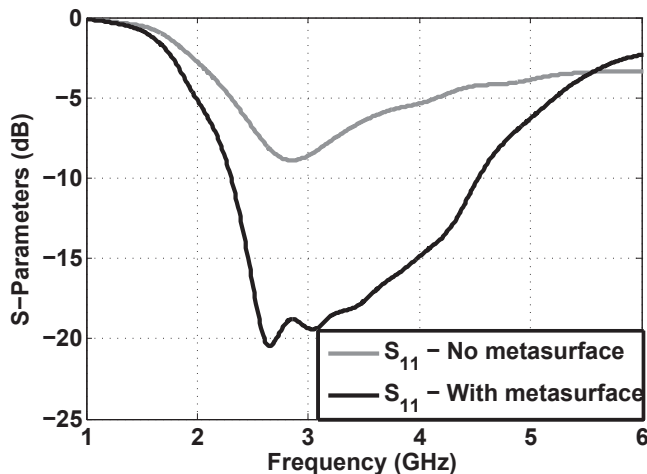
Figure 3.3. S-Parameters of the Wideband Monopole Antenna.

The key to the vastly improved bandwidth of these monopole antennas with the metasurfaces stems from the impedance bandwidth, both for the real and imaginary part of the input impedance. The input resistance and reactance can be seen in Fig. 3.4 and 3.5. Throughout the increased bandwidth, there is a significant flattening of the input impedance when compared with the same monopole antenna with no metasurface. This is a consistent
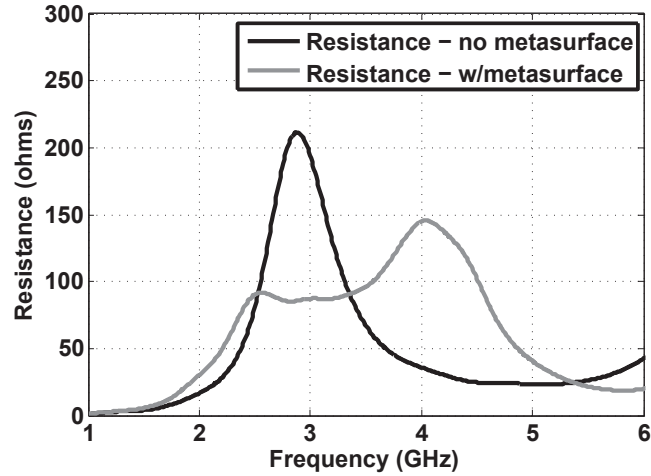
Figure 3.4. Input resistance of the first, lower frequency, Wideband Monopole Antenna.

pattern with this antenna design, throughout the frequency range of interest. This can also be seen in the radiation patterns of the antenna throughout the same frequency range.
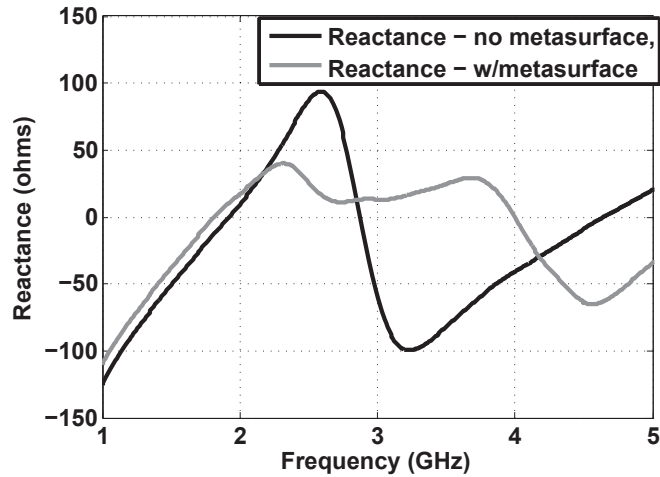
Figure 3.5. Input reactance of the first, lower frequency, Wideband Monopole Antenna.

The radiation patterns of the antenna can be seen in 3.6. The radiation patterns are remarkably consistent throughout the entire frequency band. This indicates that the antenna will be very useful for wideband applications, as the antenna behavior is very consistent throughout this large bandwidth.
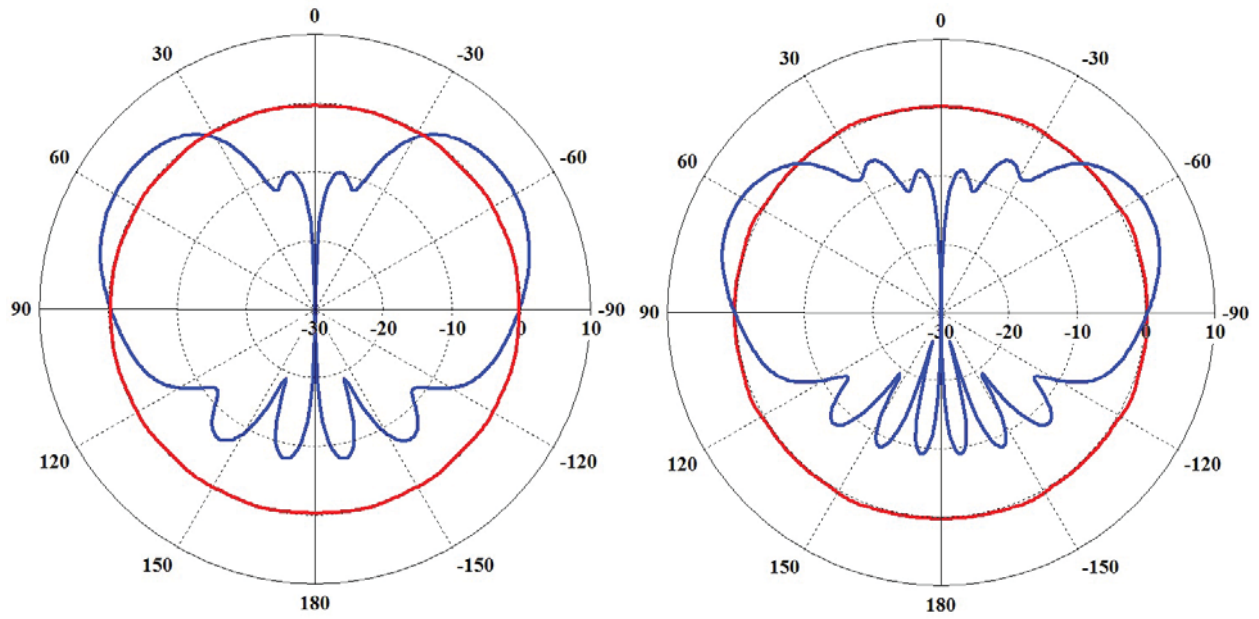
(a) E and H-Plane radiation patterns at 2.4 GHz

(b) E and H-Plane radiation patterns at 3.4 GHz
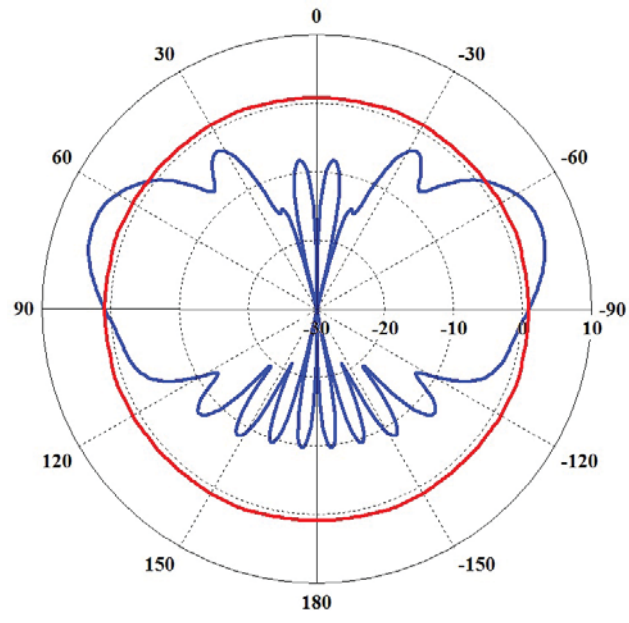
(c) E and H-Plane radiation patterns at 4.4 GHz

Figure 3.6. E (blue) and H-plane (red) radiation patterns for the original lower frequency cylindrical wideband monopole antenna, at different frequencies within the -10 dB bandwidth (2.3 - 4.54 GHz).

3.1.2 Higher Frequency Monopole Antenna

Now that this antenna has been recreated, new antennas can be made using this base design. First, a higher frequency of this antenna was created, with the goal of a similarly
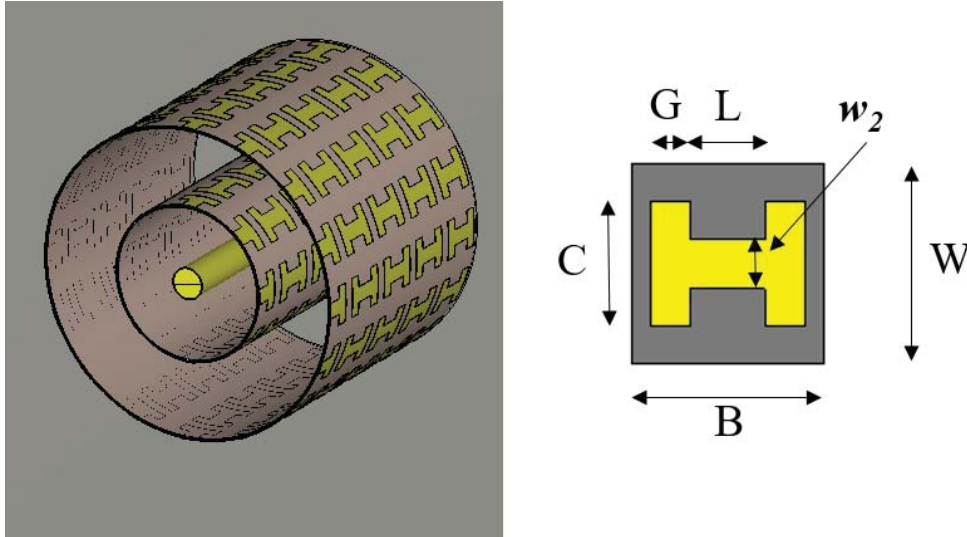
Figure 3.7. Cross sectional view of the cylindrical wideband antenna and the metasurface unit cell.

large increase in the bandwidth of the antenna. Both the antenna size and the metasurface parameters had to be changed to achieve this shift in frequency.
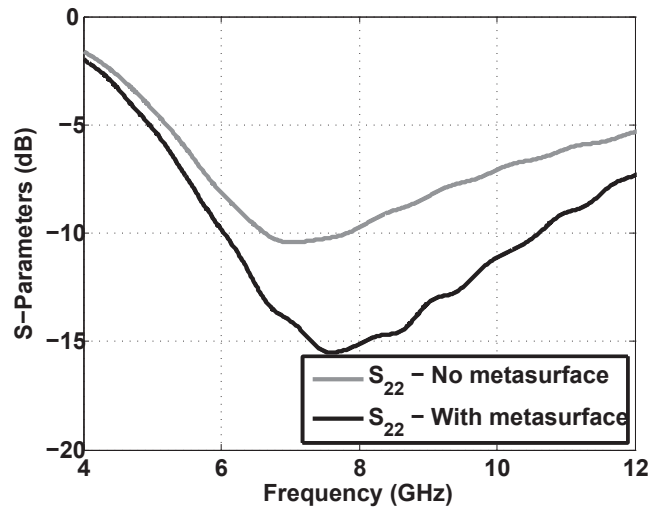
Figure 3.8. S-Parameters of the wideband monopole antenna, operating at a higher frequency.
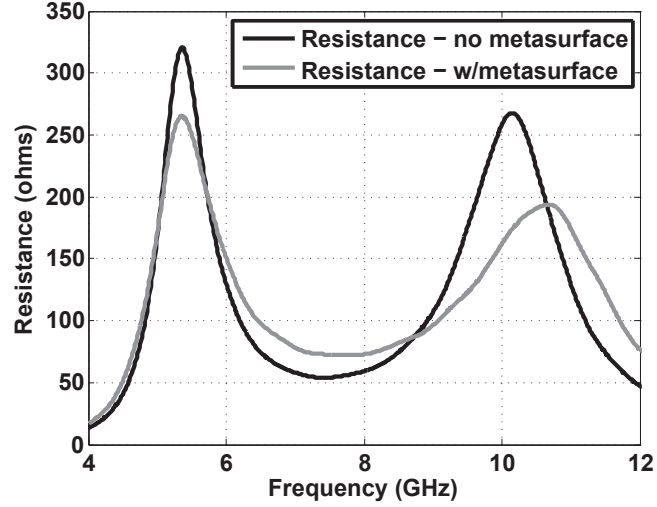
Figure 3.9. Real input impedance of the second, higher frequency, Wideband Monopole Antenna.
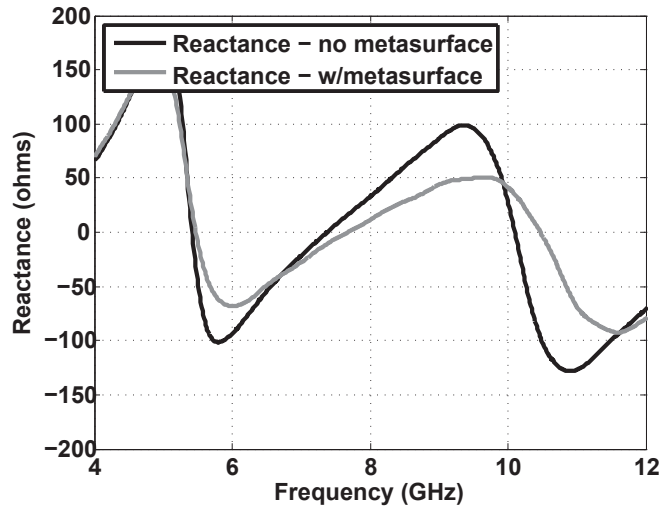
Figure 3.10. Imaginary input impedance of the second, higher frequency, Wideband Monopole Antenna.

The wire monopole was shortened to $L = 10$ mm, the dielectric was shortened to H_l = 19.5 mm, and the following parameters were also changed: $L = 0.75$ mm, $G = 0.4$ mm, and $C = 1.25$ mm, which can be seen in Fig. 3.7. All of these changes facilitate the increased bandwidth at a higher frequency. The S_{22} of this higher frequency antenna can be seen in Fig. 3.8, where the antenna has a -10 dB bandwidth of 3.9 GHz, from 6.04 - 10.59 GHz.
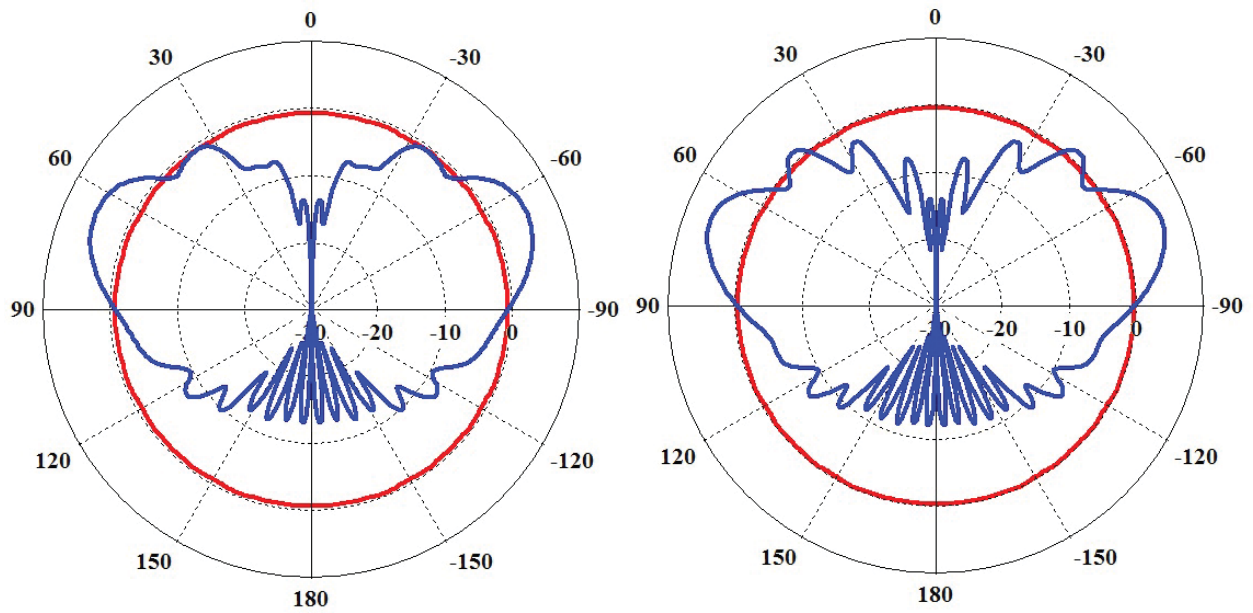
(a) E and H-Plane radiation patterns at 6.25 GHz

(b) E and H-Plane radiation patterns at 7.5 GHz
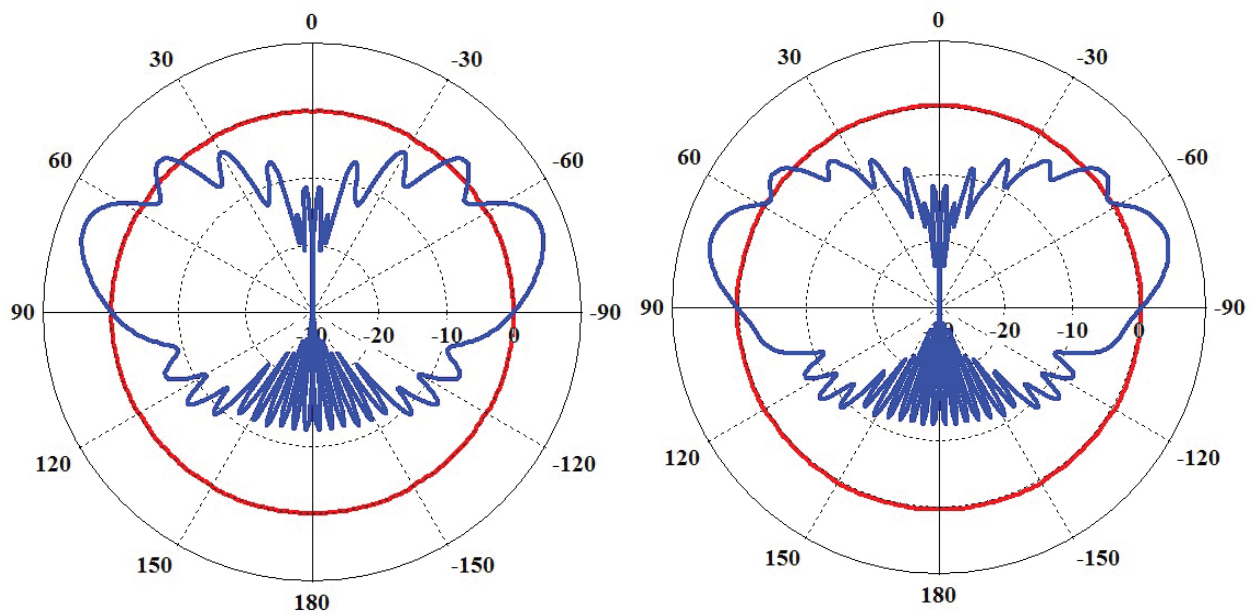
(c) E and H-Plane radiation patterns at 8.75 GHz

(d) E and H-Plane radiation patterns at 10 GHz

Figure 3.11. E (blue) and H-plane (red) radiation patterns for the higher frequency cylindrical wideband monopole antenna, at different frequencies within the -10 dB bandwidth (6.04 - 10.59 GHz).

This is also a significant improvement in bandwidth over the normal monopole antenna resonating at these frequencies. This was an important first step, to verify that the

behavior could be achieved with other designs. Additionally, the behavior of the input resistance and reactance is also similar to the original design, with a flattening of the input impedance in the frequency range of interest.

The radiation patterns of the antenna can be seen in Fig. 3.11. There is a remarkably similar pattern throughout the frequency band of operation. It is also worth noting that the patterns for this antenna are even more consistent than for the previous antenna, which is likely due to the size of the ground plane in relation to the wavelengths in this frequency band. The ground plane is 320 x 320 mm for all of these designs.

3.1.3 Coupled Cylindrical Antennas

Now that these two antennas have been modeled, they can be placed together to see how much the two antennas interfere with each other. The two antennas are placed together on the same ground plane at distances $d = 44$ and 88 mm. The geometries for these two distances can be seen in 3.12 and 3.14
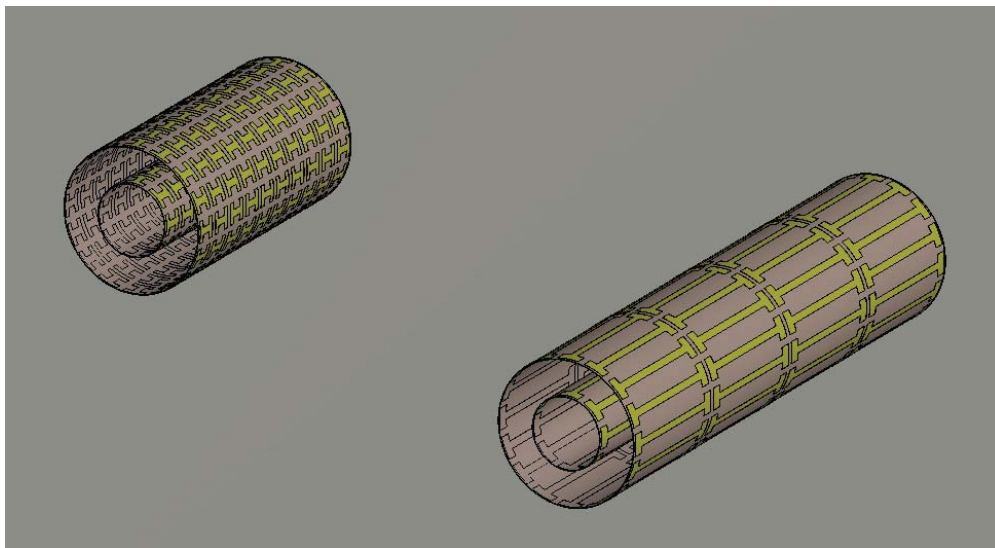
Figure 3.12. Geometry of the Cylindrical wideband antennas when placed at a distance $d = 44$ mm.

This distance d is measured from the center of the first antenna to the center of

the second antenna. The S-parameters for these two antenna spacings are shown in Figs. 3.13 and 3.15. The S-parameters are remarkably consistent even when the antennas are
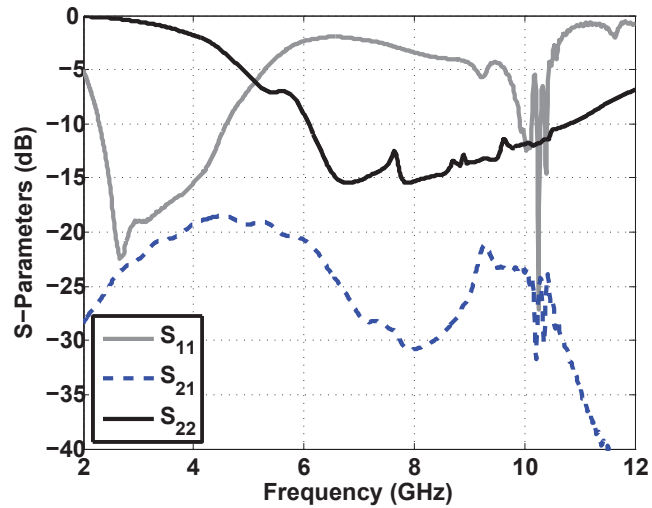
Figure 3.13. S-Parameters of the two cylindrical coupled wideband antennas, at a distance $d = 44$ mm.

placed together on a single ground plane. The bandwidth of the antennas has also not been significantly affected by the introduction of the antennas to each other. The mutual coupling between the two antennas is directly affected by the spacing of the antennas, as in the frequency range of both monopoles, the S_{21} is about -5 dB higher for the closer spacing, $d = 44$ mm.

Figure 3.14. Geometry of the Cylindrical wideband antennas when placed at a distance $d = 88$ mm.
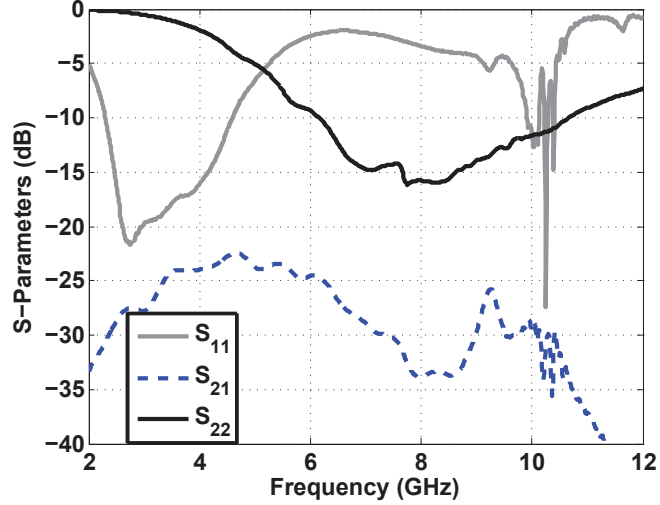
67

Figure 3.15. S-Parameters of the two cylindrical coupled wideband antennas, at a distance $d = 88$ mm.

It is also interesting to note that the radiation patterns of the two antennas are not significantly affected by the two antennas being placed close together. This can be seen in Figs. 3.16 - 3.19, which show the E and H-Plane radiation patterns at different frequencies for the isolated (blue), antennas spaced at $d = 44$ mm (red), and antennas spaced at $d = 88$ mm (black). In particular, the lower frequency antenna is almost entirely unaffected by the introduction of the higher frequency monopole antenna. This is likely due to the larger difference in the frequency range of the antennas, where in [52], when two strip dipole antennas were placed together at significantly different frequencies, 1 and 5 GHz, the smaller antenna did not require a cloak, as the antenna did not represent a significant object to the lower frequency antenna.

However, the second antenna's H-plane patterns indicate a more significant disturbance of the higher frequency antenna's radiation patterns throughout the frequency range of interest. These distortions are not so significant that the antenna could not still be used, but further investigation is needed into the possibility of restoring this antenna to its original radiation patterns in the presence of the longer, lower frequency monopole antenna.

It should also be noted that while not included here, the matching characteristics and
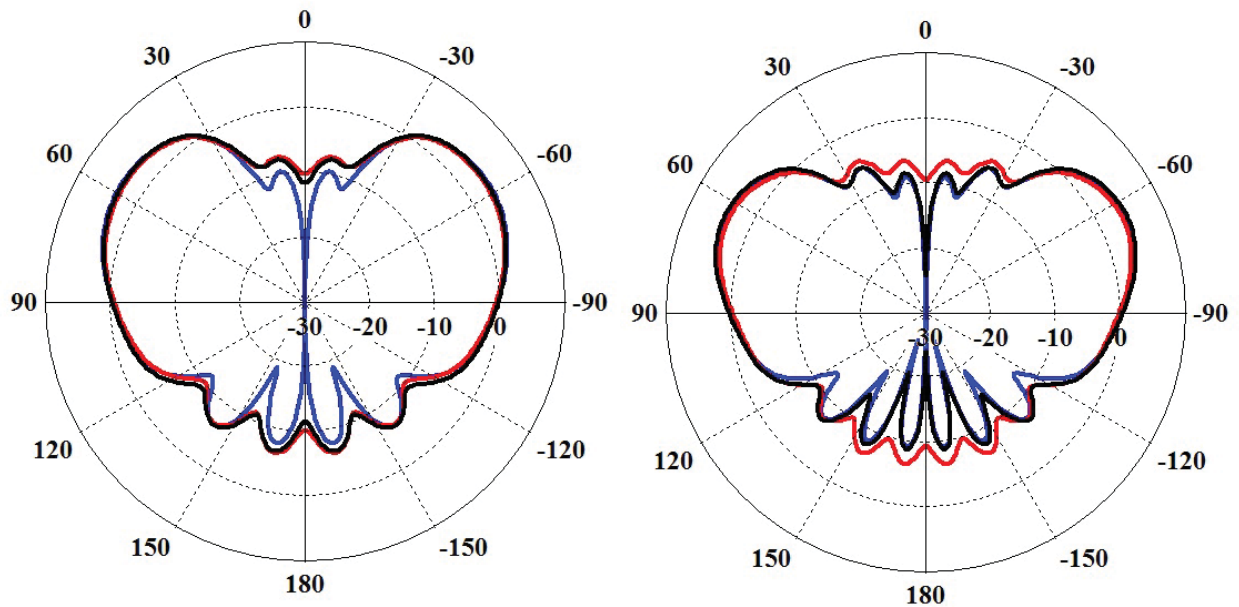
(a) E-Plane radiation patterns at 2.4 GHz

(b) E-Plane radiation patterns at 3.4 GHz
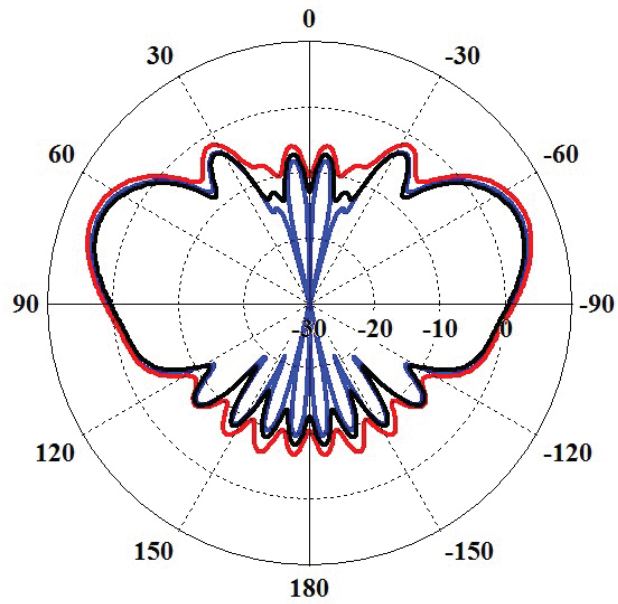
(c) E-Plane radiation patterns at 4.4 GHz

Figure 3.16. E-Plane radiation patterns for the lower frequency wideband monopole antenna, for the isolated (blue) and two different coupled cases ($d = 44$ mm (red) and $d = 88$ mm (black)).

(a) H-Plane radiation patterns at 2.4 GHz

(b) H-Plane radiation patterns at 3.4 GHz

(c) H-Plane radiation patterns at 4.4 GHz

Figure 3.17. H-Plane radiation patterns for the lower frequency wideband monopole antenna, for the isolated (blue) and two different coupled cases ($d = 44$ mm (red) and $d = 88$ mm (black)).
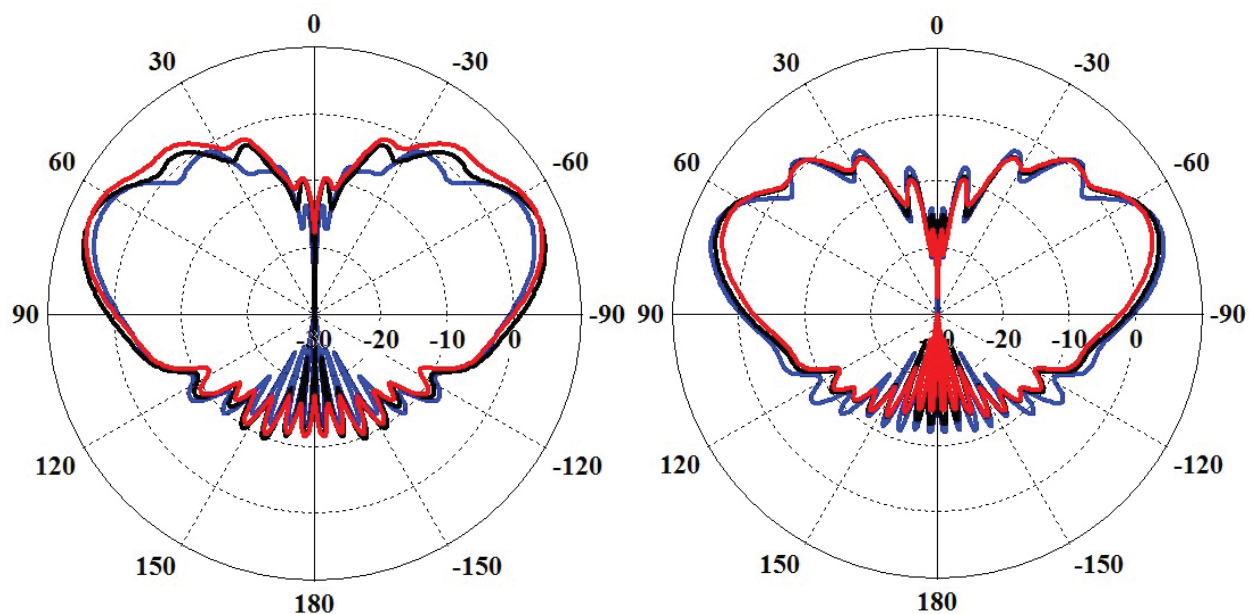
(a) E-Plane radiation patterns at 6.25 GHz

(b) E-Plane radiation patterns at 7.5 GHz
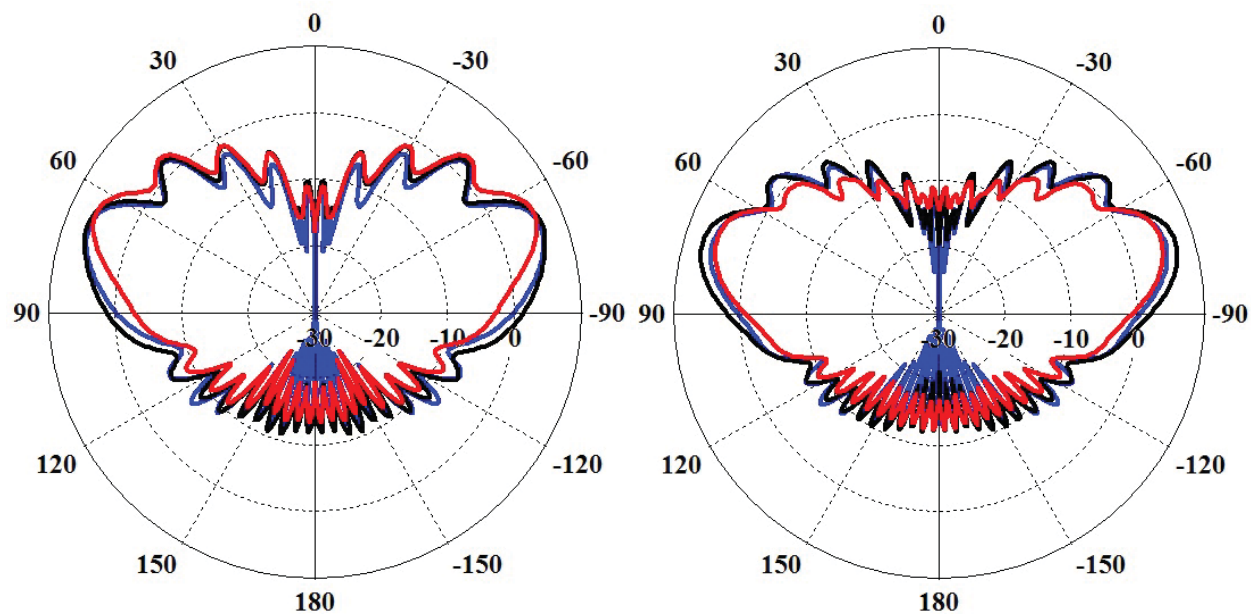
(c) E-Plane radiation patterns at 8.75 GHz

(d) E-Plane radiation patterns at 10 GHz

Figure 3.18. E-Plane radiation patterns for the higher frequency wideband monopole antenna, for the isolated (blue) and two different coupled cases ($d = 44$ mm (red) and $d = 88$ mm (black)).
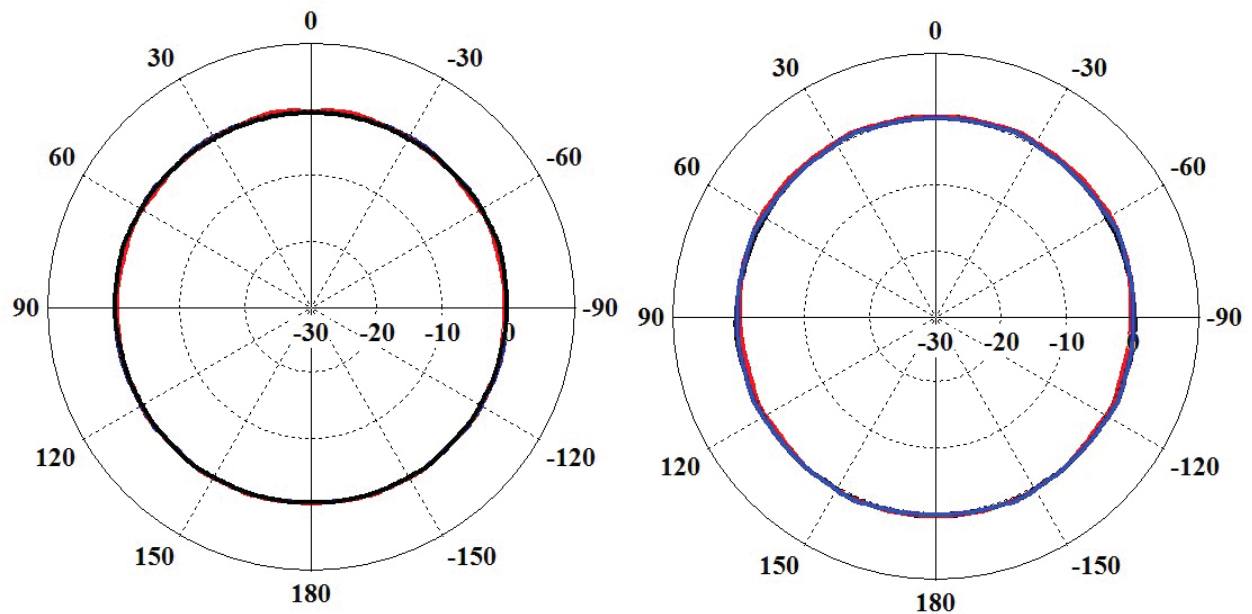
(a) H-Plane radiation patterns at 5.7 GHz

(b) H-Plane radiation patterns at 6.7 GHz
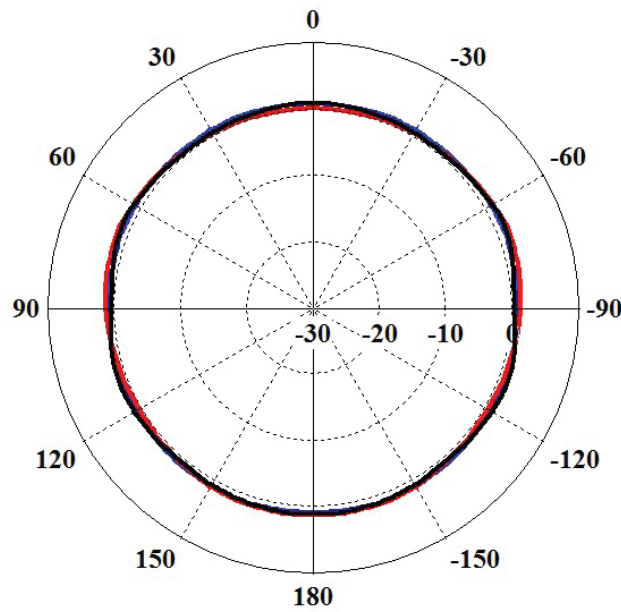
(c) H-Plane radiation patterns at 7.7 GHz

(d) H-Plane radiation patterns at 7.7 GHz

Figure 3.19. H-Plane radiation patterns for the higher frequency wideband monopole antenna, for the isolated (blue) and two different coupled cases ($d = 44$ mm (red) and $d = 88$ mm (black)).
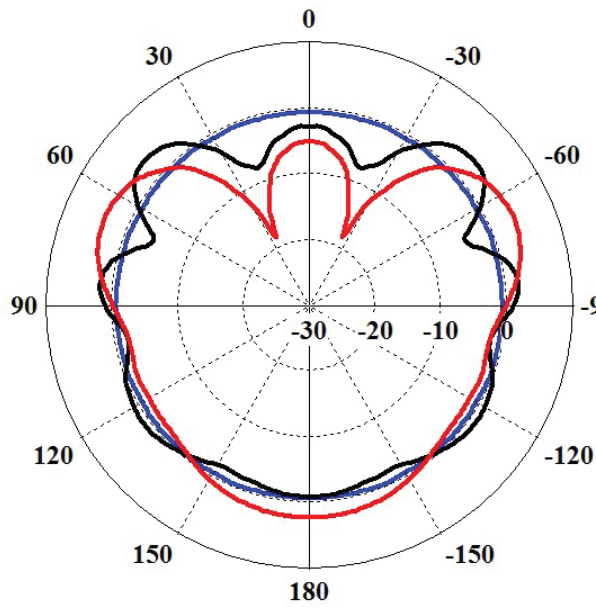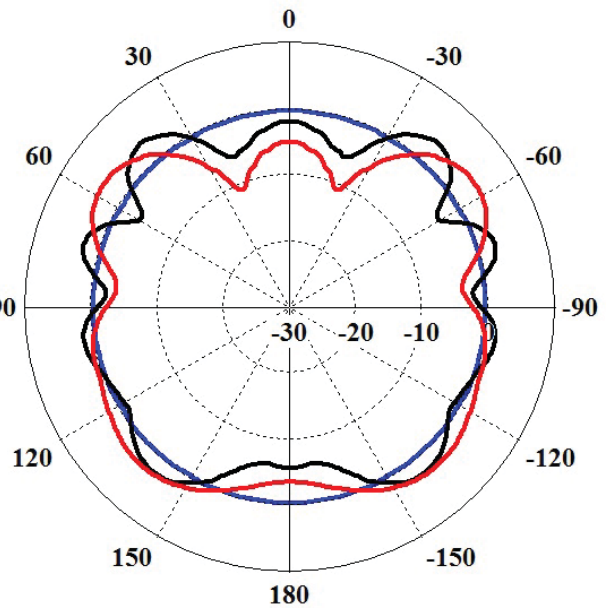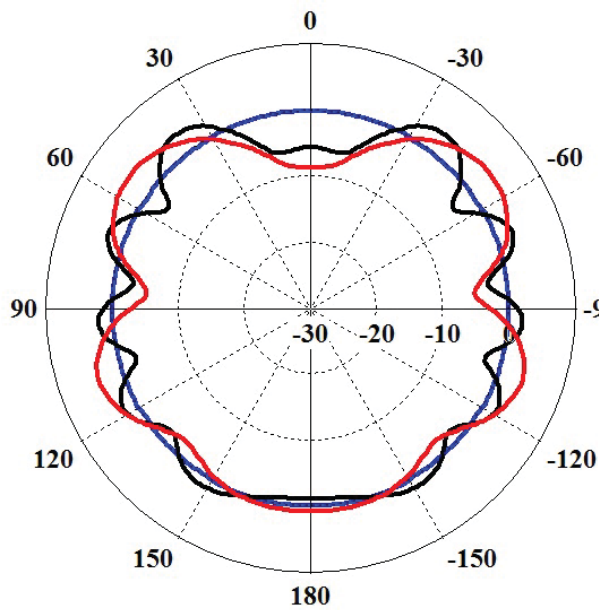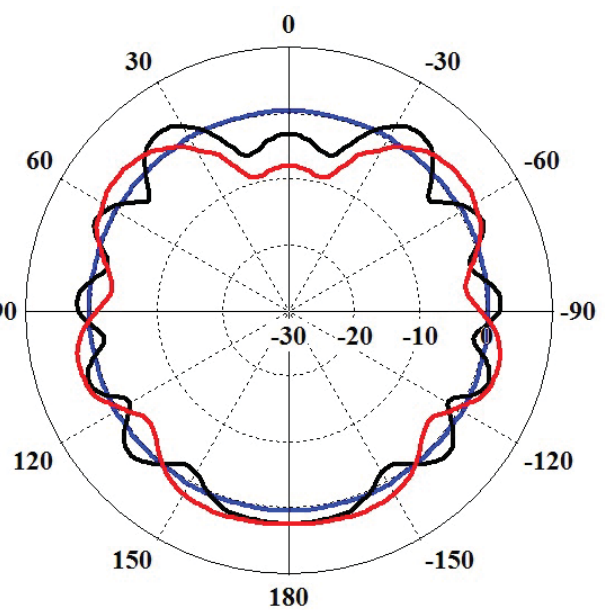
the radiation patterns when the two antennas are brought much closer together ($d = 8$ mm) are much more significantly disturbed, to the point that the -10 dB bandwidth of the higher frequency antenna becomes significantly smaller or even completely lost. This is a problem which must also be addressed, either through the adjustment of the metasurface properties, or perhaps through an attempt to cloak these antennas from each other, as mentioned in previous sections.

3.2   Elliptical Wideband Monopole Antenna

Given the extremely increased bandwidth of this monopole antenna, further study was required. To this end, the next step in the process was creating this antenna using elliptically shaped dielectric cylinders instead of the previous cylindrical shell dielectric. The first main concern when trying to achieve this transition is the fact that the previous design had significant air gaps between the antenna and between the inner metasurface and the outer metasurface. As a result of this factors, a smaller dielectric constant was chosen, $\epsilon_r = 2$. The wire dipole antenna was transformed to a strip dipole antenna, the size of the strip dipole antenna can be defined by the equation $r = \frac{1}{4}(w + t)$, which when using a very small wire dipole, with $r = 0.5$ mm, a width of $w = 2$ mm is used for a very thin ($t = 0$) strip dipole antenna.

Next, the size of the dielectric must be chosen. In previous work with elliptical metasurfaces, the focal points of the elliptical dielectric cylinder must be at the edges of the strip dipole antenna, which has $w = 2$ mm and $l = 8$ mm. It is also important that the first layer not be too large, to this end, an ellipse of size $a = 1.1$ mm and $b = 0.45$ mm was chosen for the first layer, with length $H_l = 20$ mm. The I-shaped patterns were placed on this elliptical cylinder, with 3 unit cells. Next a second dielectric cylinder was placed around this first layer, with a larger cross section with size $a = 1.6$ mm and $b = 1.24$ mm. The same I-shaped patterns were placed on this outer layer with 5 unit cells. The unit cells for the

initial design were the same size as the original design, with the following parameters: $L = 3$ mm, $C = 1.5$ mm, $G = 0.8$ mm, $t = 0.017$ mm, and with a $gap = 0.4$ mm between the I-shaped patterns. The geometry of the antenna with and without the elliptical metasurface can be seen in Fig. 3.20 and the cross sectional view can be seen with the unit cell geometry in 3.21.
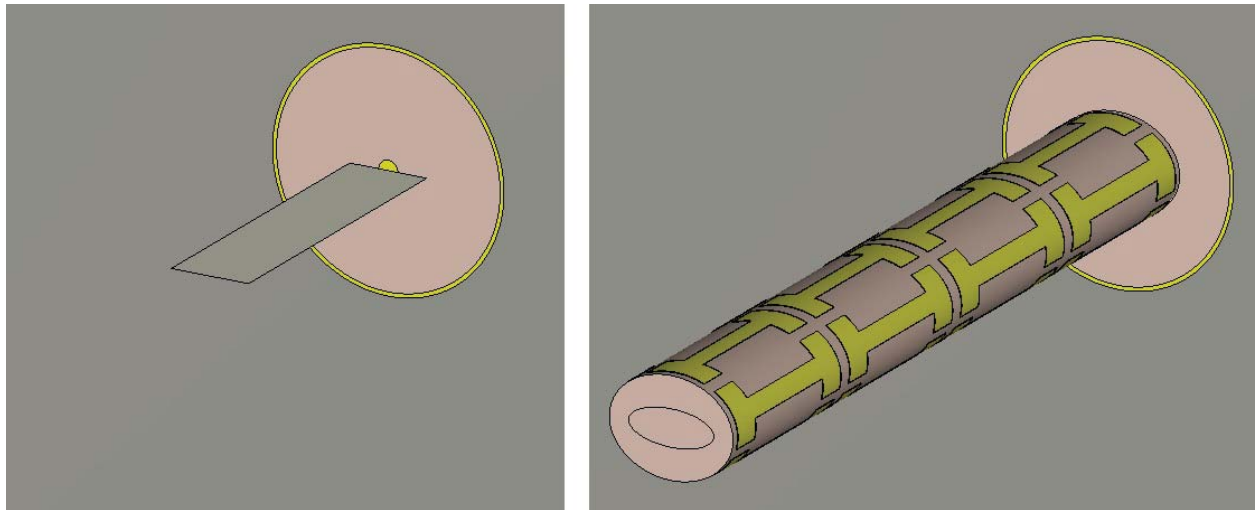

Figure 3.20. Geometry of the Elliptical wideband antenna without and with the metasurface.
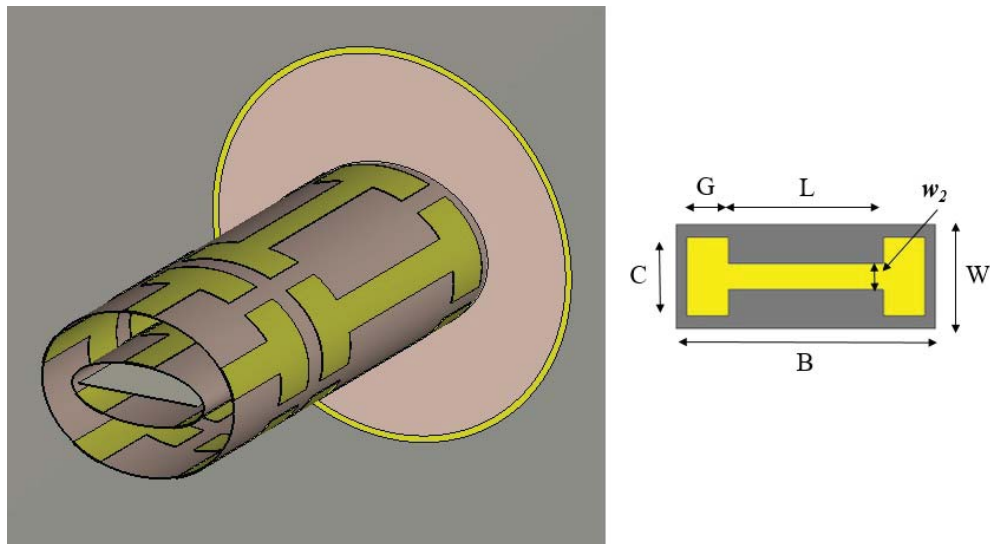
Figure 3.21. Cross sectional view of the elliptical wideband antenna and the metasurface unit cell.

The S-parameters of this antenna are shown in Fig. 3.22. This antenna has a similar
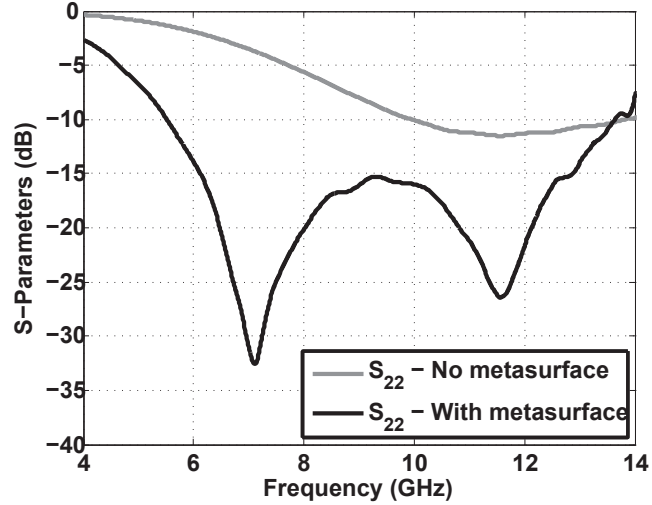
Figure 3.22. S-Parameters of the wideband monopole elliptical antenna, operating at a higher frequency.

bandwidth as the previous higher frequency antenna, with a -10 dB bandwidth from 5.51 to 13.63 GHz. There is some reduction in the bandwidth when compared to the higher frequency cylindrical monopole antenna. Some of this is due to the dielectric constant of the elliptical antenna, as the cylindrical monopole antenna had extensive air gaps between the two metasurface layers. Previous attempts at creating this antenna were done with larger dielectric constants, and thus for this design the ϵ_r was reduced to 2. Using shells instead of full elliptical dielectric cylinders would likely improve the bandwidth, but this would likely require extremely precise manufacturing to make, and thus the full elliptical dielectric cylinders were used in the designs. It is also important to note that several sizes for the dielectric were considered before this size was chosen, with $a = 1.1$ mm and $b = 0.45$ mm for the first metasurface layer, and with $a_2 = 1.6$ mm and $b_2 = 1.24$ mm for the outer metasurface layer.

The antenna's real and input impedance are shown in Fig. 3.23 and 3.24. This elliptical antenna has similar behavior in the real and imaginary parts of the input impedance, where it can be seen that the resistance and reactance both become significantly flatter than the antenna without the metasurface in the frequency range of interest.
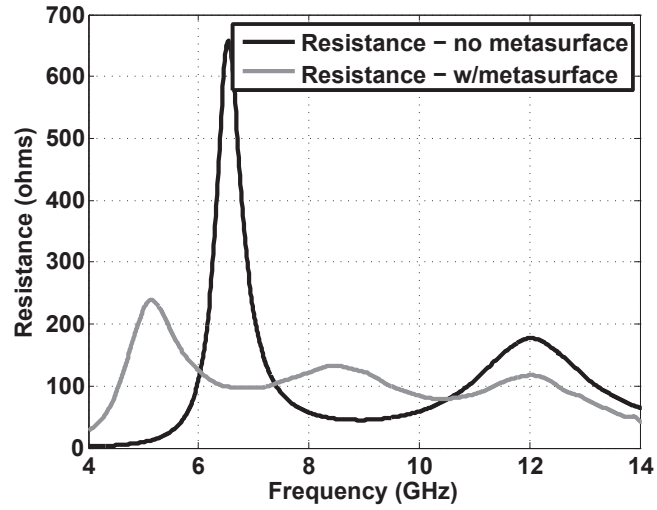
Figure 3.23. Real input impedance of the second, higher frequency, wideband elliptical Monopole Antenna.
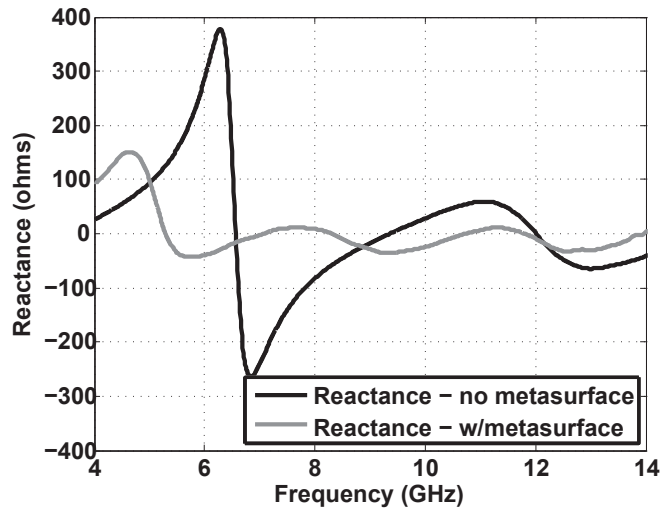
Figure 3.24. Imaginary input impedance of the second, higher frequency, wideband elliptical Monopole Antenna.
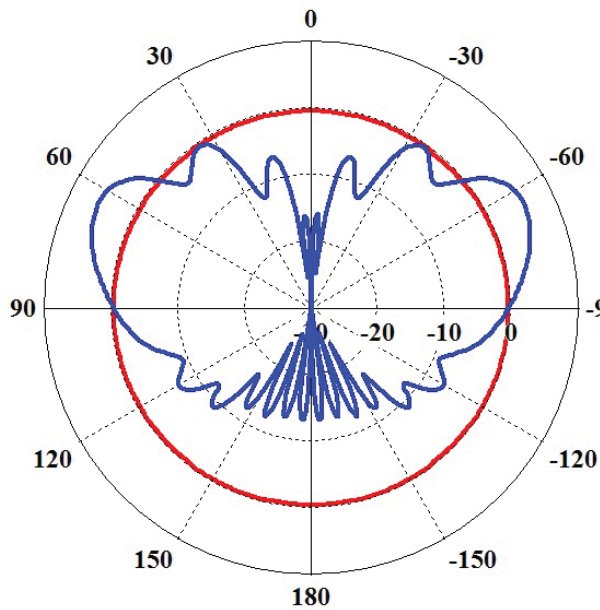
(a) E and H-Plane radiation patterns at 6 GHz
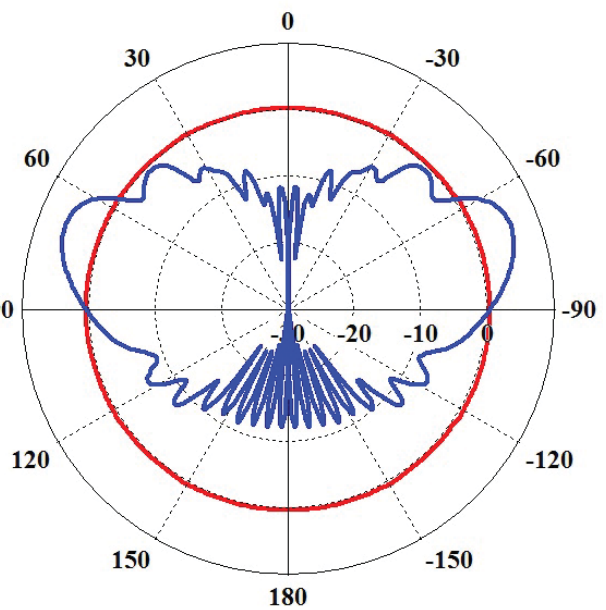
(b) E and H-Plane radiation patterns at 8 GHz
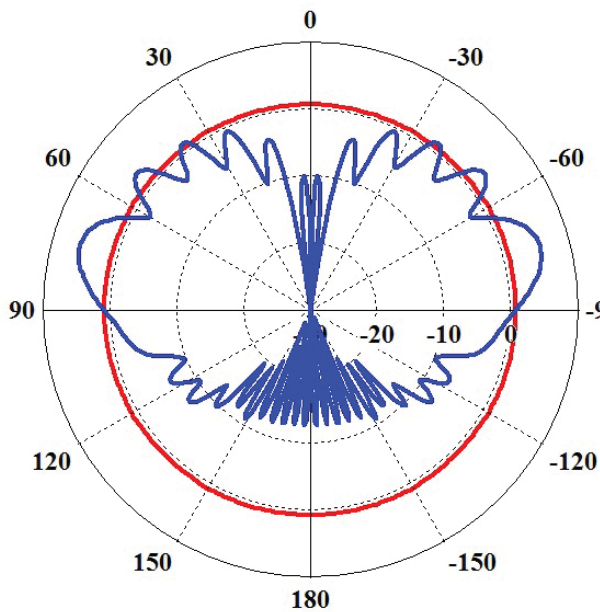
(c) E and H-Plane radiation patterns at 10 GHz
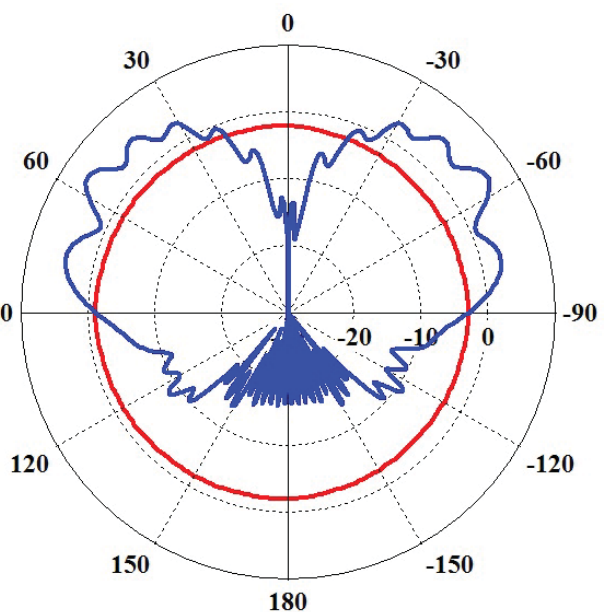
(d) E and H-Plane radiation patterns at 12 GHz

Figure 3.25. E (blue) and H-plane (red) radiation patterns for the higher frequency elliptical wideband monopole antenna, at different frequencies within the -10 dB bandwidth (5.51 - 13.63 GHz).

As always, another point of interest is the radiation pattern of the antenna, the E and H-Plane radiation patterns can be seen in Fig. 3.25. The radiation patterns are slightly different from the original cylindrical monopole antenna, but not so different that it is a significant concern. The radiation patterns are consistent throughout the frequency range which is a good indicator of the overall performance of this new elliptical monopole antenna.

Now that the higher frequency antenna has been designed, the lower frequency elliptical monopole antenna can be created. This monopole antenna has a length $l = 24$ mm and width $w = 2$ mm. The length of the dielectric is $H_l = 96$ mm which can be seen in the cross section of the antenna along with the unit cell in Fig. 3.26. The length of the unit cell was increased to $L = 22$ mm to accommodate the increased bandwidth at lower frequencies, with the rest of the parameters for the unit cell as follows: $B = 24$ mm, $W = 2$ mm, $C = 1.5$ mm, $G = 0.8$ mm, and $w_2 = 0.5$ mm. The S-parameters and input impedance of this lower
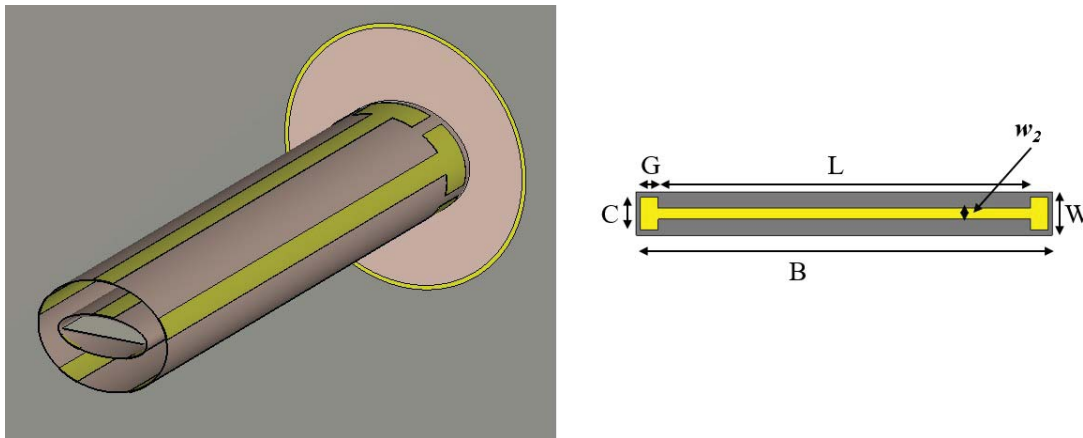
Figure 3.26. Cross sectional view of the elliptical wideband antenna and the metasurface unit cell.

frequency antenna are shown in Figs. 3.27 - 3.29. One this that is interesting to note is that the behavior of the S_{11} is still very similar to the original cylindrical antenna, where a second resonance was introduced to the antenna, which directly caused the increased bandwidth. The bandwidth of this antenna is slightly smaller than the original cylindrical antenna, with a -10 dB bandwidth of 1.86 - 3.89 GHz compared to the original bandwidth which was 2.3 - 4.54 GHz. This slight reduction in bandwidth could likely be addressed through further

78
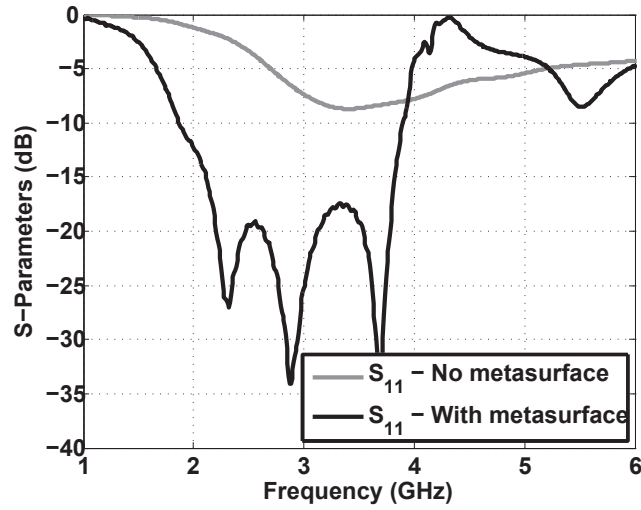
Figure 3.27. S-Parameters of the wideband monopole elliptical antenna, operating at a lower frequency.
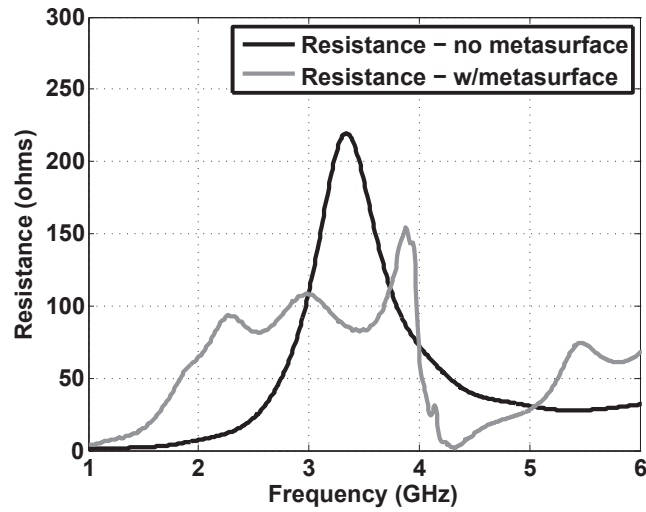
Figure 3.28. Real input impedance of the first, lower frequency, wideband elliptical Monopole Antenna.

investigation into both the size of the dielectric and the dielectric constant used. There are other opportunities for future investigation such as the parameters of the I-shaped pattern, which could also improve bandwidth or allow for easier shifting of the frequency of the antenna. It should be noted that by changing the vertical length of the unit cell, that the dielectric can become much larger than the strip monopole antenna, which can result in the second resonance of the antenna happening at a frequency too far away from the original resonance, resulting in two seperate resonances, with some point in the middle not having $S_{11} < $ -10 dB, which would not result in the large bandwidth that is desired.
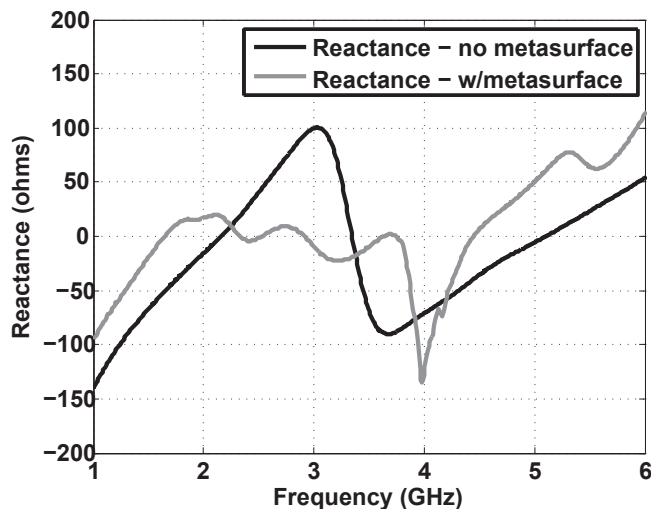
Figure 3.29. Imaginary input impedance of the first, lower frequency, wideband elliptical Monopole Antenna.

Finally, the radiation patterns of the antennas must be investigated, which are shown in Fig. 3.30. It is interesting to note than the E-plane (red) pattern for part b is smaller than the E-plane in part a, as for the other antennas the E-plane was not significantly affected by checking other frequencies inside the bandwidth. This is likely a side effect of using the elliptical structure as opposed to the original cylindrical structure, as the current elliptical structure does not have the air gaps of the cylindrical structure.
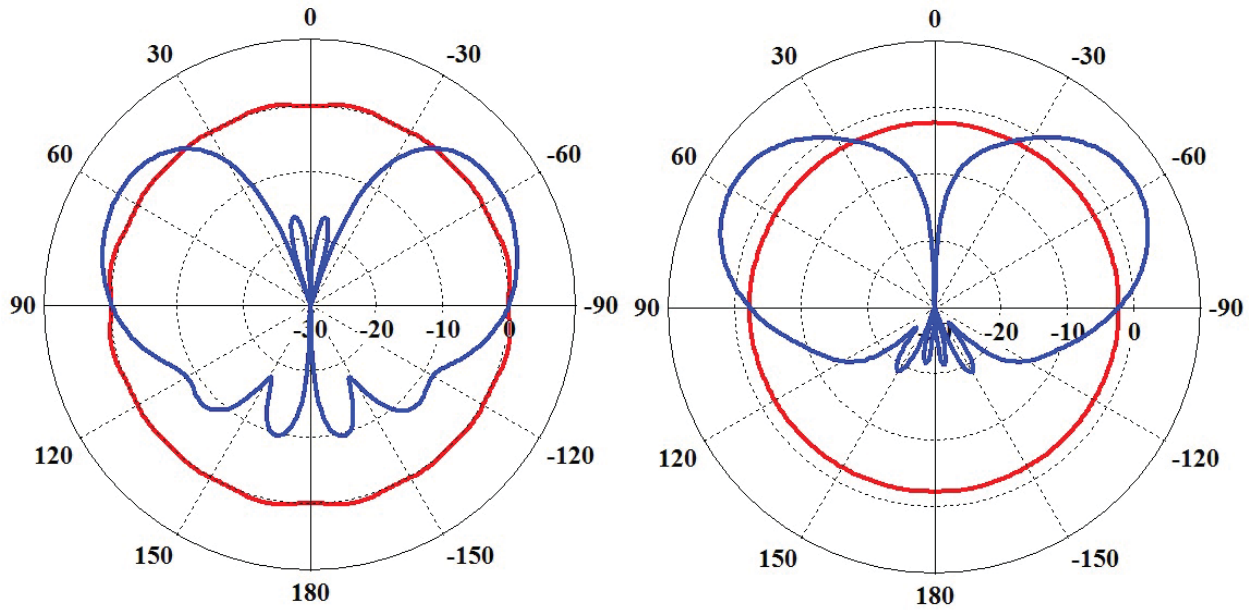
(a) E and H-Plane radiation patterns at 1.9 GHz

(b) E and H-Plane radiation patterns at 2.9 GHz
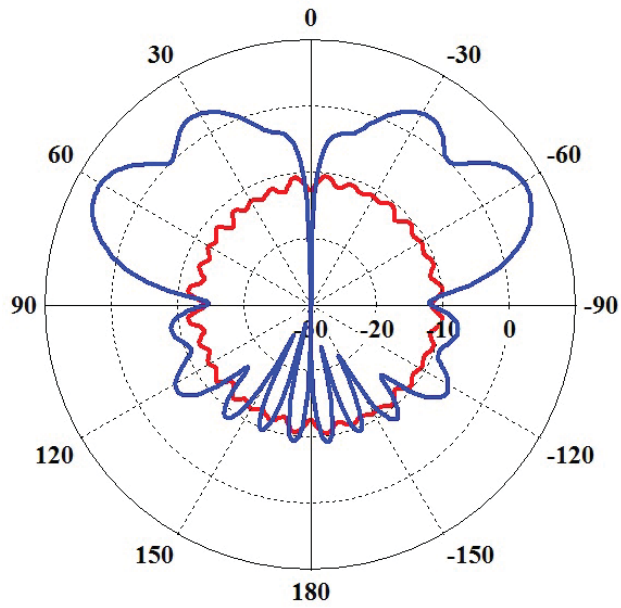
(c) E and H-Plane radiation patterns at 3.9 GHz

Figure 3.30. E (blue) and H-plane (red) radiation patterns for the lower frequency elliptical wideband monopole antenna, at different frequencies within the -10 dB bandwidth (1.86 - 3.89 GHz).

3.2.1 Coupled Elliptical Antennas

As before with the cylindrical antennas, now the two antennas are placed together on a single ground plane with two distances, $d = 26$ and 47 mm.
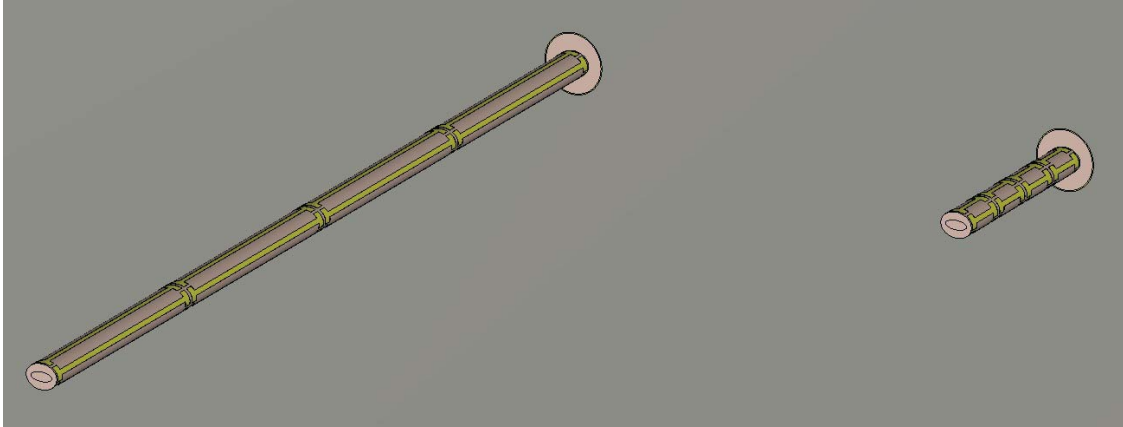
Figure 3.31. Geometry of the elliptical wideband antennas when placed at a distance $d = 51.7$ mm.

Figure 3.32. Geometry of the elliptical wideband antennas when placed at a distance $d = 103.4$ mm.

The geometry of these two spacings can be seen in 3.31 and 3.32 The mutual coupling between these two antennas is low throughout the entire frequency range, and can be seen in Figs. 3.33 and 3.34. For the cylindrical antennas, there was a -5 dB difference between the closer and farther spacing, but for this elliptical case, the difference between the mutual coupling of the two antennas is less affected by the distance between the antennas, for instance at $f = 4$ GHz, the mutual coupling for $d = 51.7$ and 103.4 mm is -24 dB and -26 dB

respectively, which is a very small difference. The bandwidth of these two antennas is also not significantly affected by the placement of the two antennas on the same ground plane.
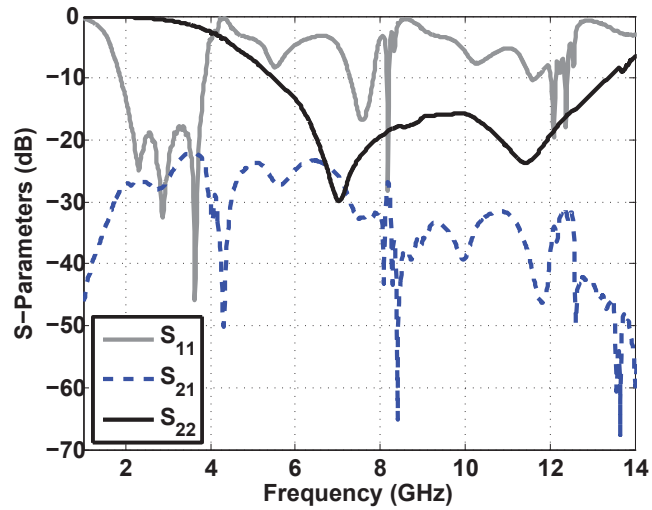
Figure 3.33. S-Parameters of the coupled wideband elliptical monopole antennas when placed at a distance $d = 51.7$ mm.
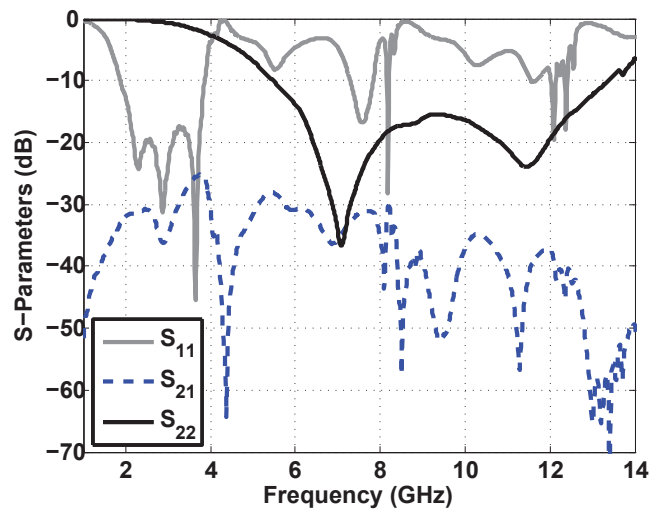
Figure 3.34. S-Parameters of the coupled wideband elliptical monopole antennas when placed at a distance $d = 103.4$ mm.
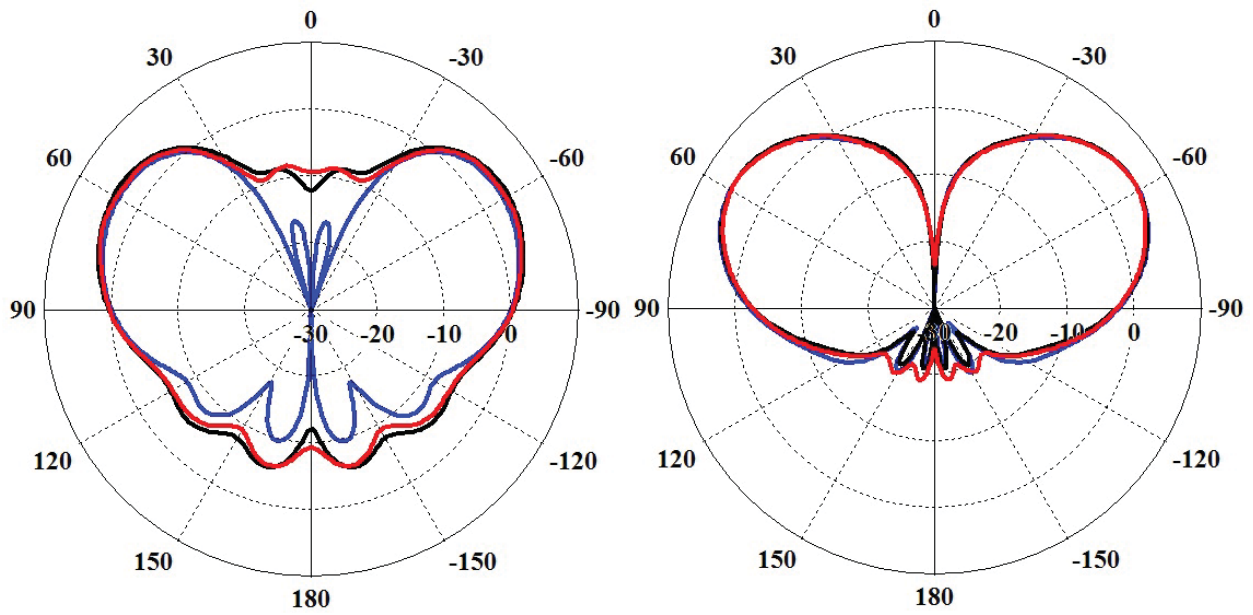
(a) E-Plane radiation patterns at 1.9 GHz

(b) E-Plane radiation patterns at 2.9 GHz
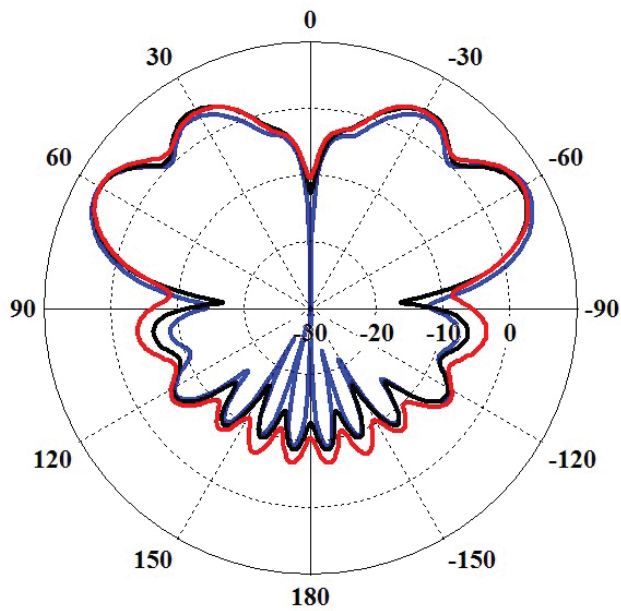
(c) E-Plane radiation patterns at 3.9 GHz

Figure 3.35. E-plane radiation patterns for the lower frequency elliptical wideband monopole antenna, when the antenna is isolated (blue), and coupled at distances $d = 51.7$ mm (red) and 103.4 mm (black).
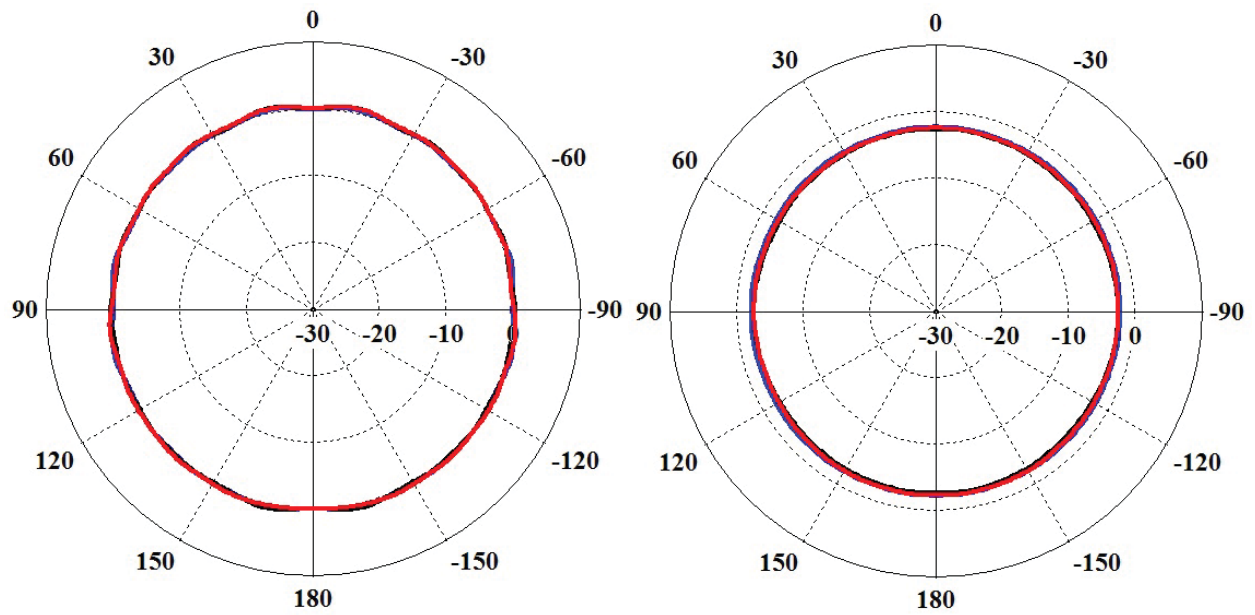
(a) H-Plane radiation patterns at 1.9 GHz

(b) H-Plane radiation patterns at 2.9 GHz
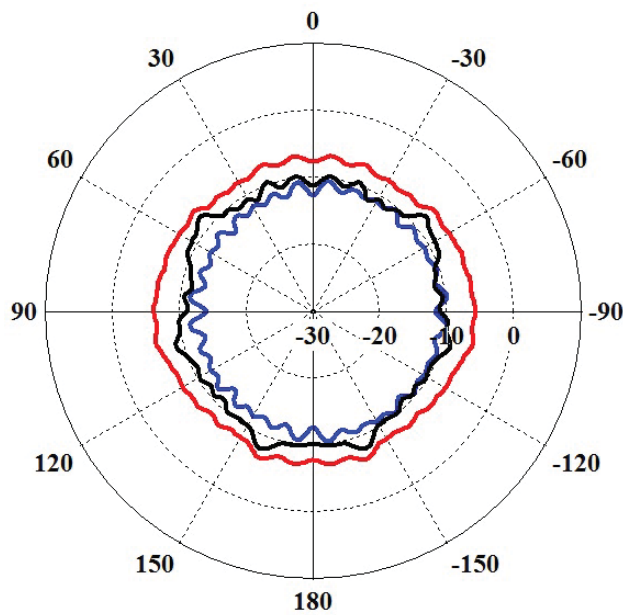
(c) H-Plane radiation patterns at 3.9 GHz

Figure 3.36. H-plane radiation patterns for the lower frequency elliptical wideband monopole antenna, when the antenna is isolated (blue), and coupled at distances $d = 51.7$ mm (red) and 103.4 mm (black).
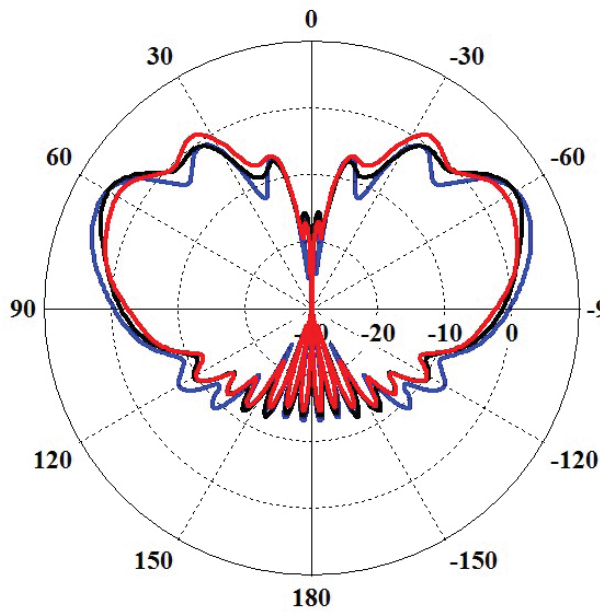
(a) E-Plane radiation patterns at 6 GHz
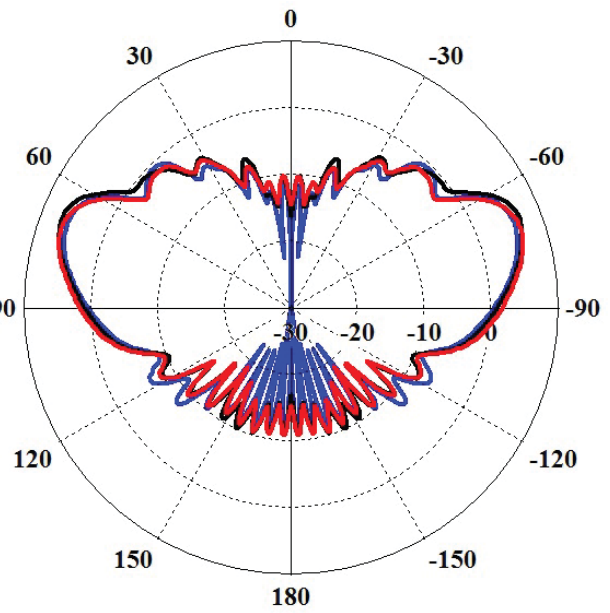
(b) E-Plane radiation patterns at 8 GHz
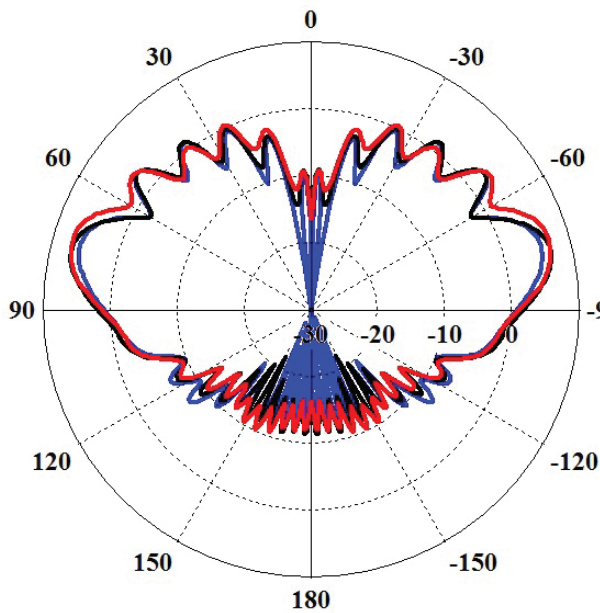
(c) E-Plane radiation patterns at 10 GHz
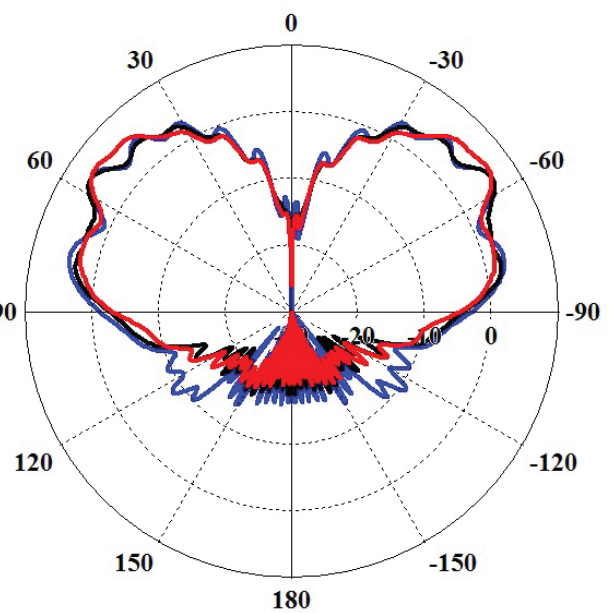
(d) E-Plane radiation patterns at 12 GHz

Figure 3.37. E-plane radiation patterns for the higher frequency elliptical wideband monopole antenna, when the antenna is isolated (blue), and coupled at distances $d = 51.7$ mm (red) and 103.4 mm (black).

86
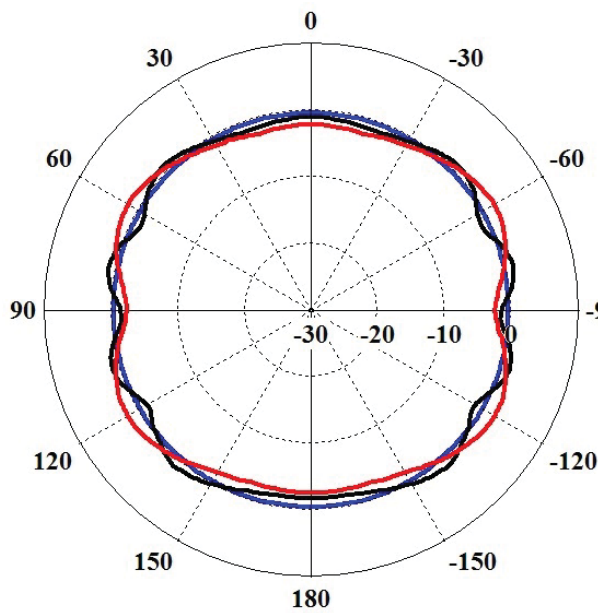
(a) H-Plane radiation patterns at 6 GHz

(b) H-Plane radiation patterns at 8 GHz
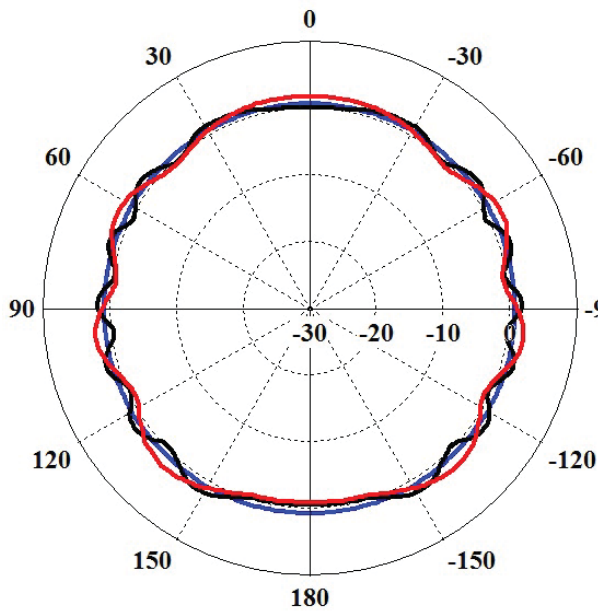
(c) H-Plane radiation patterns at 10 GHz
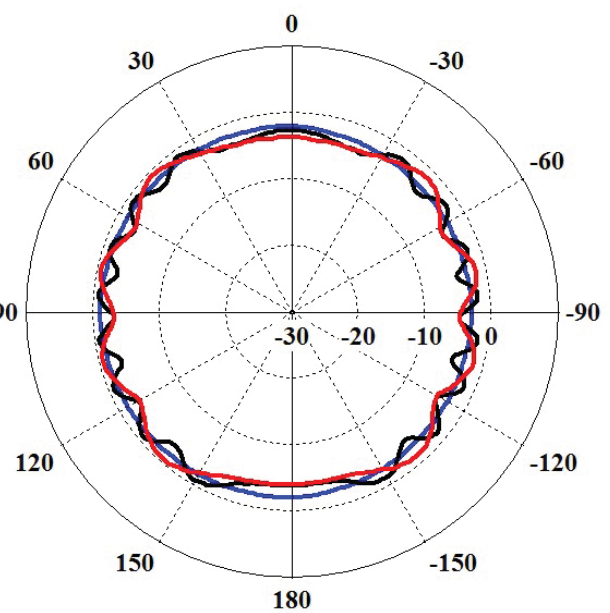
(d) H-Plane radiation patterns at 12 GHz

Figure 3.38.   H-plane radiation patterns for the higher frequency elliptical wideband monopole antenna, when the antenna is isolated (blue), and coupled at distances $d = 51.7$ mm (red) and 103.4 mm (black).

In Figs. 3.35 - 3.38, the E and H-Plane radiation patterns for the two antennas can be seen for three cases, isolated (blue), spaced at $d = 51.7$ mm (red), and spaced at $d =$

103.4 mm (black). As before with the cylindrical monopole antennas, the radiation patterns of the lower frequency antenna are not significantly affected by the introduction of the higher frequency antenna. However, the E-plane of the higher frequency antenna is the most clear in its indication of how the radiation patterns are distorted by the introduction of the lower frequency antenna, as there is a slight flattening radiation pattern.

3.3 Microstrip Wideband Antenna

The final goal of exploring these antennas was to bring their bandwidth enhancement to microstrip technology. It is important to note that the work done in this section is only the preliminary steps towards moving to using microstrip technology combined with these wideband monopole antennas. The transition to to the elliptical structures was the first step in this goal of achieving wideband microstrip antennas. To this end, the same structure as the elliptical monopole antennas was chosen, with $a_1 = 1.2$ mm and $b_1 = 0.66$ mm for the first metasurface layer, and with $a_2 = 2.2$ mm and $b_2 = 1.95$ mm for the outer metasurface layer. The geometry of the antenna on the microstrip can be seen in Fig. 3.39.

This structure was then placed onto a substrate with $\epsilon_r = 2.2$, with $L_{sub} = 120$ mm, $W_{sub} = 70$ mm, $H_{sub} = 2.5$ mm. The SMA type port from the previous monopoles was also used here, which is important to providing the increased bandwidth. The size of the port had to be increased to create a connection between the outer conductor and the partial ground plane that rests beneath the substrate which has a length $L_{ground} = 17$ mm. The main ideas for this microstrip structure come from the previous work done on the cloaking of microstrip antennas at GHz done in [59], where the same partial ground plane was used. The metasurface wrapped around the antenna starts at the same place where the ground plane ends, as this is where the antenna starts, and the strip above the ground plane represents a normal microstrip line to feed the antenna. A cross section and the unit cell for the two antennas can be seen in Figs. 3.41 and 3.42. For Antenna I, the parameters of the unit cell
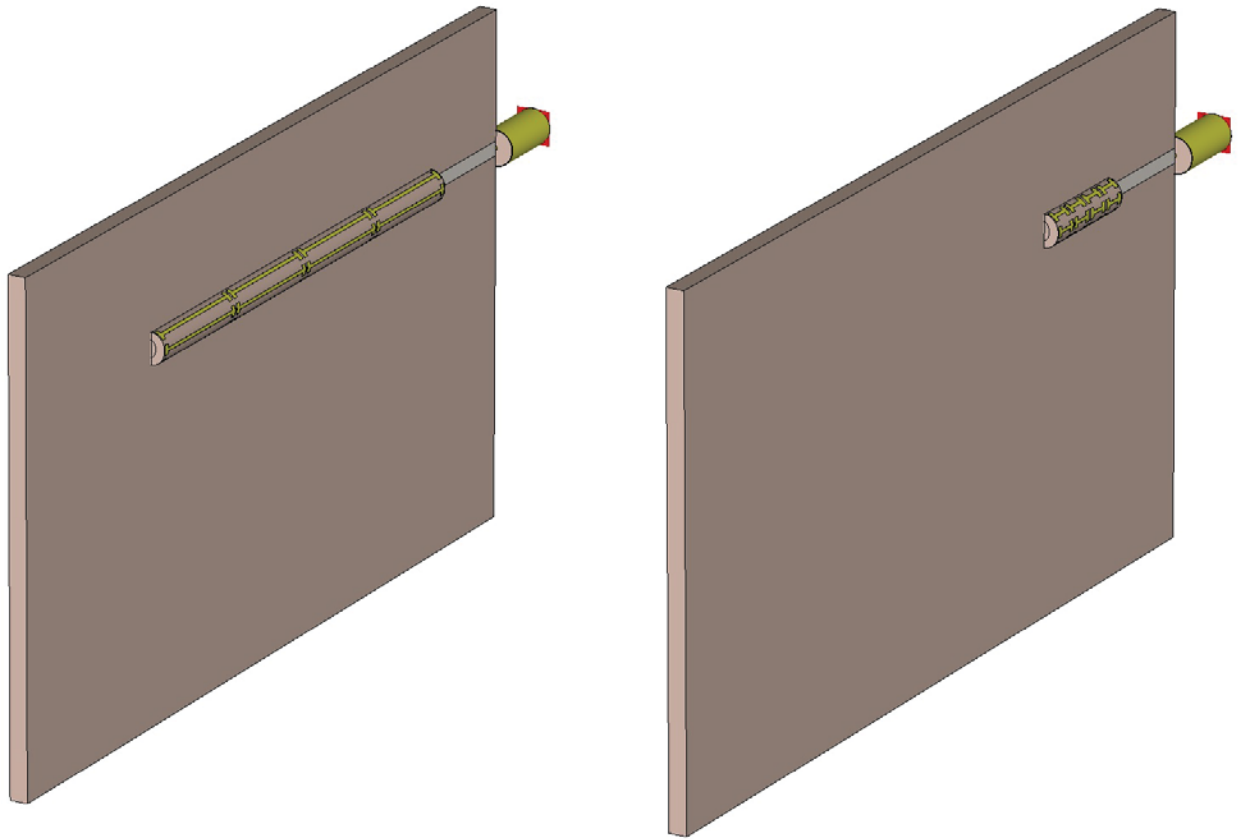
Figure 3.39. Geometry of the microstrip wideband Antenna I and II on the microstrip substrate.
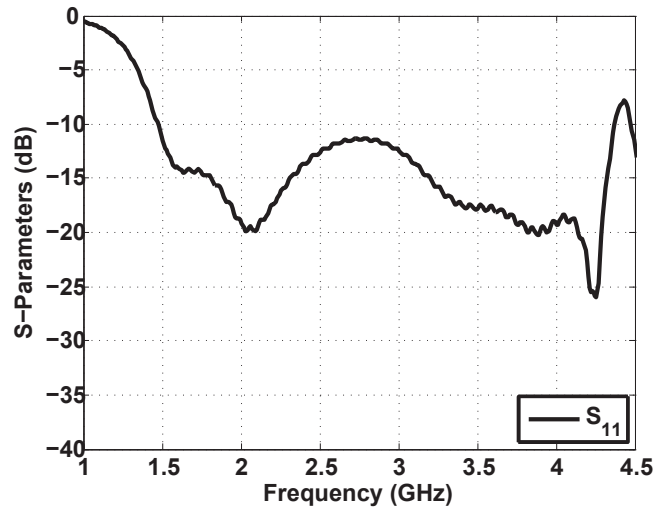
Figure 3.40. S-Parameters of the wideband monopole microstrip antenna, operating at a lower frequency.

are as follows: $B = 19$ mm, $L = 17$ mm, $W = 2$ mm, $C = 1.5$ mm, $G = 0.8$ mm, $w_2 = 0.5$ mm, and the $gap = 0.4$ mm (Fig. 3.41). For Antenna II, the parameters of the unit cell are: $B = 5$ mm, $L = 3$ mm, $W = 2$ mm, $C = 1.5$ mm, $G = 0.8$ mm, $w_2 = 0.5$ mm, and the $gap = 0.4$ mm (Fig. 3.42).
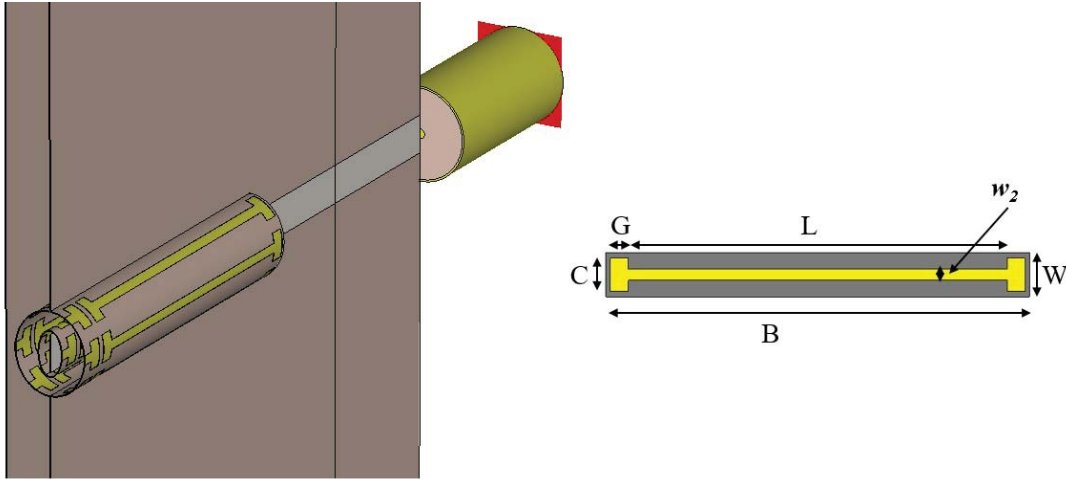
Figure 3.41. Geometry of the microstrip wideband Antenna I and II on the microstrip substrate.
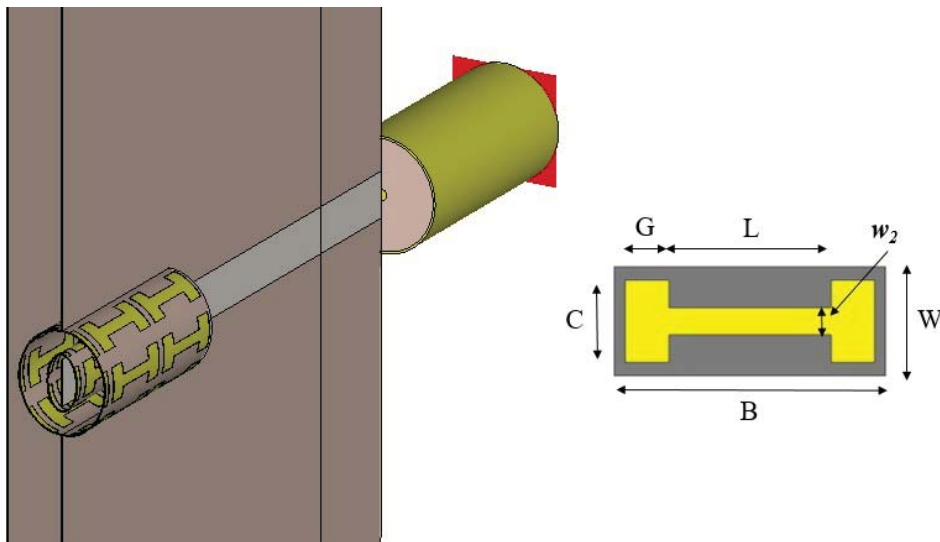
Figure 3.42. Geometry of the microstrip wideband Antenna I and II on the microstrip substrate.

Two antennas were created for the microstrip structure, lower and higher frequency monopole antennas. The S-parameters of these two antennas can be seen in Figs. 3.40 and

3.43. The increased bandwidth that is desired is achieved for these two initial designs, with the -10 bandwidth of the first antenna being 1.47 - 4.37 GHz. The second antenna's -10 dB bandwidth is 4.61 - 11.4 GHz. There are opportunities to continue expanding on this idea, with the goal of using smaller dielectrics to keep the size for the microstrip environment, where planarity is a key concern when designing antennas.
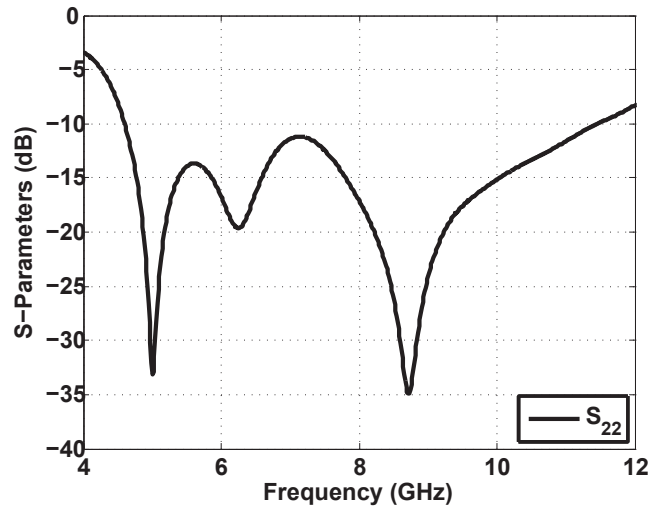
Figure 3.43. S-Parameters of the wideband monopole microstrip antenna, operating at a lower frequency.

There is a concern with these initial microstrip designs, which is the radiation patterns of the antennas, which can be seen in Figs. 3.44 and 3.45. The patterns are not as clear cut as the previous cases, where there are significant extra lobes in the radiation pattern which must be addressed before the antennas can be placed close together. One part that is affecting this is the size of the dielectric, as the lower frequency antenna is very large at the moment, which requires a large dielectric to fit the antenna on the microstrip. However, the bandwidth of the antennas is definitely a strong starting point for further, as this bandwidth is already much larger than that of a strip monopole antenna on microstrip.

91
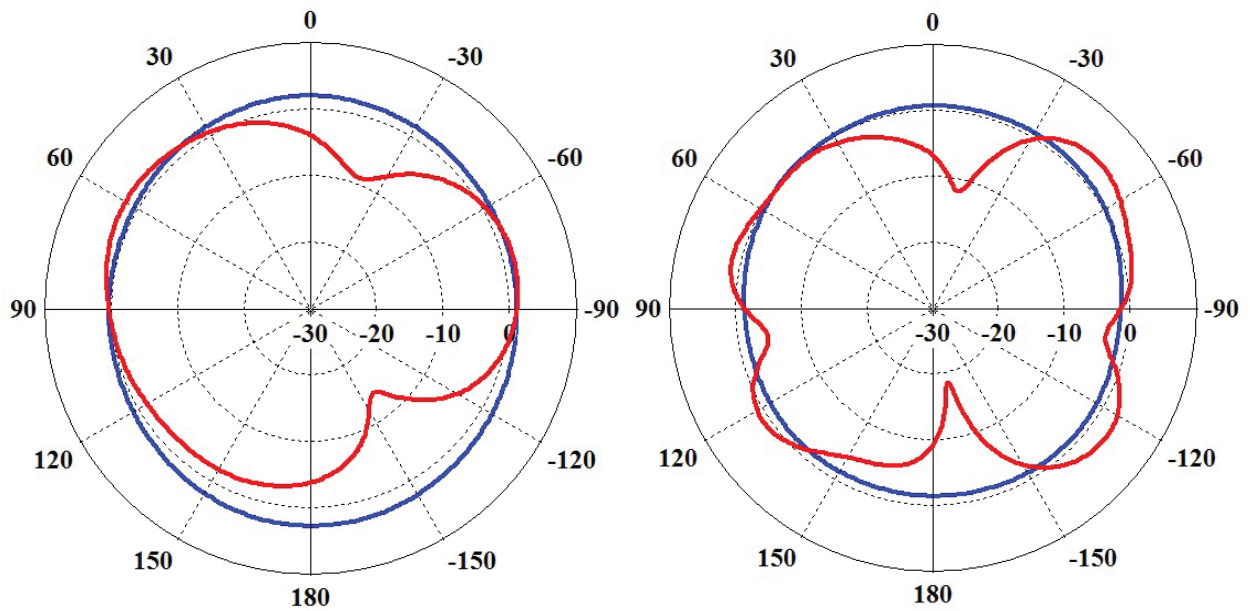
(a) E-Plane and H-Plane radiation patterns at 2 GHz(b) E-Plane and H-Plane radiation patterns at 4 GHz

Figure 3.44. E-Plane (red) and H-Plane (blue) radiation patterns for the lower frequency elliptical wideband monopole antenna, at different frequencies within the -10 dB bandwidth (1.47 - 4.37 GHz).
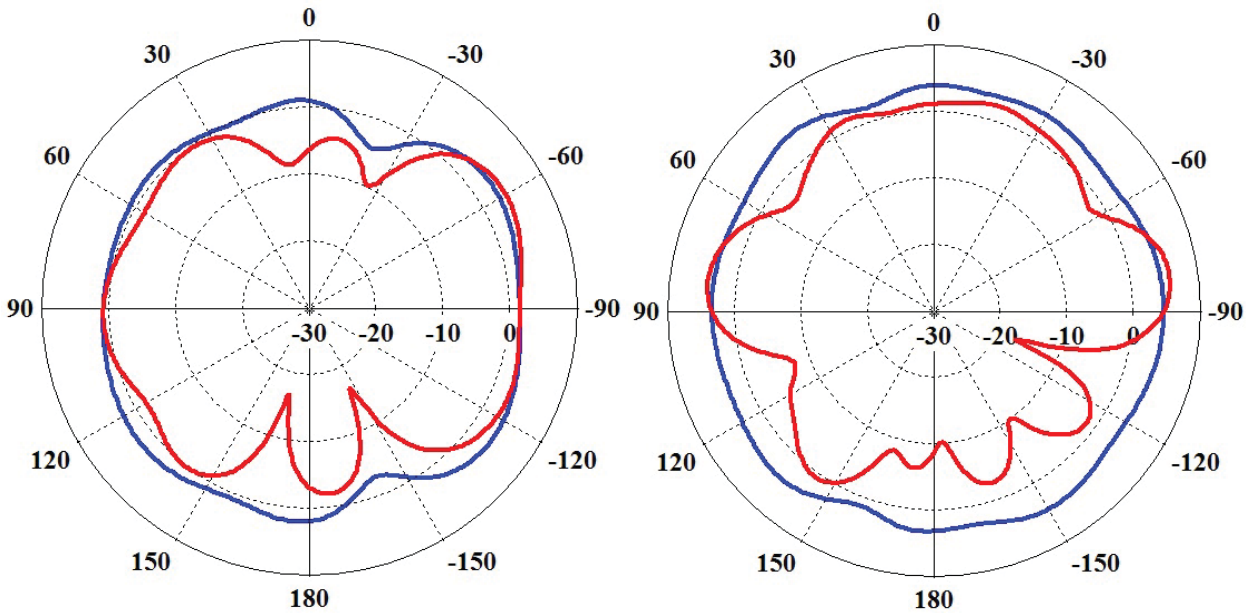
(a) E-Plane and H-Plane radiation patterns at 6 GHz(b) E-Plane and H-Plane radiation patterns at 10 GHz

Figure 3.45. E-Plane (red) and H-Plane (blue) radiation patterns for the higher frequency elliptical wideband monopole antenna, at different frequencies within the -10 dB bandwidth (4.61 - 11.4 GHz).

3.4 Future Work

The use of metasurfaces to drastically increase the bandwidth of antennas is an exciting opportunity for further research. While this chapter focused on the transformation of the underlying structure to different geometries, there are more opportunities available for study, in particular when these antennas are placed together on the same ground plane. Currently, there is some disturbance caused by the antennas in the far-field, when they are placed at distances $d = \lambda/2$ and $d = \lambda$. This interaction must be further explored with the hopes of reducing the interaction between these antennas further. Additionally, when these antennas are placed very close together in the near-field, at a distance $d = \lambda/10$, the bandwidth of the antennas are significantly affected. This also requires further investigation, as it would be extremely useful if these antennas could be brought closer together. Finally, there is some room for the improvement of the microstrip antenna designs for these wideband antennas, as the currently designs are quite large, when referring to the cross sectional size of the dielectric ellipses. Smaller sizes for the dielectric ellipses would allow for smaller substrates which is always an important goal when designing microstrip antennas.

3.5 Conclusion

In this section, the drastic improvement of the bandwidth of monopole antennas was considered. This increase in bandwidth stemmed from the use of multiple metasurfaces working together to cause a flattening of the input impedance which leads to increased bandwidth. The antennas also maintained good radiation patterns throughout their -10dB bandwidth. The antennas were also further delved into in regards to the mutual coupling between two antennas with non-overlapping bandwidths. The radiation patterns have not been significantly affected by the introduction of another antenna, which is promising for the use with these antennas. These antennas present exciting opportunities for their potential to be used in different geometries with similar bandwidth behavior.

BIBLIOGRAPHY

BIBLIOGRAPHY

[1] C. L. Holloway, E. F. Kuester, J. A. Gordon, J. O'Hara, J. Booth, and D. R. Smith, "An overview of the theory and applications of metasurfaces: The two-dimensional equivalents of metamaterials," *IEEE Antennas and Propagation Magazine*, vol. 54, no. 2, pp. 10–35, 2012.

[2] K. S. Novoselov, A. K. Geim, S. Morozov, D. Jiang, Y. Zhang, S. Dubonos, , I. Grigorieva, and A. Firsov, "Electric field effect in atomically thin carbon films," *science*, vol. 306, no. 5696, pp. 666–669, 2004.

[3] G. W. Hanson, "Dyadic green's functions and guided surface waves for a surface conductivity model of graphene," *Journal of Applied Physics*, vol. 103, no. 6, p. 064302, 2008.

[4] I. E. Abbott's, "Graphene: exploring carbon flatland," *Physics today*, vol. 60, no. 8, p. 35, 2007.

[5] A. K. Geim and K. S. Novoselov, "The rise of graphene," *Nature materials*, vol. 6, no. 3, pp. 183–191, 2007.

[6] T. Seyller, A. Bostwick, K. Emtsev, K. Horn, L. Ley, J. McChesney, T. Ohta, J. D. Riley, E. Rotenberg, and F. Speck, "Epitaxial graphene: a new material," *physica status solidi (b)*, vol. 245, no. 7, pp. 1436–1446, 2008.

[7] V. Gusynin, S. Sharapov, and J. Carbotte, "Magneto-optical conductivity in graphene," *Journal of Physics: Condensed Matter*, vol. 19, no. 2, p. 026222, 2006.

[8] A. Vakil and N. Engheta, "Transformation optics using graphene," *Science*, vol. 332, no. 6035, pp. 1291–1294, 2011.

[9] X. Li, W. Cai, J. An, S. Kim, J. Nah, D. Yang, R. Piner, A. Velamakanni, I. Jung, E. Tutuc, *et al.*, "Large-area synthesis of high-quality and uniform graphene films on copper foils," *Science*, vol. 324, no. 5932, pp. 1312–1314, 2009.

[10] A. Reina, X. Jia, J. Ho, D. Nezich, H. Son, V. Bulovic, M. S. Dresselhaus, and J. Kong, "Large area, few-layer graphene films on arbitrary substrates by chemical vapor deposition," *Nano letters*, vol. 9, no. 1, pp. 30–35, 2008.

[11] M. Tamagnone, J. Gomez-Diaz, J. R. Mosig, and J. Perruisseau-Carrier, "Reconfigurable terahertz plasmonic antenna concept using a graphene stack," *Applied Physics Letters*, vol. 101, no. 21, p. 214102, 2012.

[12] D. Correas-Serrano, J. S. Gomez-Diaz, A. Alù, and A. Á. Melcón, "Electrically and magnetically biased graphene-based cylindrical waveguides: Analysis and applications as reconfigurable antennas," *IEEE Transactions on Terahertz Science and Technology*, vol. 5, no. 6, pp. 951–960, 2015.

[13] I. Llatser, C. Kremers, A. Cabellos-Aparicio, J. M. Jornet, E. Alarcón, and D. N. Chigrin, "Graphene-based nano-patch antenna for terahertz radiation," *Photonics and Nanostructures-Fundamentals and Applications*, vol. 10, no. 4, pp. 353–358, 2012.

[14] P.-Y. Chen, C. Argyropoulos, and A. Alu, "Terahertz antenna phase shifters using integrally-gated graphene transmission-lines," *IEEE Transactions on Antennas and Propagation*, vol. 61, no. 4, pp. 1528–1537, 2013.

[15] E. Carrasco and J. Perruisseau-Carrier, "Reflectarray antenna at terahertz using graphene," *IEEE Antennas and Wireless Propagation Letters*, vol. 12, pp. 253–256, 2013.

[16] W. Cai, U. K. Chettiar, A. V. Kildishev, and V. M. Shalaev, "Optical cloaking with metamaterials," *Nature photonics*, vol. 1, no. 4, pp. 224–227, 2007.

[17] D. Schurig, J. Mock, B. Justice, S. A. Cummer, J. B. Pendry, A. Starr, and D. Smith, "Metamaterial electromagnetic cloak at microwave frequencies," *Science*, vol. 314, no. 5801, pp. 977–980, 2006.

[18] P.-Y. Chen and A. Alù, "Atomically thin surface cloak using graphene monolayers," *ACS nano*, vol. 5, no. 7, pp. 5855–5863, 2011.

[19] P.-Y. Chen, J. Soric, Y. R. Padooru, H. M. Bernety, A. B. Yakovlev, and A. Alù, "Nanostructured graphene metasurface for tunable terahertz cloaking," *New Journal of Physics*, vol. 15, no. 12, p. 123029, 2013.

[20] Z. H. Jiang, P. E. Sieber, L. Kang, and D. H. Werner, "Restoring intrinsic properties of electromagnetic radiators using ultralightweight integrated metasurface cloaks," *Advanced Functional Materials*, vol. 25, no. 29, pp. 4708–4716, 2015.

[21] D.-H. Kwon and D. H. Werner, "Restoration of antenna parameters in scattering environments using electromagnetic cloaking," *Applied physics letters*, vol. 92, no. 11, p. 113507, 2008.

[22] P. Alitalo, J. Vehmas, and S. A. Tretyakov, "Reduction of antenna blockage with a transmission-line cloak," in *Proceedings of the 5th European Conference on Antennas and Propagation (EUCAP)*, pp. 2399–2402, IEEE, 2011.

[23] Z. H. Jiang and D. H. Werner, "Exploiting metasurface anisotropy for achieving near-perfect low-profile cloaks beyond the quasi-static limit," *Journal of Physics D: Applied Physics*, vol. 46, no. 50, p. 505306, 2013.

[24] R. Mitchell-Thomas, T. McManus, O. Quevedo-Teruel, S. Horsley, and Y. Hao, "Perfect surface wave cloaks," *Physical review letters*, vol. 111, no. 21, p. 213901, 2013.

[25] J. Wang, S. Qu, Z. Xu, H. Ma, J. Zhang, Y. Li, and X. Wang, "Super-thin cloaks based on microwave networks," *IEEE Transactions on Antennas and Propagation*, vol. 61, no. 2, pp. 748–754, 2013.

[26] C. A. Valagiannopoulos, P. Alitalo, and S. A. Tretyakov, "On the minimal scattering response of pec cylinders in a dielectric cloak," *IEEE Antennas and Wireless Propagation Letters*, vol. 13, pp. 403–406, 2014.

[27] P.-S. Kildal, A. A. Kishk, and A. Tengs, "Reduction of forward scattering from cylindrical objects using hard surfaces," *IEEE Transactions on Antennas and Propagation*, vol. 44, no. 11, pp. 1509–1520, 1996.

[28] F. Monticone and A. Alù, "Do cloaked objects really scatter less?," *Physical Review X*, vol. 3, no. 4, p. 041005, 2013.

[29] P.-Y. Chen, C. Argyropoulos, and A. Alù, "Broadening the cloaking bandwidth with non-foster metasurfaces," *Physical review letters*, vol. 111, no. 23, p. 233001, 2013.

[30] F. Bilotti, S. Tricarico, F. Pierini, and L. Vegni, "Cloaking apertureless near-field scanning optical microscopy tips," *Optics letters*, vol. 36, no. 2, pp. 211–213, 2011.

[31] B. Edwards, A. Alù, M. G. Silveirinha, and N. Engheta, "Experimental verification of plasmonic cloaking at microwave frequencies with metamaterials," *Physical Review Letters*, vol. 103, no. 15, p. 153901, 2009.

[32] D. Rainwater, A. Kerkhoff, K. Melin, J. Soric, G. Moreno, and A. Alù, "Experimental verification of three-dimensional plasmonic cloaking in free-space," *New Journal of Physics*, vol. 14, no. 1, p. 013054, 2012.

[33] A. Alù and N. Engheta, "Cloaking and transparency for collections of particles with metamaterial and plasmonic covers," *Optics Express*, vol. 15, no. 12, pp. 7578–7590, 2007.

[34] A. Alù and N. Engheta, "Cloaking a sensor," *Physical review letters*, vol. 102, no. 23, p. 233901, 2009.

[35] A. Alù, "Mantle cloak: Invisibility induced by a surface," *physical review B*, vol. 80, no. 24, p. 245115, 2009.

[36] Y. R. Padooru, A. B. Yakovlev, P.-Y. Chen, and A. Alù, "Analytical modeling of conformal mantle cloaks for cylindrical objects using sub-wavelength printed and slotted arrays," *Journal of Applied Physics*, vol. 112, no. 3, p. 034907, 2012.

[37] Y. R. Padooru, A. B. Yakovlev, C. S. Kaipa, G. W. Hanson, F. Medina, and F. Mesa, "Dual capacitive-inductive nature of periodic graphene patches: Transmission characteristics at low-terahertz frequencies," *Physical Review B*, vol. 87, no. 11, p. 115401, 2013.

[38] H. M. Bernety and A. B. Yakovlev, "Cloaking of single and multiple elliptical cylinders and strips with confocal elliptical nanostructured graphene metasurface," *Journal of Physics: Condensed Matter*, vol. 27, no. 18, p. 185304, 2015.

[39] A. Monti, J. Soric, A. Alu, F. Bilotti, A. Toscano, and L. Vegni, "Overcoming mutual blockage between neighboring dipole antennas using a low-profile patterned metasurface," *IEEE Antennas and Wireless Propagation Letters*, vol. 11, pp. 1414–1417, 2012.

[40] F. Yang and Y. Rahmat-Samii, "Microstrip antennas integrated with electromagnetic band-gap (ebg) structures: A low mutual coupling design for array applications," *IEEE Transactions on Antennas and Propagation*, vol. 51, no. 10, pp. 2936–2946, 2003.

[41] S.-S. Lee, H.-S. Park, J.-G. Bang, and H.-T. Kim, "Coupling reduction between slanted shipboard antennas," *Microwave and Optical Technology Letters*, vol. 33, no. 1, pp. 37–40, 2002.

[42] M. M. Nikolic, A. R. Djordjevic, and A. Nehorai, "Microstrip antennas with suppressed radiation in horizontal directions and reduced coupling," *IEEE transactions on antennas and propagation*, vol. 53, no. 11, pp. 3469–3476, 2005.

[43] M. A. Khayat, J. T. Williams, D. R. Jackson, and S. A. Long, "Mutual coupling between reduced surface-wave microstrip antennas," *IEEE Transactions on Antennas and Propagation*, vol. 48, no. 10, pp. 1581–1593, 2000.

[44] E. Rajo-Iglesias, O. Quevedo-Teruel, and L. Inclan-Sanchez, "Mutual coupling reduction in patch antenna arrays by using a planar ebg structure and a multilayer dielectric substrate," *IEEE Transactions on Antennas and Propagation*, vol. 56, no. 6, pp. 1648–1655, 2008.

[45] H. S. Farahani, M. Veysi, M. Kamyab, and A. Tadjalli, "Mutual coupling reduction in patch antenna arrays using a uc-ebg superstrate," *IEEE Antennas and Wireless Propagation Letters*, vol. 9, pp. 57–59, 2010.

[46] M. Coulombe, S. F. Koodiani, and C. Caloz, "Compact elongated mushroom (em)-ebg structure for enhancement of patch antenna array performances," *IEEE Transactions on Antennas and Propagation*, vol. 58, no. 4, pp. 1076–1086, 2010.

[47] S. D. Assimonis, T. V. Yioultsis, and C. S. Antonopoulos, "Design and optimization of uniplanar ebg structures for low profile antenna applications and mutual coupling reduction," *IEEE Transactions on Antennas and Propagation*, vol. 60, no. 10, pp. 4944–4949, 2012.

[48] M. Salehi and A. Tavakoli, "A novel low mutual coupling microstrip antenna array design using defected ground structure," *AEU-International Journal of Electronics and Communications*, vol. 60, no. 10, pp. 718–723, 2006.

[49] F. Zhu, J. Xu, and Q. Xu, "Reduction of mutual coupling between closely-packed antenna elements using defected ground structure," in *Microwave, Antenna, Propagation*

and EMC Technologies for Wireless Communications, 2009 3rd IEEE International Symposium on, pp. 1–4, IEEE, 2009.

[50] J. Ouyang, F. Yang, and Z. Wang, "Reducing mutual coupling of closely spaced microstrip mimo antennas for wlan application," *IEEE Antennas and Wireless Propagation Letters*, vol. 10, pp. 310–313, 2011.

[51] C. K. Ghosh, B. Mandal, and S. K. Parui, "Mutual coupling reduction of a dual-frequency microstrip antenna array by using u-shaped dgs and inverted u-shaped microstrip resonator," *Progress In Electromagnetics Research C*, vol. 48, pp. 61–68, 2014.

[52] H. M. Bernety and A. B. Yakovlev, "Reduction of mutual coupling between neighboring strip dipole antennas using confocal elliptical metasurface cloaks," *Antennas and Propagation, IEEE Transactions on*, vol. 63, no. 4, pp. 1554–1563, 2015.

[53] K. Chung, J. Kim, and J. Choi, "Wideband microstrip-fed monopole antenna having frequency band-notch function," *IEEE Microwave and Wireless Components Letters*, vol. 15, no. 11, pp. 766–768, 2005.

[54] J. Kim, C. Cho, and J. Lee, "5.2 ghz notched ultra-wideband antenna using slot-type srr," *Electronics Letters*, vol. 42, no. 6, pp. 315–316, 2006.

[55] E. Lee, P. Hall, and P. Gardner, "Compact wideband planar monopole antenna," *Electronics Letters*, vol. 35, no. 25, pp. 2157–2158, 1999.

[56] K. Kim, Y. Cho, S. Hwang, and S. Park, "Band-notched uwb planar monopole antenna with two parasitic patches," *Electronics Letters*, vol. 41, no. 14, p. 1, 2005.

[57] Z. H. Jiang, M. D. Gregory, and D. H. Werner, "A broadband monopole antenna enabled by an ultrathin anisotropic metamaterial coating," *Antennas and Wireless Propagation Letters, IEEE*, vol. 10, pp. 1543–1546, 2011.

[58] G. Moreno, H. M. Bernety, and A. B. Yakovlev, "Reduction of mutual coupling between strip dipole antennas at terahertz frequencies with an elliptically shaped graphene monolayer," *IEEE Antennas and Wireless Propagation Letters*, vol. 15, pp. 1533–1536, 2016.

[59] H. M. Bernety and A. B. Yakovlev, "Decoupling antennas in printed technology using elliptical metasurface cloaks," *Journal of Applied Physics*, vol. 119, no. 1, 2016.

Gabriel Moreno is from Houston, Texas, born in October 1988. He received a B. S. degree in Electrical Engineering from the University of Texas at Austin in 2012. From 2014 to 2016, he worked as a research assistant at the University of Mississippi, where he pursued his Masters of Science degree in Electrical Engineering - Electromagnetics. His research interests include cloaking, antennas, and metasurfaces. Mr. Moreno is a student member of Institute of Electrical and Electronics Engineers (IEEE).

JOURNAL PUBLICATIONS

- G. Moreno, H. M. Bernety, and A. B. Yakovlev, "Reduction of mutual coupling between strip dipole antennas at terahertz frequencies with an elliptically shaped graphene monolayer," IEEE Antennas and Wireless Propagation Letters, vol. 15, pp. 1533–1536, 2016.

- D. Rainwater, A. Kerkhoff, K. Melin, J. Soric, G. Moreno, and A. Alù, "Experimental verification of three-dimensional plasmonic cloaking in free-space," New Journal of Physics, vol. 14, no. 1, p. 013054, 2012.

CONFERENCE PUBLICATIONS

- G. Moreno, H. M. Bernety, and A. B. Yakovlev, "Reduction of mutual coupling between strip dipole antennas at terahertz frequencies with an elliptically shaped graphene monolayer," 2016 IEEE International Symposium on Antennas and Propagation/USNC-URSI National Radio Science meeting, 2016.

AWARDS

- Best Student Poster award at the 2015 NSF I/UCRC BWAC IAB Meeting